

POLITECNICO

MILANO 1863

SCUOLA DI INGEGNERIA INDUSTRIALE E DELL'INFORMAZIONE
LAUREA MAGISTRALE IN ENGINEERING PHYSICS

MODERN TOOLS FOR X-RAY SPECTROSCOPY SIMULATIONS AND DATA ANALYSIS APPLIED TO STRONGLY CORRELATED SYSTEMS

Master's Thesis of:
Riccardo PIERGIACOMI
Student ID: 899254

Supervisor:
Prof. Giacomo GHIRINGHELLI

Co-supervisor:
Dr. Kurt KUMMER

Co-supervisor:
Dr. Marius RETEGAN

2018 - 2019

POLITECNICO DI MILANO

Abstract

Modern tools for X-ray spectroscopy simulations and data analysis applied to strongly correlated systems

by Riccardo PIERGIACOMI

Strongly correlated systems exhibit many exotic properties due to a strong Coulomb interaction among electrons. Several models try to describe these phenomena, but a complete theory taking into account all possible interactions has not been completed yet. Thus, further studies are needed to verify the correctness of models and uncover the physics still unexplained. X-ray absorption and Resonant Inelastic X-ray Scattering performed with synchrotron radiation are valid techniques to investigate strongly correlated materials. Some studies about intermediate valence in heavy fermion compounds reported disagreements with the theory, while others reported successful spectra simulation on strongly correlated oxides. In this thesis work, Multivariate Curve Resolution methods are employed as a tool to investigate intermediate valence in intermetallic ternary compounds based on Yb and Ce. In addition, starting from Density Functional Theory calculations, parametric spectra simulations of X-ray absorption and Resonant Inelastic X-ray Scattering performed on NiO and MnO are tested. The data analysis and spectra simulation methodologies presented and tested can be useful tools to better understand experimental results and shed some light on the theoretical models.

POLITECNICO DI MILANO

Sommario

Modern tools for X-ray spectroscopy simulations and data analysis applied to strongly correlated systems

by Riccardo PIERGIACOMI

La forte interazione Coulombiana tra elettroni genera proprietà interessanti all'interno di materiali fortemente correlati. Diversi sono i modelli che cercano di descrivere tali fenomeni, tuttavia non è stato ancora sviluppato un modello tenente conto di tutti i possibili tipi di interazioni presenti. Perciò sono necessari ulteriori studi per verificare la correttezza dei modelli e svelare fenomeni ancora inspiegabili. Le tecniche di X-ray Absorption e di Resonant Inelastic X-ray Scattering utilizzate con luce di sincrotrone sono valide sonde per investigare i materiali fortemente correlati. Alcuni studi riguardo la presenza di una valenza intermedia in composti a fermione pesante hanno mostrato alcune discordanze con i modelli teorici; mentre altri hanno riportato simulazioni di spettri su ossidi fortemente correlati con successo. In questo lavoro di tesi, metodi di Multivariate Curve Resolution sono utilizzati come strumento per investigare la presenza di una valenza intermedia in composti ternari intermetallici basati su Yb e Ce. Inoltre, partendo da calcoli di Density Functional Theory, sono testate simulazioni parametriche di spettri X-ray Absorption e Resonant Inelastic X-ray Scattering su NiO e MnO. Le metodologie di analisi dei dati e simulazioni di spettri presentati e testati possono essere utili strumenti per comprendere meglio i risultati sperimentali e indagare sulla correttezza dei modelli teorici.

Acknowledgements

I would like to thank my supervisor Professor Ghiringhelli for the opportunity to develop my thesis at the European Synchrotron Radiation Facility, a world-class centre of excellence for fundamental and innovation-driven research, and the ESRF itself for having hosted me.

I want to extend my gratitude to my two co-supervisors, Dr. Kurt Kummer and Dr. Marius Retegan, for assisting and supporting me throughout the all project, and for creating a calm but stimulating working environment. I would also like to thank the ID32, ID26, ID20 staff for the pleasant lunches and moments spent together.

I would like to thank my office colleague and friend Elisabetta, for always being there to answer my stupid questions and for all the coffee breaks. I definitely owe you a couple of them for the help.

Ringrazio tutti gli amici che mi hanno accompagnato in questi anni universitari. In particolar modo, Greta, Agnese, Matteo e Giordano, per le innumerevoli risate e le indimenticabili serate passate insieme in questi ultimi cinque anni. Alla fine, le feste più feste siamo noi!

Un ringraziamento speciale va soprattutto alle mie due fantastiche coinquiline, Celeste e Ludovica, per essere ormai la mia seconda famiglia a Milano, sempre presente sia nel momento del bisogno che per una spensierata serata di divertimento.

Desidero inoltre ringraziare Tamara, per le lunghe telefonate e il supporto morale costante nonostante la distanza geografica che spesso ci separa.

Infine, non finirò mai di ringraziare la mia famiglia, che ha sempre creduto in me, a cui devo la persona che sono oggi, e senza la quale tutto ciò non sarebbe stato possibile.

Contents

| | |
|---|-----------|
| Abstract | ii |
| Sommario | iv |
| Acknowledgements | vi |
| Introduction | 1 |
| 1 Modern methods of X-ray spectroscopy calculations and data analysis | 3 |
| 1.1 Density Functional Theory (DFT) | 3 |
| 1.2 Atomic multiplet theory | 5 |
| 1.3 Wannier functions as a bridge to connect DFT and multiplet theory | 8 |
| 1.4 Anderson model and Kondo interaction | 10 |
| 1.4.1 Anderson model | 11 |
| 1.4.2 Kondo interaction | 15 |
| 1.5 Multivariate Curve Resolution (MCR) - an unbiased method to analyse large X-ray spectroscopy datasets | 17 |
| 2 X-ray Spectroscopy Instrumentation | 23 |
| 2.1 X-ray absorption spectroscopy (XAS) | 24 |
| 2.2 Resonant Inelastic X-ray Scattering (RIXS) | 25 |
| 3 Temperature dependent valence in Yb and Ce Kondo lattice from X-ray spectroscopies - a test case for MCR | 28 |
| 3.1 Resonant X-ray emission on YbRh ₂ Si ₂ | 28 |
| 3.2 Soft X-ray absorption spectroscopy on Ce 122 systems | 37 |
| 4 Simulation on XAS and RIXS spectra of strongly correlated oxides from first principles | 69 |
| 4.1 NiO | 70 |

| | | |
|----------|-----------------------------|-----------|
| 4.1.1 | Band structure | 71 |
| 4.1.2 | XAS spectra | 72 |
| 4.1.3 | RIXS spectra | 73 |
| 4.2 | MnO | 74 |
| 4.2.1 | Band structure | 74 |
| 4.2.2 | XAS spectra | 75 |
| 4.2.3 | RIXS spectra | 75 |
| 5 | Summary and outlooks | 77 |
| | Bibliography | 79 |

List of Figures

| | | |
|------|--|----|
| 1.1 | Schematic plot of the f-spectral function $A_f(\omega)$ | 13 |
| 1.2 | Calculated n_f temperature evolution | 14 |
| 1.3 | Pressure dependence of valence on CeCu_2Si_2 | 15 |
| 1.4 | Doniach Phase diagram for heavy fermion compounds | 16 |
| 1.5 | Schematic representation of the bilinear model | 17 |
| 1.6 | Sample dataset - profile evolution | 20 |
| 1.7 | Sample dataset - Singular Value Decomposition | 20 |
| 1.8 | Sample dataset - PCA | 21 |
| 1.9 | Sample dataset - model fit | 22 |
| 2.1 | ID32 beamline floor plan | 24 |
| 2.2 | Direct RIXS process | 26 |
| 2.3 | Indirect RIXS process | 27 |
| 2.4 | ESRF ID32 RIXS branch | 27 |
| 3.1 | Crystal structure of YbRh_2Si_2 | 29 |
| 3.2 | YbRh_2Si_2 RXES temperature evolution | 29 |
| 3.3 | YbRh_2Si_2 RXES Singular Value decomposition | 30 |
| 3.4 | YbRh_2Si_2 PCA - pure variable selection | 31 |
| 3.5 | YbRh_2Si_2 model fit - pure variable selection | 32 |
| 3.6 | YbRh_2Si_2 PCA - custom initial guess | 33 |
| 3.7 | YbRh_2Si_2 model fit - custom initial guess | 34 |
| 3.8 | YbRh_2Si_2 PCA - Evolving Factor Analysis | 35 |
| 3.9 | YbRh_2Si_2 model fit - Evolving Factor Analysis | 36 |
| 3.10 | CeNi_2Si_2 Soft XAS temperature evolution | 40 |
| 3.11 | CeNi_2Si_2 Soft XAS Singular Value Decomposition | 40 |
| 3.12 | CeNi_2Si_2 two components PCA - pure variable selection | 41 |
| 3.13 | CeNi_2Si_2 four components PCA - pure variable selection | 41 |
| 3.14 | CeNi_2Si_2 two components model fit - pure variable selection | 42 |
| 3.15 | CeNi_2Si_2 four components model fit - pure variable selection | 43 |
| 3.16 | CeNi_2Si_2 two components PCA - custom initial guess | 44 |

| | | |
|------|--|----|
| 3.17 | CeNi ₂ Si ₂ two components model fit - custom initial guess . . . | 45 |
| 3.18 | CeNi ₂ Si ₂ two components PCA - Evolving Factor Analysis . . | 46 |
| 3.19 | CeNi ₂ Si ₂ four components PCA - Evolving Factor Analysis . . | 46 |
| 3.20 | CeNi ₂ Si ₂ two components model fit - Evolving Factor Analysis | 47 |
| 3.21 | CeNi ₂ Si ₂ four components model fit - Evolving Factor Analysis | 48 |
| 3.22 | CeRu ₂ Ge ₂ Soft XAS temperature evolution | 49 |
| 3.23 | CeRu ₂ Ge ₂ Soft XAS Singular Value Decomposition | 50 |
| 3.24 | CeRu ₂ Ge ₂ two components PCA - pure variable selection . . . | 51 |
| 3.25 | CeRu ₂ Ge ₂ three components PCA - pure variable selection . . | 51 |
| 3.26 | CeRu ₂ Ge ₂ two components model fit - pure variable selection . | 52 |
| 3.27 | CeRu ₂ Ge ₂ three components model fit - pure variable selection | 53 |
| 3.28 | CeRu ₂ Ge ₂ two components PCA - custom initial guess | 54 |
| 3.29 | CeRu ₂ Ge ₂ two components model fit - custom initial guess . . | 55 |
| 3.30 | CeRu ₂ Ge ₂ two components PCA - Evolving Factor Analysis . | 56 |
| 3.31 | CeRu ₂ Ge ₂ three components PCA - Evolving Factor Analysis | 56 |
| 3.32 | CeRu ₂ Ge ₂ two components model fit - Evolving Factor Analysis | 57 |
| 3.33 | CeRu ₂ Ge ₂ three components model fit - Evolving Factor Anal- ysis | 58 |
| 3.34 | SNIP algorithm | 60 |
| 3.35 | M ₄ edge 4 <i>f</i> ⁰ peaks temperature evolution from several ternary Ce compounds. | 62 |
| 3.36 | Zoomed version of figure 3.35 | 63 |
| 3.37 | M ₅ edge 4 <i>f</i> ⁰ peaks temperature evolution from several ternary Ce compounds. | 64 |
| 3.38 | Zoomed version of figure 3.37 | 65 |
| 3.39 | Normalized M ₄ edge 4 <i>f</i> ⁰ peaks temperature evolution from several ternary Ce compounds. | 67 |
| 3.40 | Normalized M ₅ edge 4 <i>f</i> ⁰ peaks temperature evolution from several ternary Ce compounds. | 68 |
| 4.1 | Unit cell and Quanta cluster of NiO | 70 |
| 4.2 | Band structure of NiO in the [−10, 10] eV energy range | 71 |
| 4.3 | NiO XAS at L _{2,3} edges | 72 |
| 4.4 | NiO RIXS with incident photon energy at 853 eV | 73 |
| 4.5 | Unit cell and Quanta cluster of MnO | 74 |
| 4.6 | Band structure of MnO in the [−10, 10] eV energy range . . . | 74 |
| 4.7 | MnO XAS at L _{2,3} edges | 75 |
| 4.8 | MnO RIXS with incident photon energy at 640 eV | 76 |

List of Tables

| | | |
|-----|--|----|
| 3.1 | R2 factors and max order of magnitude of residuals of MCR-ALS analysis on YbRh_2Si_2 | 37 |
| 3.2 | Ternary compounds based on Ce analyzed | 38 |
| 3.3 | Crystalline structure of CeNi_2Si_2 , CeNi_2Ge_2 , CeRu_2Si_2 , CeRu_2Ge_2 | 39 |
| 3.4 | R2 factors and max order of magnitude of residuals of MCR-ALS analysis on CeNi_2Si_2 | 49 |
| 3.5 | R2 factors and max order of magnitude of residuals of MCR-ALS analysis on CeRu_2Ge_2 | 59 |

Introduction

The following thesis deals with the project carried on from April 2019 to October 2019 with the group of scientists at the beamline ID32 of the European Synchrotron Radiation Facility (ESRF)

In this work, modern tools for data analysis and spectra simulation are used to investigate strongly correlated compounds.

Those compounds are based on transition or rare-earth metals, in which the 3d and 4f (or 5f) shell are partially occupied [1]. Indeed, they exhibit a strong Coulomb repulsion among electrons in those shells. This strong electron-electron interaction gives birth to many exotic properties such as superconductivity [2], metal-insulator transition [3], heavy fermion states [4].

However, no complete model taking into account all the possible interaction has been developed yet. Simple impurity models such as the Anderson model [5] are usually employed to describe strongly correlated systems. Therefore, employing modern tools to analyse data and simulate spectra could shed some light on the physics behind those compounds.

In the thesis work hereafter, Multivariate Curve Resolution method is used to analyse intermediate valence in heavy fermion systems. This method has been previously used in chemistry to separate different concentrations of substances inside a generic solution [6, 7]. Its power stems from the little a priori knowledge about the physical phenomena needed to analyse the data, making it virtually applicable to any field. Secondly, Density Functional Theory calculations are used to obtain physical parameters used in parametric spectra simulations. This implies an opposite approach to spectra simulations: usually simulated spectra are fitted to experimental data in order to obtain key parameters regarding the Coulomb repulsion or spin-orbit interaction. However, this fitting process does not always lead to unique or physical meaningful results. Therefore, exploring the possibility of using Density Functional Theory to calculate those parameters could be useful not only to test the correctness of the models, but also to better understand the experimental results [8].

Going into details about the contents, in chapter 1 a theoretical back-

ground of both the modern tools used and heavy fermion physics is given. Going further, in chapter 2 a brief description of the spectroscopic techniques will be presented. Then in chapter 3, the Multivariate Curve Resolution method presented in chapter 1 will be employed to study intermediate valence in Yb and Ce ternary intermetallic compounds. Eventually, in chapter 4 spectra simulations starting from Density Functional Theory calculation are presented.

Notably, chapters 3 and 4 are conceived with the aim to prove to the reader the validity of those tools in analysing data and simulating spectra, respectively.

Chapter 1

Modern methods of X-ray spectroscopy calculations and data analysis

1.1 Density Functional Theory (DFT)

Density Functional Theory (DFT) has been developed to investigate the electronic structure of compounds through computational quantum mechanical models. Thanks to the increasing computing performances in the last decades, DFT has become popular in condensed matter physics and solid-state physics since it allows good quality calculation with low computational costs and time with respect to other methods such as Hartree-Fock. In this chapter general concepts regarding DFT are introduced in order to better understand its implementation.

Let's consider a system composed by N interacting particles. The corresponding Hamiltonian would be [9]:

$$\hat{\mathcal{H}}[v] = -\frac{1}{2} \sum_{i=1}^N \nabla_i^2 + \sum_{i=1}^N v(x_i) + \frac{1}{2} \sum_{i \neq j}^N w(|\mathbf{r}_i - \mathbf{r}_j|) = \hat{T} + \hat{U} + \hat{W} \quad (1.1)$$

where the external potential v is a functional variable and \hat{W} is the correlation energy among the particles. The interaction-free Hamiltonian ($w = 0$) would be:

$$\hat{\mathcal{H}}^0[v] = -\frac{1}{2} \sum_{i=1}^N \nabla_i^2 + \sum_{i=1}^N v(x_i) \quad (1.2)$$

In the following, a superscript 0 indicates the interaction-free case. The

ground state energy is defined as

$$E[v] \triangleq \inf\{\langle \Psi | \hat{\mathcal{H}}[v] | \Psi \rangle \mid \Psi \in \mathcal{W}_N\} \quad (1.3)$$

where

$$\begin{aligned} \mathcal{W}_N \triangleq \{ \Psi \mid \Psi(x_1, \dots, x_N) \text{ (anti)symmetric,} \\ \langle \Psi | \Psi \rangle = 1, \langle \nabla_i \Psi | \nabla_i \Psi \rangle < \infty \text{ for } i = 1, \dots, N \}. \end{aligned} \quad (1.4)$$

Let's define the class of potentials

$$\mathcal{V}_N \triangleq \{ v \mid v \in \oplus L^p \text{ for some } p\text{'s, } \hat{\mathcal{H}}[v] \text{ has a ground state} \}. \quad (1.5)$$

Having defined the ground state energy and the class of potentials, it is possible to demonstrate the Hohenberg and Kohn theorem which states [9]

$v(x) \text{ mod } (const.) \in \mathcal{V}_N$ is a unique function of the ground state density $n(x)$

In other words, this theorem says it is possible to transfer any functional dependence on v into a functional dependence on n . Let's now define the density functional introduced by Hohenberg and Kohn as:

$$F_{\text{HK}}[n] \triangleq E[v[n]] - \int v[n] n dx, \quad n \in \mathcal{A}_N, \quad (1.6)$$

where \mathcal{A}_N is the class of densities defined as:

$$\mathcal{A}_N \triangleq \{ n(x) \mid n \text{ comes from an } N\text{-particle ground state} \}. \quad (1.7)$$

As a result, $F_{\text{HK}}[n]$ is unique and well defined on \mathcal{A}_N . Exploiting the theorem introduced above, it is possible to formulate the Hohenberg-Kohn variational principle

$$E[v] = \min_{n \in \mathcal{A}_N} \left\{ F_{\text{HK}}[n] + \int n v dx \right\}, \quad v \in \mathcal{V}_N \quad (1.8)$$

Therefore, minimizing the energy means finding the density of the ground state. However, a major problem remains: neither the classes \mathcal{V}_N and \mathcal{A}_N nor the functional F_{HK} are known explicitly. Here it is where the so-called Kohn-Sham equation comes into play. The clever idea of Kohn and Sham was to consider the case on non-interacting particle moving in an effective external potential that takes into account also the correlation among particles. In this framework it is possible to rewrite the HK functional as follows:

$$F_{\text{HK}}[n] = T[n] + E_H[n] + E_{XC}[n] \quad (1.9)$$

where $E_H[n]$ is the Hartree (Coulomb) energy and E_{XC} the residual interaction. Since the particles are not interacting, it is possible to separate the problem into N single particle Schrödinger equations:

$$\left(-\frac{\hbar^2}{2m}\nabla^2 + v_{eff}(x)\right)\phi_i(x) = \varepsilon_i\phi_i(x) \quad (1.10)$$

$$v_{eff}(x) \triangleq v_{ext}(x) + v_H(x) + v_{XC}(x) = v_{ext}(x) + e^2 \int \frac{n(x')}{|x-x'|} dx + \frac{\delta E_{XC}}{\delta n(x)} \quad (1.11)$$

where ε_i is the energy associated with the Kohn-Sham orbitals ϕ_i . Those orbitals are used to define the density

$$n(x) = \sum_i^N |\phi_i(x)|^2 \quad (1.12)$$

used in a self consistent method to minimize the following variational principle

$$E[v_{ext}] = \min_n \left\{ T[n] + \int n v_{ext} dx + E_H[n] + E_{XC}[n] \right\} \quad (1.13)$$

Once the energy is minimized and the set of KS orbital are found, it is possible to calculate the band structure of the ground state.

1.2 Atomic multiplet theory

In order to show how spectra in strongly correlated electronic systems are calculated, in this section, the atomic multiplet theory is presented. It is reasonable to start building the model from the atomic Hamiltonian and then introducing solid-state effects as perturbations. The Hamiltonian of a free atom with N electrons can be written as [10]

$$\mathcal{H}_{free} = \sum_{i=1}^N \left(-\frac{\hbar^2}{2m_e} \nabla_i^2 - \frac{Z_{eff}e^2}{r_i} + \zeta(r_i)\mathbf{l}_i \cdot \mathbf{s}_i \right) + \sum_{i<j}^N \frac{e^2}{|\mathbf{r}_i - \mathbf{r}_j|} \quad (1.14)$$

where, in order, the terms are: kinetic energy of the electrons, electrostatic potential energy of the nucleus charge screened by inner shells, spin-orbit interaction and Coulomb repulsion between two electrons on the same shell. The origin of the reference system is the position of the nucleus. Many-body Hamiltonians involving a mixture of coordinates are impossible to solve;

therefore, a central field approximation [11] can be adopted. In this framework, electrons feel an average spherical potential created by the other electrons. The resulting Hamiltonian will be

$$\mathcal{H}_{free} = \overbrace{\sum_{i=1}^N \left(-\frac{\hbar^2}{2m_e} \nabla_i^2 - \frac{Z_{eff} e^2}{r_i} + \left\langle \sum_{i<j}^N \frac{e^2}{|\mathbf{r}_i - \mathbf{r}_j|} \right\rangle \right)}^{\mathcal{H}_0} + \underbrace{\sum_{i<j}^N \frac{e^2}{|\mathbf{r}_i - \mathbf{r}_j|} - \left\langle \sum_{i<j}^N \frac{e^2}{|\mathbf{r}_i - \mathbf{r}_j|} \right\rangle + \sum_{i=1}^N \zeta(r_i) \mathbf{l}_i \cdot \mathbf{s}_i}_{\mathcal{H}'} \quad (1.15)$$

where the spin-orbit term and the remaining Coulomb interaction will be treated in a perturbative approach. Notice that in \mathcal{H}_0 there is no mixture of coordinates. Thus, the solution to the Schrödinger equation $\mathcal{H}_0 \Psi^0 = \epsilon^0 \Psi^0$ will be a linear combination of hydrogen-like atomic spin-orbitals $\psi_\tau(\mathbf{x})$, where τ labels the good quantum numbers n, l, m_l, m_s , and \mathbf{x} the spatial and spin coordinates. Since the unperturbed system described by \mathcal{H}_0 has spherical symmetry, the spatial dependent part of $\psi_\tau(\mathbf{x})$ can be written in terms of polar coordinates (r, θ, ϕ) :

$$\psi_\tau(r, \theta, \phi, \sigma) = R_{nl}(r) Y_l^{m_l}(\theta, \phi) \chi(\sigma) \quad (1.16)$$

where σ is the spin coordinate and $Y_l^{m_l}(\theta, \phi)$ are the so-called spherical harmonics.

In order to uphold the Pauli exclusion principle, the full antisymmetric many-electron wavefunction Ψ^0 is given by the Slater determinant of $\psi_\tau(\mathbf{x})$ [12]

$$\Psi^0(\mathbf{x}_1, \mathbf{x}_2, \dots, \mathbf{x}_N) = \frac{1}{\sqrt{N!}} \begin{vmatrix} \psi_{\tau_1}(\mathbf{x}_1) & \psi_{\tau_1}(\mathbf{x}_2) & \cdots & \psi_{\tau_1}(\mathbf{x}_N) \\ \psi_{\tau_2}(\mathbf{x}_1) & \psi_{\tau_2}(\mathbf{x}_2) & \cdots & \psi_{\tau_2}(\mathbf{x}_N) \\ \vdots & \vdots & \ddots & \vdots \\ \psi_{\tau_N}(\mathbf{x}_1) & \psi_{\tau_N}(\mathbf{x}_2) & \cdots & \psi_{\tau_N}(\mathbf{x}_N) \end{vmatrix}. \quad (1.17)$$

The resulting wavefunctions Ψ^0 can act as a basis in the perturbation theory to construct new wavefunctions to evaluate the first order energy correction due to the spin-orbit and Coulomb interactions. In the case of RE atoms those two interactions have the same order of magnitude, an intermediate coupling scheme for the momentum summation must be adopted, which can be derived from the LS coupling scheme [13].

The LS scheme is used when the spin-orbit interaction is smaller than the Coulomb repulsion. In those cases, the azimuthal and spin quantum numbers

are summed separately. Thus, the total orbital and spin momentum operators are $\mathbf{L} = \sum_i \mathbf{l}_i$ and $\mathbf{S} = \sum_i \mathbf{s}_i$ respectively. Moreover, the total quantum number operator is $\mathbf{J} = \mathbf{L} + \mathbf{S}$ which has $2J + 1$ degenerate eigenstates, each one labeled with the quantum number $M = -J, -J + 1, \dots, J - 1, J$. Those groups of eigenstates for different values of J are called multiplets. In the end, in the LS scheme, L, S, J are all good quantum numbers, making it convenient to label eigenstates with the Russel-Sanders notation $^{2S+1}L_J$. However, as aforementioned, for REs an intermediate coupling scheme should be adopted, where L and S are not good quantum numbers. Nevertheless, the LS eigenfunctions $|^{2S+1}L_J\rangle$ can be used as a basis to define a new set of eigenfunctions for the intermediate coupling scheme called free-ion wavefunctions [13]. Therefore, in the following description, in order to calculate the energy correction due to the Coulomb repulsion, spin-orbit interaction and crystal electric field, $|^{2S+1}L_J\rangle$ are used.

In perturbation theory, the first order energy correction due to the Coulomb repulsion among electrons will be:

$$\left\langle ^{2S+1}L \left| \mathcal{H}'_C \right| ^{2S'+1}L' \right\rangle = \sum_k f_k F^k + \sum_k g_k G^k. \quad (1.18)$$

The matrix element has been divided into four different contributions. Uppercase letters (F,G) refer to the radial parts, which are called Slater integrals: while lowercase letters (f,g) correspond to the angular part. The F terms represent the repulsion among electrons belonging to the same shell, and therefore are named direct Slater integrals; on the other hand, the G terms are linked to the interaction among electron on different shells, and are called indirect Slater integrals. Due to selection rules stemming from the conservation of the total angular momentum, in $3d^N$ configurations, only F^0, F^2, F^4 , are different from zero. Dealing with $L_{2,3}$ edges, the final state $2p^5 3d^{N+1}$ contains only F^0, F^2, F^4, G^1 and G^3 [14]. Those parameters can be either calculated or extracted as fitting parameters from experimental data.

Following the same perturbative approach as above, the first order correction due to spin-orbit coupling to the total energy of the unperturbed system would be:

$$\left\langle ^{2S+1}L_J \left| \mathcal{H}'_{SO} \right| ^{2S'+1}L'_{J'} \right\rangle = \zeta_{nl} A_{SO}(nl). \quad (1.19)$$

Also those parameters can be either calculated or extracted as fitting parameters from experimental data.

When the atom is placed inside a crystalline environment, the charge distribution of the other surrounding atoms creates a static electric field that breaks the spherical symmetry of the free atom system. This field splits the energetic levels of the atom lifting the $(2J + 1)$ fold degeneracy.

How these levels split depends on the local point symmetry on the atom. One possibility to model the interaction is to consider an effective crystal electric field potential $V_{CEF}(\mathbf{r})$ with the same symmetry of the surrounding crystalline environment [15]. The resulting Hamiltonian would be

$$\mathcal{H}_{CEF} = -eV_{CEF}(\mathbf{r}) \quad (1.20)$$

The crystal field potential can be expanded in terms of normalized spherical harmonics $C_k^m(\theta, \phi) = \sqrt{\frac{4\pi}{2k+1}}Y_k^m(\theta, \phi)$:

$$V_{CEF}(r, \theta, \phi) = \sum_{k=0}^{\infty} \sum_{m=-k}^k \tilde{A}_k^m r^k C_k^m(\theta, \phi) \quad (1.21)$$

where k and m are generic azimuthal and magnetic quantum numbers respectively.

In the framework of a perturbation theory, the first order correction to the atomic system involves the calculation of the matrix elements in the basis of $|^{2S+1}L_J\rangle$ [15, 13]:

$$\begin{aligned} \left\langle ^{2S+1}L_{J,M} \left| \mathcal{H}_{CEF} \right| ^{2S'+1}L'_{J',M'} \right\rangle &= \\ &= \sum_{k=0}^{\infty} \sum_{m=-k}^k A_k^m (-1)^{J-M} \begin{pmatrix} J & k & J' \\ -M & m & M' \end{pmatrix} D_J^k \end{aligned} \quad (1.22)$$

where the 3j formalism [16] has been used and $A_k^m \propto \tilde{A}_k^m \langle r^k \rangle$. Depending on the point group symmetry of the crystal, only for specific values of k and m the radial integral in A_k^m will survive. The value of A_k^m are usually obtained from calculations or found fitting the experimental data [13].

1.3 Wannier functions as a bridge to connect DFT and multiplet theory

In a periodic crystal, the eigenstates of the Hamiltonian operator in periodic boundary condition are Bloch waves $|\Psi_{n\mathbf{k}}\rangle$:

$$\Psi_{n\mathbf{k}} = e^{i\mathbf{k}\cdot\mathbf{R}} u_{n\mathbf{k}}(\mathbf{r}) \quad (1.23)$$

Let's consider an isolated band. To build a localized wave packet around a specific atom/ion, a superposition of Bloch waves over a wide range of

\mathbf{k} is needed. Therefore, a Wannier function (WF) localized in the cell \mathbf{R} associated with the band n is built as [17]:

$$|W_{\mathbf{R}n}\rangle = \frac{V}{(2\pi)^3} \int_{1BZ} e^{-i\mathbf{k}\cdot\mathbf{R}} |\Psi_{n\mathbf{k}}\rangle d\mathbf{k}. \quad (1.24)$$

Wannier functions are not eigenstates of the Hamiltonian. However, they still contain some information about the charge density: the density obtained by summing the squares of Bloch or Wannier functions is the same [18]. By definition, it is possible to redefine a Bloch wave as follows:

$$|\tilde{\Psi}_{n\mathbf{k}}\rangle = e^{i\varphi_n(\mathbf{k})} |\Psi_{n\mathbf{k}}\rangle \quad (1.25)$$

without changing the physical description of the system. Notice how this gauge freedom propagates into the WFs through eq. 1.24 as well. Therefore, different transformation gauges imply different sets of WFs, making the WFs not unique at all. A suitable choice could be a smooth gauge such as $\nabla_{\mathbf{k}} |u_{n\mathbf{k}}\rangle$, since smoother functions on the reciprocal space result in more localized functions in the real space [18], which in this case are the WFs.

In many crystals, internal degeneracy and/or crossing of bands is quite common; there usually exists a manifold of J bands separated by an energy gap with respect to higher or lower bands. In these cases, using single band Bloch waves as in eq. 1.24 will lead to not well-localized WFs. Indeed, it is important to study the multiband case. The gauge transformation in eq. 1.25 can be generalized in

$$|\tilde{\Psi}_{n\mathbf{k}}\rangle = \sum_{m=1}^J U_{mn}^{(\mathbf{k})} |\Psi_{m\mathbf{k}}\rangle, \quad (1.26)$$

where U is a unitary matrix of dimension of J , periodic in \mathbf{k} . Equation 1.24 becomes

$$|W_{\mathbf{R}n}\rangle = \frac{V}{(2\pi)^3} \int_{1BZ} e^{-i\mathbf{k}\cdot\mathbf{R}} \sum_{m=1}^J U_{mn}^{(\mathbf{k})} |\Psi_{m\mathbf{k}}\rangle. \quad (1.27)$$

Well-localized WFs now depend on the choice of U . One way to make sure that the resulting $|\tilde{\Psi}_{n\mathbf{k}}\rangle$ will be smooth enough is to use the so-called projection technique.

Let's consider a manifold of J bands and pick a set of J test functions $\chi_n(\mathbf{r})$ in the home unit cell. These test functions usually are simple functions located where the expected WFs should be centered and with a similar angular character. These $\chi_n(\mathbf{r})$ are projected onto Bloch waves corresponding to the multiband set, obtaining:

$$|\phi_{n\mathbf{k}}\rangle = \sum_{m=1}^J |\Psi_{m\mathbf{k}}\rangle \langle \Psi_{m\mathbf{k}} | \chi_n \rangle \quad (1.28)$$

The resulting wavefunctions are typically smooth in the k space. The new states can be constructed through Löwdin-orthonormalization [18] as follows:

$$|\tilde{\Psi}_{n\mathbf{k}}\rangle = \sum_{m=1}^J |\phi_{m\mathbf{k}}\rangle (S_{\mathbf{k}}^{-\frac{1}{2}})_{mn} \quad (1.29)$$

where $(S_{\mathbf{k}})_{mn} = \langle \phi_{m\mathbf{k}} | \phi_{n\mathbf{k}} \rangle_{UC}$ (UC stands for unitary cell). Substituting the new set of Bloch waves $|\tilde{\Psi}_{n\mathbf{k}}\rangle$ in eq. 1.24, will create well-localized WFs resembling atomic orbitals centered in the ions locations. In the end, assuming the equivalence between the WFs just defined and the atomic orbitals described in section 1.2, from the WFs is possible to obtain useful parameters used in calculation and simulations such as Slater integrals, crystal electric field or hoppings strength among different orbitals.

1.4 Anderson model and Kondo interaction

In recent years rare-earth (RE) compounds based on Ce have aroused a significant interest among the solid-state research community due to their exotic properties. These compounds display different ground states: magnetic ordering, unconventional superconductivity [19], heavy-fermion behavior [20], Kondo lattices [21] and mixed-valence states [22] have been reported. On top of that, these physical properties can be easily controlled by changing pressure [23], temperature [24], stoichiometry, external field [25]. Of particular interest in this thesis are intermetallic systems in which the RE element exhibits a mixed-valence state depending on its physical and chemical environment.

Atomic Ce has a $[\text{Xe}]4f^15d^16s^2$ electronic configuration. In solids, the $5d$ and $6s$ hybridize together generating bands, becoming delocalized. On the contrary, the $4f$ shell, extending less than the two aforementioned shells, remains localized around the ion, and so do the $4f$ electrons. However, in some intermetallic compounds, Ce shows a trivalent state in which the occupation of the $4f$ orbitals is not stable. Because of their interaction with the surrounding conduction electrons, Ce ions display a mixture of $4f^0$ and $4f^1$ configurations, leading to a not integer n_f occupation number of the f shell. A complete model that takes into account all possible effects and interactions occurring in a heavy fermion crystal systems has not been developed yet. However, for the seek of this thesis, a basic model able to describe qualitatively the origin of the mixed-valence regime is enough. In this chapter, a brief description of the atomic model will be presented, followed by the Anderson impurity model. Then an overview of the Kondo interaction will be

presented, and finally the qualitative temperature and pressure dependence of the occupation number will be discussed.

1.4.1 Anderson model

In the case of RE elements, the multiplet theory described in section 1.2 works under the assumption of weakly-interacting and well-localized f shells. However, for the sake of this thesis, it is important to study the hybridization of the $4f$ shell with its surroundings. In order to do that, let's restart from the atomic Hamiltonian but only taking into account a unitary occupation of the f shell. The resulting atomic Hamiltonian will be

$$\mathcal{H}_{atomic} = \varepsilon_f n_f + U n_f^\uparrow n_f^\downarrow \quad (1.30)$$

where U is the Coulomb repulsion energy between two electrons in the same $4f$ shell. Let's now consider the energy cost of the following four states in the atomic model:

$$\begin{aligned} |f^2\rangle \quad E(f^2) &= 2\varepsilon_f + U \\ |f_\uparrow^1\rangle \quad E(f^1) &= \varepsilon_f \\ |f_\downarrow^1\rangle \quad E(f^1) &= \varepsilon_f \\ |f^0\rangle \quad E(f^0) &= 0 \end{aligned} \quad (1.31)$$

Thus, the cost for adding an electron would be $E(f^2) - E(f^1) = \varepsilon_f + U > 0$, while the cost for removing an electron is $E(f^0) - E(f^1) = -\varepsilon_f > 0$. So, for

$$-U < \varepsilon_f < 0 \quad \text{or} \quad -U/2 < \varepsilon_f + U/2 < U/2 \quad (1.32)$$

the local moment will be well defined and there will be valence fluctuations provided that $k_\beta T > \max(-\varepsilon_f, \varepsilon_f + U)$. However, in the compounds in study, the Coulomb repulsion between $4f$ electron is really strong and, since very low temperature conditions are here considered, that is not enough to explain a mixed-valence.

The intermediate valence regime at low temperatures in Ce materials can be described with the Anderson model, which takes into account both the hybridization between the $4f$ orbitals and the conduction band and the strong Coulomb repulsion between $4f$ electrons.

In 1961, Anderson developed a model for magnetic alloys to better describe localized magnetic states. The simplest version of the Anderson Hamiltonian can be used to characterize the hybridization of the $4f$ shell with the

conduction band. Thus, the Hamiltonian can be written as follows:

$$\mathcal{H}_A = \underbrace{\sum_{k,\sigma} \varepsilon_k c_{k\sigma}^\dagger c_{k\sigma}}_{\mathcal{H}_{band}} + \underbrace{\varepsilon_f \sum_{i,\sigma} f_{i\sigma}^\dagger f_{i\sigma} + U \sum_i n_{f,i}^\uparrow n_{f,i}^\downarrow}_{\mathcal{H}_{4f}} + \underbrace{\sum_{i,k,\sigma} [V(\mathbf{k}) c_{k\sigma}^\dagger f_{i\sigma} + \text{H.c.}]}_{\mathcal{H}_{hybr}} \quad (1.33)$$

where $n_{f,i}^\sigma = f_{i\sigma}^\dagger f_{i\sigma}$, and $V(\mathbf{k}) = \langle \mathbf{k} | V_{atomic} | f \rangle$ measures the hybridization between the localized 4f electrons and the conduction band (Bloch wave). The Anderson Hamiltonian has two main contributions: the 4f atomic Hamiltonian \mathcal{H}_{4f} introduced before, and a second Hamiltonian $\mathcal{H}_{band} + \mathcal{H}_{hybr}$ completely describing the conduction electrons and their interaction with the 4f shell. Notice that U and $V(\mathbf{k})$ are the key parameters of the atomic and conduction electron Hamiltonians respectively. Having already discussed the atomic case, let's focused on the hybridization.

The second component of the Anderson Hamiltonian

$$\mathcal{H}_{resonance} = \sum_{k,\sigma} \varepsilon_k c_{k\sigma}^\dagger c_{k\sigma} + \sum_{i,k,\sigma} [V(\mathbf{k}) c_{k\sigma}^\dagger f_{i\sigma} + \text{H.c.}] \quad (1.34)$$

will model the conduction electron and, for a reason that will be clarified soon after, it can be called the resonance Hamiltonian. The 4f local impurity potential is not sufficiently attractive to create a bound state below the conduction band. However, due to the resonant scattering, the local impurity tends to localize the conduction electron in its vicinity, inducing the formation of a virtual bound state. Therefore, the f-states broaden, producing a resonance of width

$$\Delta = \pi \sum_{\mathbf{k}} |V(k)|^2 \delta(\varepsilon_{\mathbf{k}} - \mu) = \pi V^2 \rho \quad (1.35)$$

In order to see how the Anderson Hamiltonian induces a mixed-valence state, it is useful to introduce the f-spectral function $A_f(\omega)$, which is the Fourier transform of the time-ordered f-Green's function. In $A_\omega(f)$, positive energies ($\omega > 0$) refer to the energy distribution for electron addition; while the negative part ($\omega < 0$) determines the energy distribution for removing an electron.

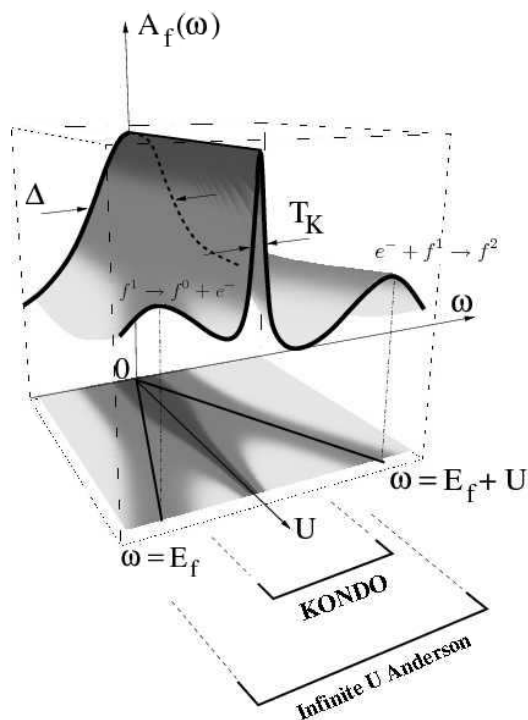


Figure 1.1: Schematic plot displaying the f -spectral function $A_f(\omega)$ as the Coulomb interaction U is increased (the occupancy of the f -shell is kept constant). At $U=0$ (non-interaction resonance), the broadening of the f -shell is purely due to the hybridization with the conduction band. When $U \gg \Delta$, A_f splits into three peaks: the two $|f^0\rangle$, $|f^2\rangle$ configurations separate in energy, and the Kondo resonance appears just below the Fermi energy. Image taken from [26]

By looking at Fig. 1.1, as one could expect at $U = 0$, there is only one broad peak whose width is Δ . However, As U is increased, the atomic contribution starts to grow and three peaks appear: the two lateral peaks are related to $4f^0$ and $4f^2$, while the central peak is often called "Kondo resonance". This resonance stems from the quantum spin fluctuation of the localized $4f^1$. From the $A_f(\omega)$ is possible to calculate the f -shell occupancy by considering its distribution below the Fermi energy

$$\langle n_f \rangle = N \int_{-\infty}^{E_f} A_f(\omega) d\omega \quad (1.36)$$

where N is the degeneracy.

In many materials where the Ce ion is in the $4f^1$ state, the $\langle n_f \rangle$ is slightly below unity; however, if the Kondo resonance is wide enough, the compounds tend more to a mixed-valence state, where the occupancy of the f -shell deviate from unity [26].

Some general behaviors of the n_f have been calculated from the Anderson impurity model or measured with different techniques. In Fig. 1.2 calculations of the temperature dependence of n_f are reported from [27]. Notice that as the temperature increases, the occupancy of the f shell tends towards unit since more $|f^1\rangle$ states become thermally populated.

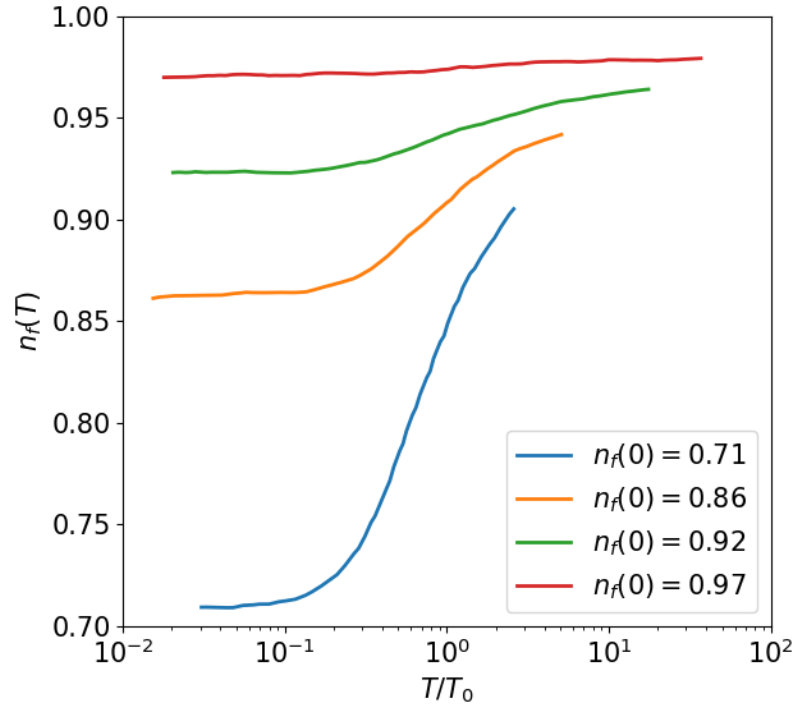


Figure 1.2: Calculated temperature variation of the occupation number of the f shell. T_0 is defined to be the position of the Fermi surface resonance in the f-spectral function for $T \rightarrow 0$. Data taken from [27]

In Fig. 1.3 the f-electron occupancy per site $\bar{n}_f = n_f/2$ are reported from [23]. Data were obtained from XAS spectra of CeCu_2Si_2 measured at different pressures at 14 K.

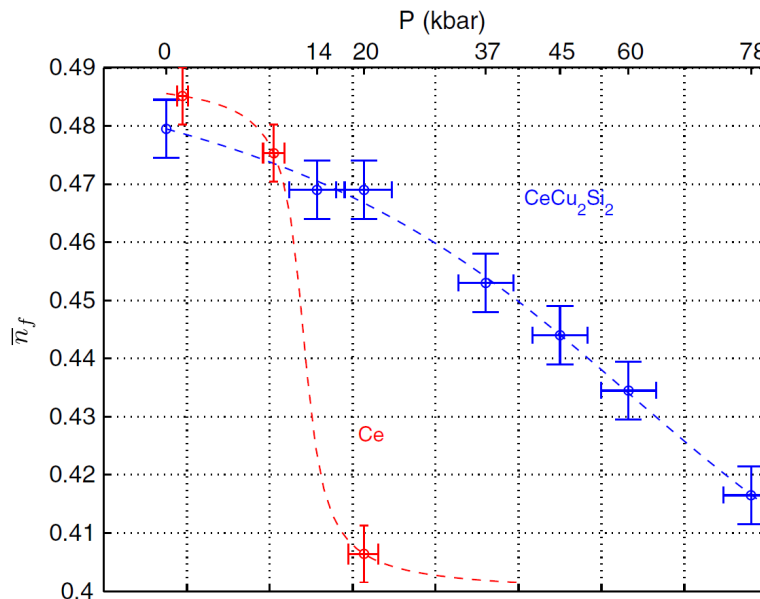


Figure 1.3: f-electron number per site $\bar{n}_f = n_f/2$ as function of pressure (top scale) and dimensionless energy scale ϵ_f/D as used in [28] (bottom scale, D is the Fermi energy of the conduction electrons as "if they were uncoupled with f electrons" [23]). Data borrowed from [23].

1.4.2 Kondo interaction

Many Ce compounds exhibit different types of ground state at low temperatures: antiferromagnetic, ferromagnetic or paramagnetic ground states might arise [29, 30, 31, 32]. These states can be described in terms of the competition between the RKKY and Kondo interactions. The former favors long-range magnetic order: the coupling among magnetic moments is conveyed by the surrounding conduction sea; the latter localizes conduction electrons around the $4f$ magnetic moments, effectively generating a singlet state and therefore screening the local magnetic moment of the ion. The characteristic temperatures of those two effects scale differently with respect to both the density of states at the Fermi energy $D(E_F)$ and the spin coupling interaction J between the $4f$ and conduction electrons:

$$T_K \propto \exp \left[-\frac{1}{JD(E_F)} \right] \quad (1.37)$$

$$T_{RKKY} \propto D(E_F)J^2 \quad (1.38)$$

As one can see in Fig. 1.4, for small values of J , the RKKY interaction

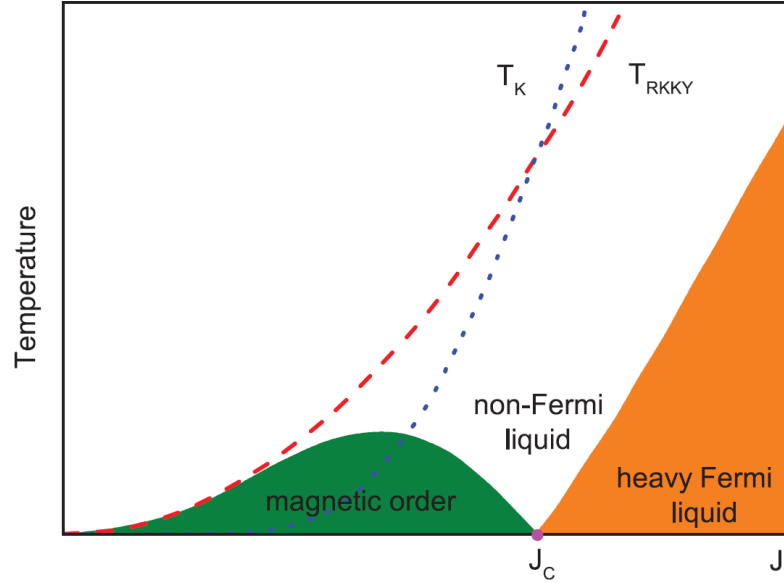


Figure 1.4: Doniach Phase diagram for heavy fermion compounds. The red dashed line and the blue dot lines are the T_{RKKY} and T_K evolution respectively. For $J < J_c$, $T_{RKKY} > T_K$ and therefore a magnetically ordered ground state is favored (green area); while for $J > J_c$, $T_{RKKY} < T_K$, and so, provided that the temperature is low enough, a heavy fermion ground state appears (orange area). Image takes from [33]

is dominant ($T_K < T_{RKKY}$), and so the ground state would be magnetically ordered; on the order hand, when J is above a critical value J_c ($T_K > T_{RKKY}$), the Kondo effect overcomes the RKKY interaction leading to a disordered ground state and, if the temperature and external magnetic field are low enough, the system exhibits a paramagnetic heavy Fermi liquid state. In order to understand how the Kondo effect could lead to the formation of a heavy fermion state, let's take into account how the resistivity of these compounds changes at very low temperatures.

Suppose to have $J > J_c$, so that the Kondo interaction prevails. As the temperature decreases, the resistivity drops until the first isolated magnetic ions start to be "quenched" by the Kondo effect. Indeed, the newly created singlet states act as a scattering source for conduction electrons, effectively increasing the resistivity. However, since the ions are arranged in a periodic lattice, as the temperature continues to decrease, the scattering becomes coherent, leading to a sudden drop in the resistivity at very low temperatures. In this coherent state, electrons show an increased effective mass, almost 1000 times larger than the free electron mass. The situation in which the Kondo effect develops coherence among all the impurities and a heavy electron band is formed is referred as "Kondo lattices".

1.5 Multivariate Curve Resolution (MCR) - an unbiased method to analyse large X-ray spectroscopy datasets

Multivariate Curve Resolution (MCR) methods can find interesting applications in spectroscopy due to their ability to extract pure components of spectra without any previous knowledge or model of the physical phenomenon. They are based on a bilinear model decomposition which separates the experimental spectra in a linear combination of principal components. The bilinear model can be written as [34]:

$$\mathbf{D} = \mathbf{C}\mathbf{S}^T + \mathbf{E} \quad (1.39)$$

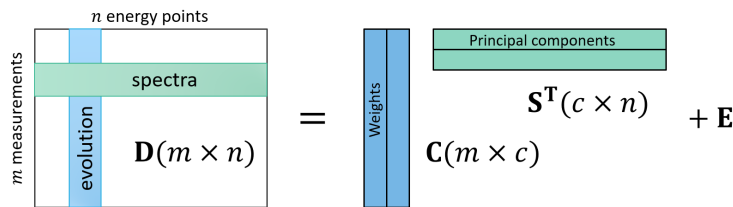


Figure 1.5: Schematic representation of the bilinear model

where:

- \mathbf{D} is a $m \times n$ matrix containing m measurements taken over n energy points;
- \mathbf{C} is a $m \times c$ matrix containing the weights of the principal components for each measurement;
- \mathbf{S} is a $c \times n$ matrix containing the first c principal components (PCs) of the spectra ($c \leq m$);
- \mathbf{E} is the matrix of residuals not explained by the resolved components.

The number of relevant PCs can be both selected manually, or guessed via the Singular Value Decomposition (SVD) algorithm.

The SVD is a generalization of the eigendecomposition of a square matrix. Suppose \mathbf{A} is a $n \times m$ matrix, then it is possible to factorize \mathbf{A} as follows [35]:

$$\mathbf{A} = \mathbf{U}\mathbf{\Sigma}\mathbf{V}^T \quad (1.40)$$

where:

- \mathbf{U} is a $n \times n$ unitary matrix whose columns \vec{u}_i are a set of orthonormal vectors;
- $\mathbf{\Sigma}$ is $n \times m$ matrix, whose diagonal elements σ_i are non-negative real numbers called singular values;
- \mathbf{V} is a $m \times m$ unitary matrix whose columns \vec{v}_i are also a set of orthonormal vectors.

The singular values σ_i are ordered in a decreasing order along the main diagonal, and it is possible to associate each σ_i with a PC. To σ_1 , the highest singular value, is associated the PC that covers most of the variance of the data; to σ_2 the second PC that explains the second largest percentage of the variance, and so on.

Having no prior knowledge on the origin of the data, principal component analysis (PCA) does not take into account any physical constraint: in this thesis work, PCs are absorption spectra, and so their intensity must be positive. Luckily, the \mathbf{D} matrix decomposition into \mathbf{C} and \mathbf{S} is not unique. Therefore, it is possible to exploit the so-called rotational ambiguities and define a rotation matrix \mathbf{T} to generate a new pair of \mathbf{C}_{new} and \mathbf{S}_{new} matrices as follows [36]:

$$\mathbf{D} = \mathbf{C}\mathbf{S}^T + \mathbf{E} = \mathbf{D}^* + \mathbf{E} \quad (1.41)$$

$$\mathbf{S}_{new}^T = \mathbf{T}\mathbf{S}^T \quad (1.42)$$

$$\mathbf{C}_{new} = \mathbf{C}\mathbf{T}^{-1} \quad (1.43)$$

$$\mathbf{D}^* = \mathbf{C}\mathbf{S}^T = \mathbf{C}_{new}\mathbf{S}_{new}^T \quad (1.44)$$

By properly defining \mathbf{T} , it is possible to apply different constraints to both pure spectra components and their weights (i.e. non-negativity). In order to find the best \mathbf{T} , an optimization method is used. Firstly, initial estimations of \mathbf{C} , \mathbf{S} and \mathbf{T} are made: \mathbf{T} will be an identity matrix whose dimension is equal to the number of PCs (\mathbf{C} and \mathbf{S} estimation methods will be briefly described later). Then, the two LS equations $\min_{\mathbf{C}} \|\mathbf{D} - \mathbf{C}_{new}\mathbf{S}_{new}^T\|$ and $\min_{\mathbf{S}^T} \|\mathbf{D} - \mathbf{C}_{new}\mathbf{S}_{new}^T\|$ are alternated and solved iteratively, applying the selected constraints at each iteration [36].

Regarding the initial estimation of \mathbf{C} and \mathbf{S} , there are three possible paths to follow: they can be either be a sensible initial guess or be obtained from pure variable detection and evolving factor analysis (EFA) methods [34]. Let's focus on the last two. Pure variable detection method aims at selecting the most dissimilar rows or columns in a single data matrix or a multiset structure providing initial estimates of spectra or of concentration

profiles, respectively. On the other hand, EFA method exploits the emergence and decay of the components in datasets. Assuming a sequential order of emergence/decay for all components in the system, this method provides a suitable initial estimation of the concentration profiles. In order to assess which method leads to the best results, two parameters related to the model fit can be taken into account. The first is R-squared (R2) which represents the percentage of the total variance explained by the principal component selected; the second one are the residuals, which contains the residual part of the experimental spectra not reconstructed by the principal components. In the end, good quality result are the ones with the R2 factor close to 100% and the low residuals.

To better understand how it works, an example will be reported in the following. In order to test the algorithm, a dataset was manually generated: the general profile is composed of six gaussian with different μ and σ . In figure 1.6, The evolution of the profile with respect to a generic variable that ranges between 0 and 100 is plotted. Counting the peaks from left to right, the intensities of the 1st and 4th peaks decrease linearly as X increases; whereas the remaining peaks have their intensity linearly increased as X rises from 0 to 100.

Let's start with the singular value decomposition reported in figure 1.7. As one can clearly see, there are only two singular values much greater than zero; therefore, only two PCs will be considered.

Regarding the initial guess, the pure variable selection method is employed. Moreover, no constraints are used, so that the simplest analysis can be performed. The results of the PCA are reported in figure 1.8. Notably, the PCA is able to correctly reconstructed both the shape and intensity evolution of the six gaussian. The algorithm has correctly grouped gaussian with the same evolution in the same principal component. Moreover, it has retrieved the linear dependence of the intensities over X.

Let's now look at the model fit reported in figure 1.9

The model fit is perfect with a R2 factor of 100% and residuals of the order of machine epsilon (10^{-16}).

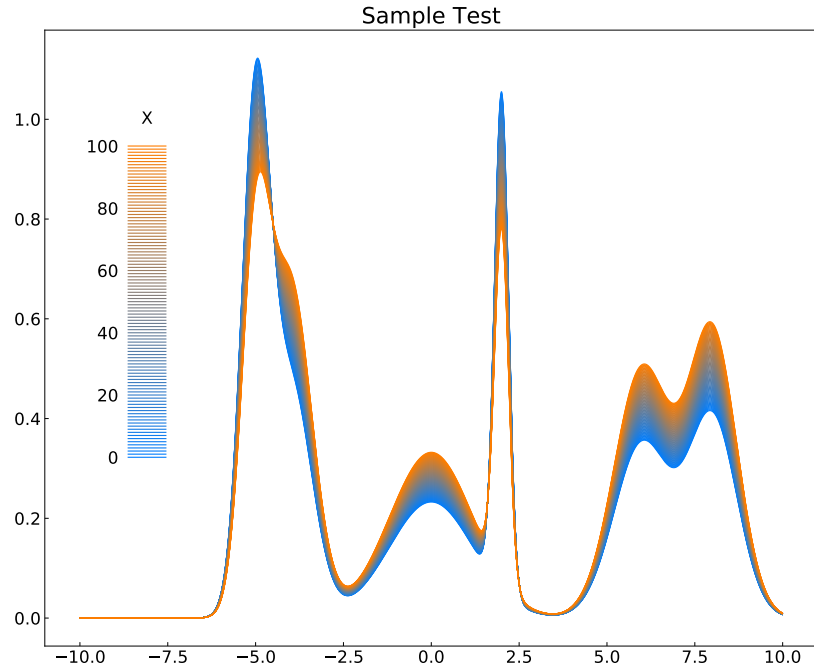


Figure 1.6: Sample data generated to test the MCR-ALS. The general profile is the sum of six gaussian with different μ and σ ; the weight of each gaussian changes with respect to another variable whose values range from 0 to 100.

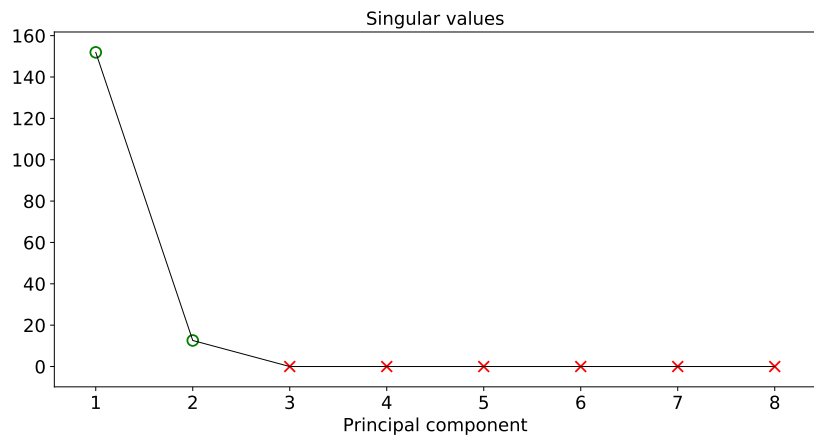


Figure 1.7: Singular Value decomposition of the sample dataset.

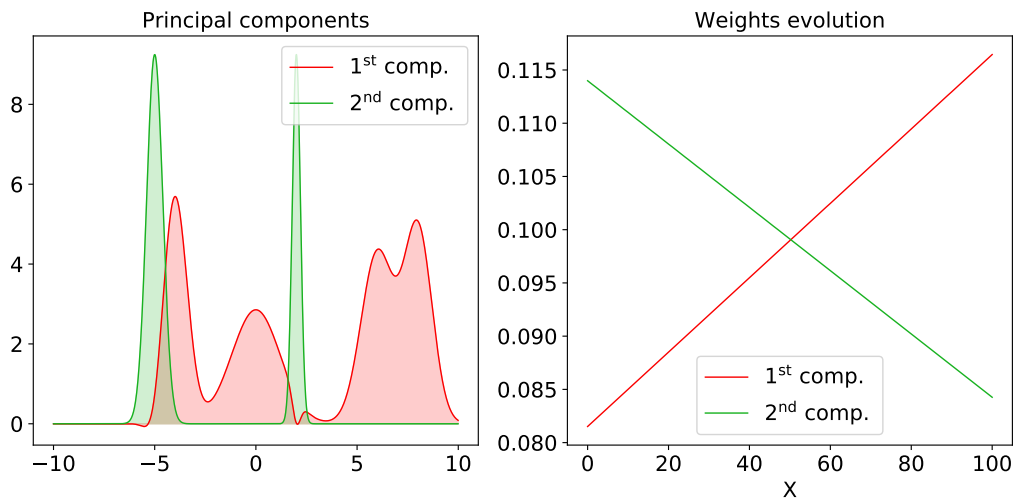


Figure 1.8: Principal component analysis of the sample dataset. Notably, the PCA was able to correctly group together the gaussian with the same evolution into two principal components. Moreover, the linear dependence on X is reconstructed in the evolution of the weights associated with the PCs

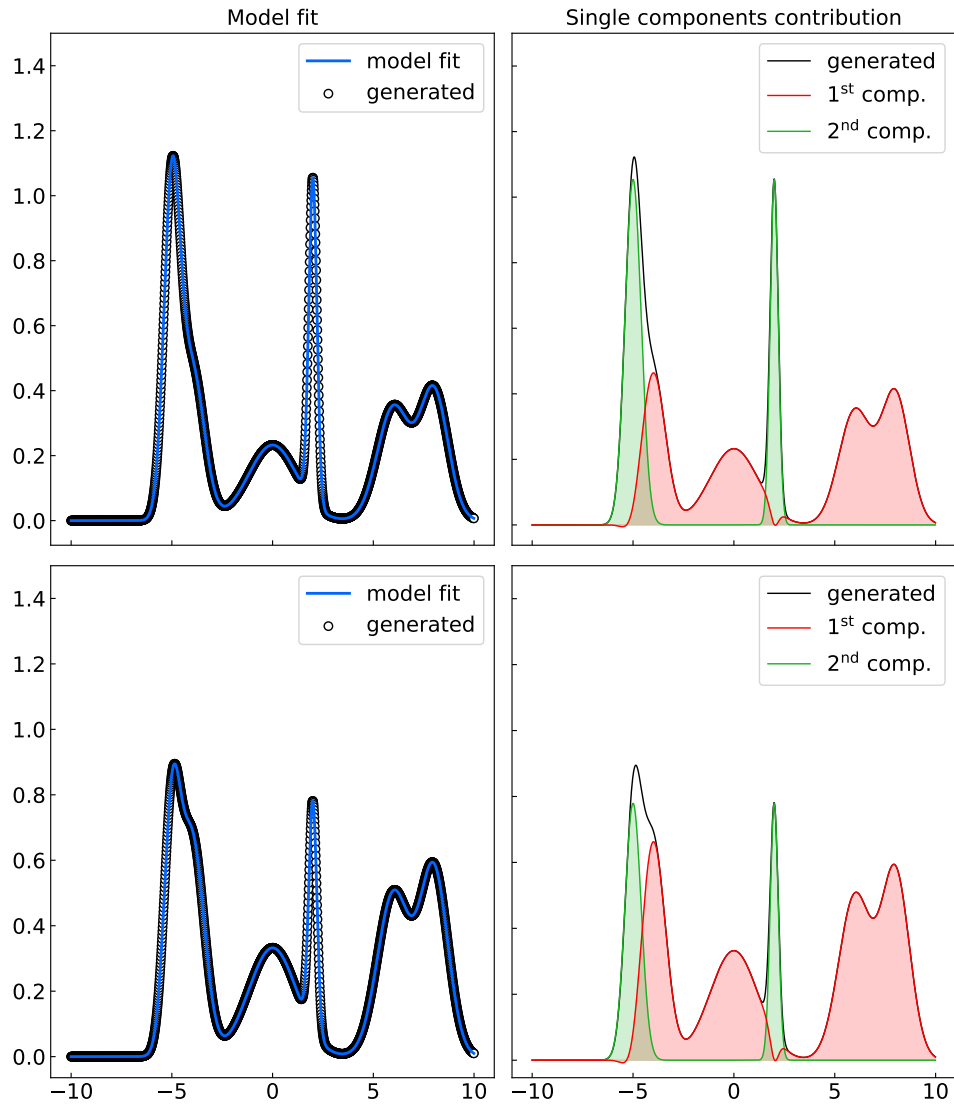


Figure 1.9: Model fit on the sample dataset. The fit is perfect: the resulting R2 factor is 100% and the residuals are of the order of the machine epsilon (10^{-16})

Chapter 2

X-ray Spectroscopy Instrumentation

Spectroscopy techniques involving X-rays are powerful tools to investigate the electronic and optical properties of solids: the importance of X-rays lies in their ability to excite core level electrons. Core level spectroscopy allows extracting information about the local environment around specific elements inside solids. Synchrotron facilities play a key role in experimental studies of core level spectroscopy: thanks to technological improvements, synchrotron radiation source have reached brilliance comparable to lasers [37].

The Soft X-Rays Spectroscopies Beamline at ESRF is a state-of-the-art beamline dedicated to X-Ray absorption (XAS), Resonant Inelastic X-Rays Scattering (RIXS) and X-Rays Magnetic Dichroism (XMCD and XMLD) experiments. The 400eV/1600eV energy range allows to measure absorption edges of different elements. The beamline has two branches: one is designed for XMCD and XMLD studies, with high sensitivity, reproducibility, flexibility, user friendliness and the capability for fast energy scanning. The second branch is designed for high energy resolution RIXS experiments with a combined resolving power up to 30000 around 930 eV. [38] In order to perform XMCD and RIXS measurements, the X-ray source must have tunable polarization (both linear and circular) and very high intensity, since RIXS experiments are flux hungry techniques. In order to achieve that, three APPLE-II undulators are employed, which are able to provide a polarization close to 100% over the 400/1600 energy range. Undulators are insertion devices composed of four arrays of permanent magnets ordered in a specific way. By sliding horizontally the arrays, the user can obtain different polarizations, while by changing the gap between the block of array, it is possible to change the frequency of the emitted light. In Fig.2.1 the ID32 beamline floor plan is reported from [38]. The radiation exiting the undulators impinges

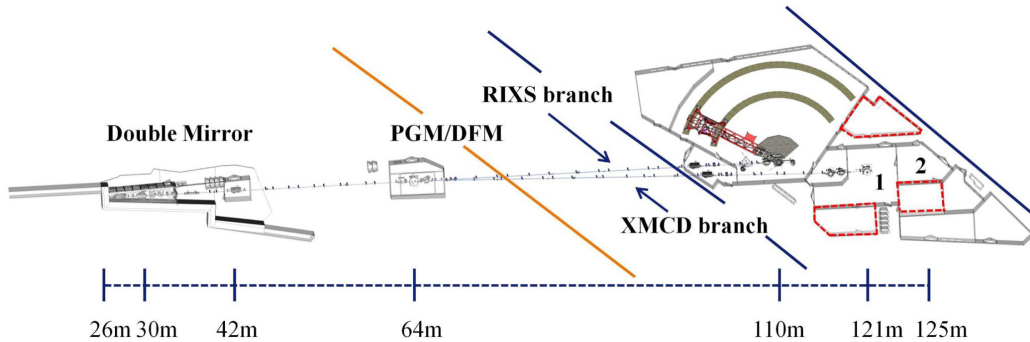


Figure 2.1: ID32 beamline floor plan

on a double mirror. This mirror has two major tasks: firstly it shifts the beam horizontally by 16 mm, allowing the deployment of a Bremsstrahlung stopping device; secondly, it adsorbs unwanted high energies radiations, effectively reducing the heat load on the entrance slit and monochromator optics. In order to assure the same degree of monochromaticity over the wide energy range, variable line spacing (VLS) plane gratings are used. In the following sections, a brief description of the XAS and RIXS experimental techniques and related instrumentation will be provided.

2.1 X-ray absorption spectroscopy (XAS)

XAS allows to probe electronic transitions from ground states to core excited states. Within the electric dipole approximation, the transition rate from an initial ground state $|i\rangle$ to a final core excited state $|f\rangle$ will be [11]:

$$W_{fi} \propto \sum_{\mathbf{s}} |\langle f | \mathbf{e}_s \cdot \mathbf{r} | i \rangle|^2 \delta(E_f - E_i - \hbar\omega) \quad (2.1)$$

where the sum index \mathbf{s} stand for the different polarization of the photon and δ provides the energy conservation.

The transition rate will be zero whenever the integral $\langle f | \mathbf{e}_s \cdot \mathbf{r} | i \rangle$ is zero; to avoid that, the integrand function must be even. In order to achieve that, being the transition operator an odd function, $|i\rangle$ and $|f\rangle$ must have different parity. Within the atomic multiplet theory, this parity constraint generates selection rules quantum numbers must obey. Considering only first order absorption events (single photon absorption) and assuming to use linearly polarized photons, which have the orbital quantum number equal to 1 and

spin equal to 0, the selection rules are the following [11]:

$$\begin{aligned} \Delta l = \pm 1, \Delta s = 0, \Delta J = 0, \pm 1, \text{ with } J_i + J_f \geq 1 \\ \Delta m_l = 0, \pm 1, \Delta m_s = 0 \end{aligned} \quad (2.2)$$

These selection rules are essential to explain and understand XAS spectra since each absorption edge is linked to different allowed transitions between the initial ground state and the final core excited state. Indeed, the energy of the absorption edge will be determined by δ , while the intensity will be proportional to the probability of the transition (matrix element squared) and the density of empty states ρ :

$$I_{XAS} \sim |\langle f | \mathbf{e}_s \cdot \mathbf{r} | i \rangle|^2 \rho. \quad (2.3)$$

Two different methods have been employed to measure XAS: total fluorescence yield (TFY) and total electron yield (TEY). As the name suggests, the TFY mode measures the photons created by the fluorescence decay of the core hole: those photons have a mean free path of the same order of magnitude of the impinging photon, so no surface effects appear. However, if the sample is not dilute, a resonance effect that leads to re-absorption could arise. As a consequence of that, some saturation effects might occur in the most intense peaks. On the other hand, TEY mode detects all the electrons exiting the sample by measuring the current flowing into the sample. Since it is not possible to distinguish the origin of those electrons (Auger or secondary electrons), the probing depth is not precise. Nevertheless, this disadvantage is compensated by the ease of acquisition and large signal.

2.2 Resonant Inelastic X-ray Scattering (RIXS)

RIXS is a photon-in photon-out second order optical process that involves a coherent absorption and emission of X-rays at resonance with electronic excitations. In RIXS process, two different scattering mechanisms take place: direct and indirect RIXS. The former is more dominant if allowed by selection rules, whereas the latter contributes only at higher orders [39].

A schematic representation of the direct scattering is reported in figure 2.2 (image taken from [39]). The impinging photon with wave vector \mathbf{k}_{in} carrying an energy $\hbar\omega_{in}$ excites a core level electron, promoting it into an empty state in the valence band. Within few fs, an electron from an occupied state in the valence band decays and fills the core hole, emitting a photon with wavevector \mathbf{k}_{out} and energy $\hbar\omega_{out}$. As a result of this 2-step excitation and relaxation

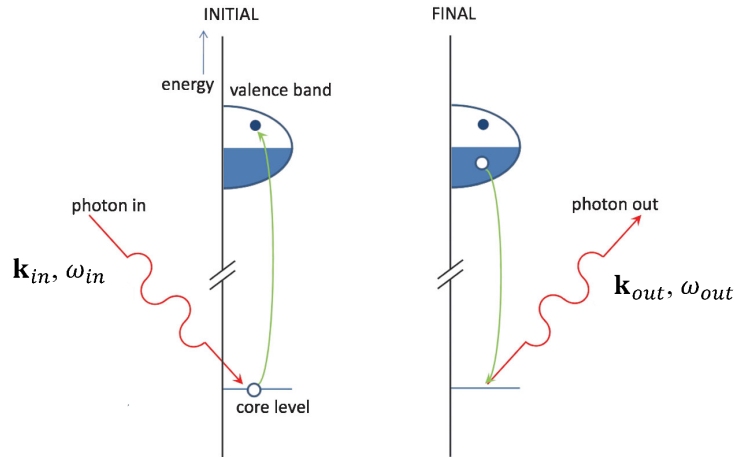


Figure 2.2: Schematic representation of the direct RIXS process. The impinging photon promotes the core electron into an empty state of the valence band. In few fs, an electron from the occupied valence band fills the core hole, emitting a new photon. As a consequence, a valence excitation has been created with momentum $\hbar\mathbf{k}_{out} - \hbar\mathbf{k}_{in}$, and energy $\hbar\omega_{in} - \hbar\omega_{out}$. Image taken from [39]

process, an electron-hole excitation is created, carrying a momentum $\hbar\mathbf{q} = \hbar\mathbf{k}_{out} - \hbar\mathbf{k}_{in}$ and energy $\hbar\omega = \hbar\omega_{out} - \hbar\omega_{in}$. For the direct RIXS to occur, both the excitation of the core hole and the following relaxation must be allowed by selection rules.

The indirect RIXS process is depicted in figure 2.3 (image taken from [39]). The electron core is excited into an empty state several eVs above the Fermi level. In the intermediate state, the core-hole potential scatters valence electrons which tend to screen the positive charge. As a consequence of that, electron-hole excitations are generated in the valence band. After the strongly excited electron decays in the core hole, the electron-hole excitations are left behind. However, it should be pointed out that for pure indirect RIXS to occur, transitions from core states to conduction band states must be weak.

At ESRF, the RIXS branch is composed of five major parts, as reported in fig. 2.4: a sample chamber, collimating mirror, spherical grating, polarimeter, detectors. The sample chamber hosts a four-circle UHV diffractometer and its position is fixed. From this, a mechanical arm composed of three vacuum chambers is attached. The first chamber contains a parabolic collimating mirror to increase the acceptance angle from the sample. The second chamber hosts two VLS spherical gratings that scatter the impinging photons in the vertical direction. The output signal would be a series of horizontal lines, each one associated with different energies. The last chamber at the end

2.2 Resonant Inelastic X-ray Scattering (RIXS)

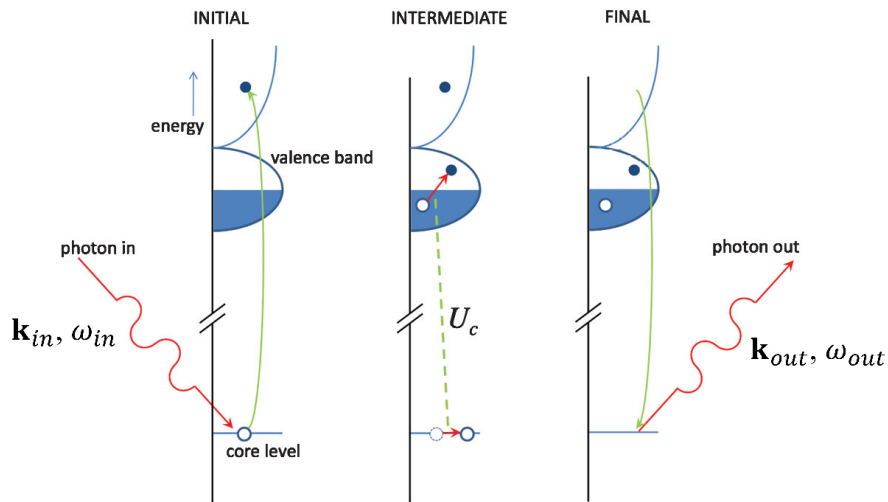


Figure 2.3: Schematic representation of the indirect RIXS. The impinging photon promotes one core electron to a strongly excited state, several eVs above the Fermi level. In this intermediate state, the core-hole potential scatters valence electrons, creating electron-hole excitations in the valence band. Once the strongly excited electron fills the core hole, those electron-hole excitations remain. Image taken from [39]

of the arm locates two 2D position-sensitive CCD cameras used as detectors. The output scattering angle can be changed from 50° to 150°

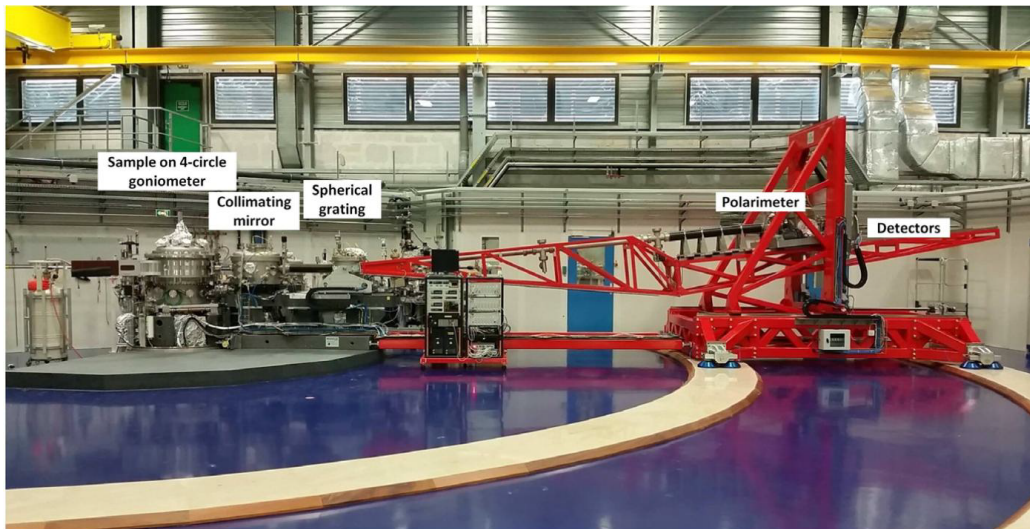


Figure 2.4: Structure at the end of RIXS branch. From left to right: four-circle diffractometer as sample holder, parabolic collimating mirror to increase acceptance angle, spherical gratings to scatter different energy signals in the vertical direction, detectors. Image takes from [38]

Chapter 3

Temperature dependent valence in Yb and Ce Kondo lattice from X-ray spectroscopies - a test case for MCR

All of the MCR-ALS analysis previously described have been implemented in a MATLAB script by [34]

3.1 Resonant X-ray emission on YbRh_2Si_2

YbRh_2Si_2 crystallizes in the ThCr_2Si_2 structure, whose crystallographic space group is $I4/mmm$, reported in figure 3.1. At low temperatures YbRh_2Si_2 exhibits a intermediate valence states due to the creation of Kondo lattices: the Yb^{+3} valence starts to slightly deviate towards Yb^{+2} .

In figure 3.2 the temperature evolution of $L3 - L\alpha 1$ RXES spectra of YbRh_2Si_2 are reported. By looking at the plot, a clear dependence of the peaks intensity over temperature emerges. The peak around 1527 eV decreases its intensity as the temperature rises; whereas the peak around 1533 eV exhibits the opposite behavior. From previous studies [40], is now clear the peaks around 1527 eV and 1533 eV are associated with Yb^{+2} and Yb^{+3} contributions, respectively.

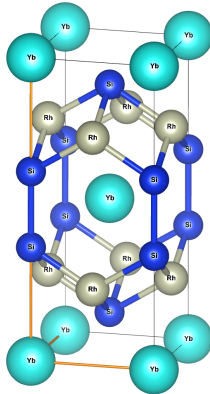
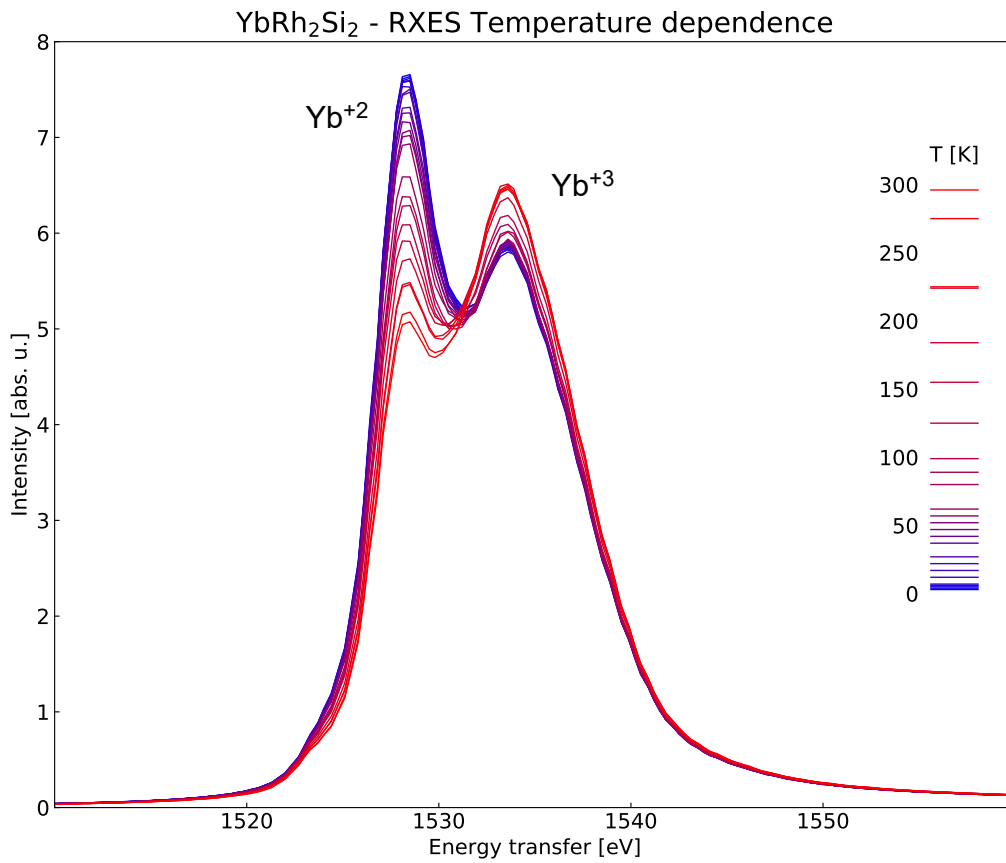
Figure 3.1: Crystal structure of YbRh_2Si_2 

Figure 3.2: Temperature evolution of RXES spectra of YbRh_2Si_2 . As referred in previous studies [40], the peaks around 1527 eV and 1533 eV are associated with Yb^{+2} and Yb^{+3} contributions respectively. A clear pattern emerges: as the temperature rises, the Yb^{+2} peak decreases more than the Yb^{+3} peak increases.

In order to extract the shape of the two peaks, the MCR-ALS method previously described was adopted. In figure 3.3, the singular values associated with the first seven principal components are shown. As described in chapter 1, the best number of principal components to select should be two, since, starting from the third component, the associated singular values are practically zero, especially if compared to the first which is 164.5.

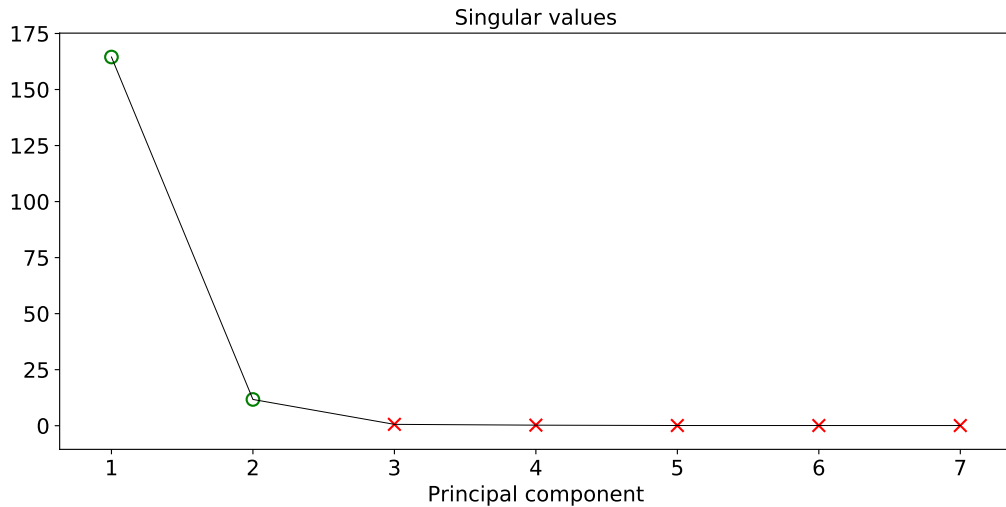


Figure 3.3: Singular value decomposition. Since after the 3rd component, the singular values are almost zero, only two components should be chosen. The values associated with the chosen component are marked with a green circle, while the values linked to discarded components are marked with a red cross.

Considering that a reasonable initial guess is required for the ALS algorithm, all the three methods depicted in chapter 1 will be used and tested. It should be pointed out that the only constrained used for both spectra and weight is the non-negativity constraint.

Firstly, the pure selection method is employed. In figure 3.4 two plot are reported: from left to right, the two principal components resulting from the optimization algorithm and the evolution of the weight of those two components as a function of temperature are reported. By just looking at the plot on the left, one can clearly see that each component recovers one of the two peaks of the RXES spectra. Thus, is reasonable to associate the 1st component (in red) with the Yb^{+2} peak, and the 2nd (in green) with the Yb^{+3} contribution. Moreover, looking at the second plot and recalling figure 3.2, the temperature evolution of the weights further supports and confirms the previous assumption. In fact, from figure 3.2, it is clear that the range over which the intensity of the Yb^{+2} varies is larger than the one of the

Yb^{+3} peak. Therefore, as the temperature increases, one should expect the weight associated with the 1st component (Yb^{+2}) to decrease more than the 2nd component weight (Yb^{+3}) increases. Indeed, the behavior just described matches the plot on the left in figure 3.4.

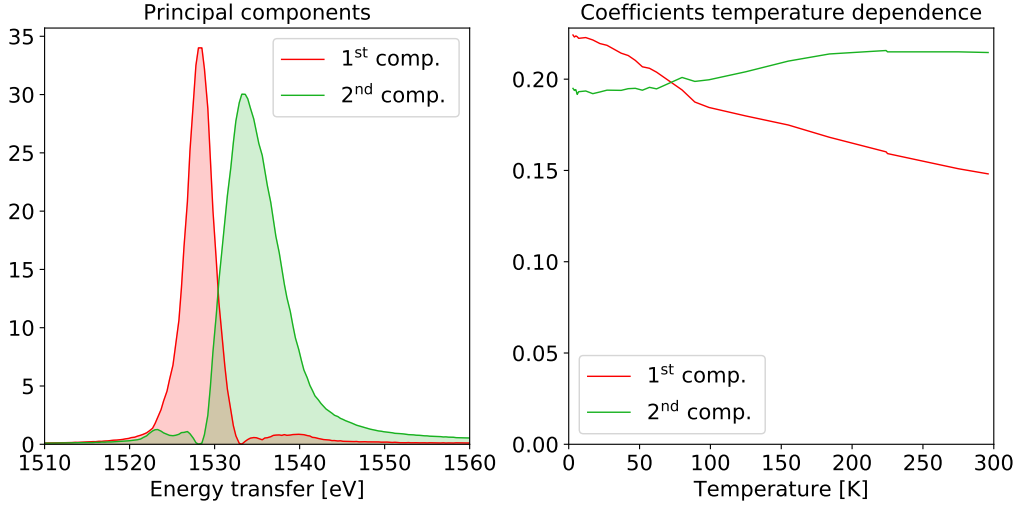


Figure 3.4: Principal components analysis with the pure variable detection method for initial guess selection. On the left, the two principal components are plotted; on the right, the temperature dependence of the weights are displayed. Each component describes only one peak of the spectra. From the temperature evolution of the components, it is clear the 1st and 2nd components are related to the Yb^{+2} and Yb^{+3} contributions respectively

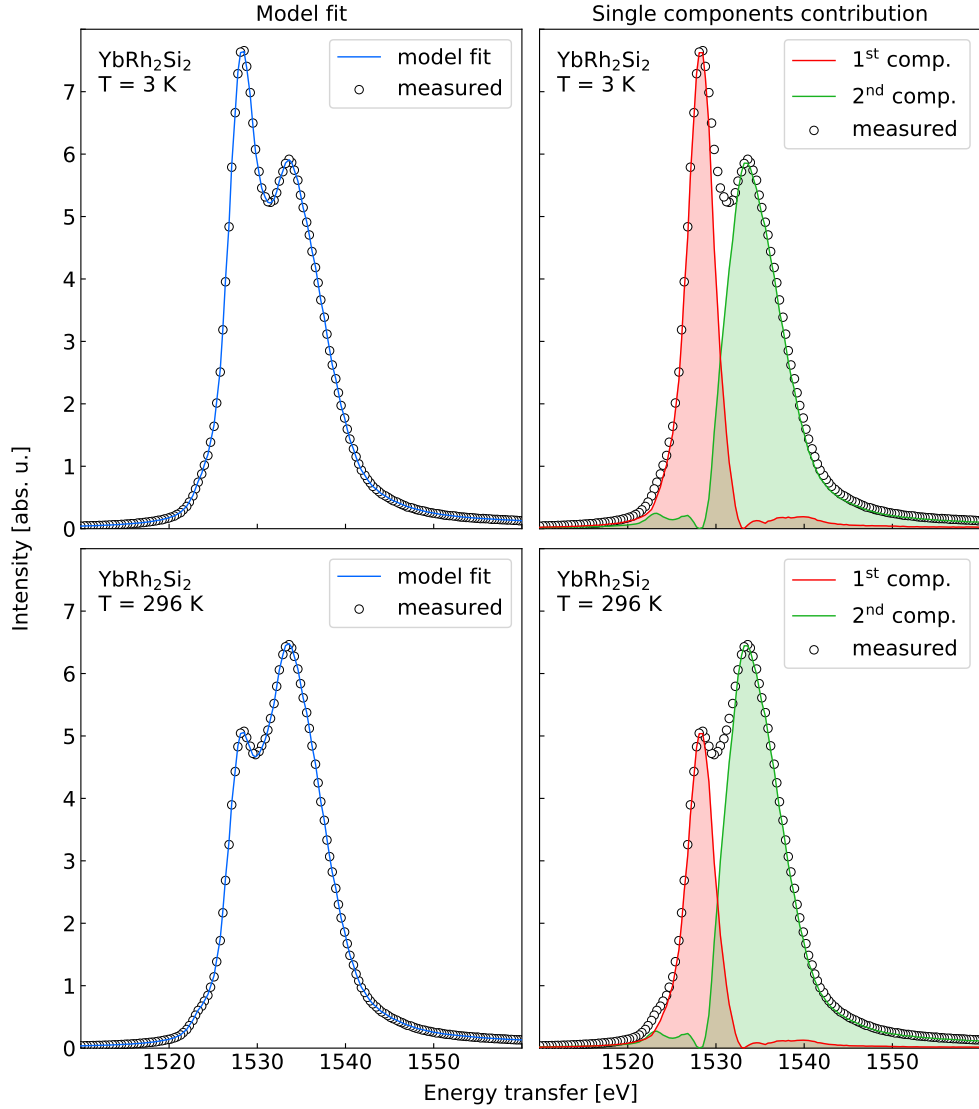


Figure 3.5: Model fit of the MCR-ALS analysis with pure variable detection method used for the initial guess selection. R2 factor is 99.9982% and the maximum of the residuals is of the order of 10^{-17} .

Let's now look at the contribution of each component to the total spectra and how well the model fits with experimental data. In figure 3.5 four plots are reported: in the second column the weighted contribution of the 1st and 2nd component are plotted separately, while in the first column they are summed. The two rows refer to the lowest (3 K) and highest (296 K) temperature measurements. These two extremes are taken into account to

enhance the difference between the Yb⁺² and Yb⁺² contributions.

The result of the PCA is quite astonishing: the first two principal components alone explain 99.9982% of the total variance, and the residuals are of the order of 10^{-17} .

Let's now look at the second choice of the initial guess. As a reasonable guess that does not include any a priori knowledge about the physics behind the shape of spectra, the mean (as 1st component) and the difference between the RXES spectra at 3 K and 296 K (as 2nd component) were chosen. In figure 3.6 the results from the MCR-ALS are reported in the same frame as the ones in figure 3.4. Notably, the 2nd component successfully recreates the Yb⁺² peak, while the first component matches the spectra at 296K, as one can clearly see from figure 3.7. The weights dependence over temperature displays a vanishing behavior for the 2nd component, having no contribution to the spectra at almost 300 K. This vanishing behavior is in accordance with the theory which claims that the valence of Yb ions at 300 K should be really close to +3.

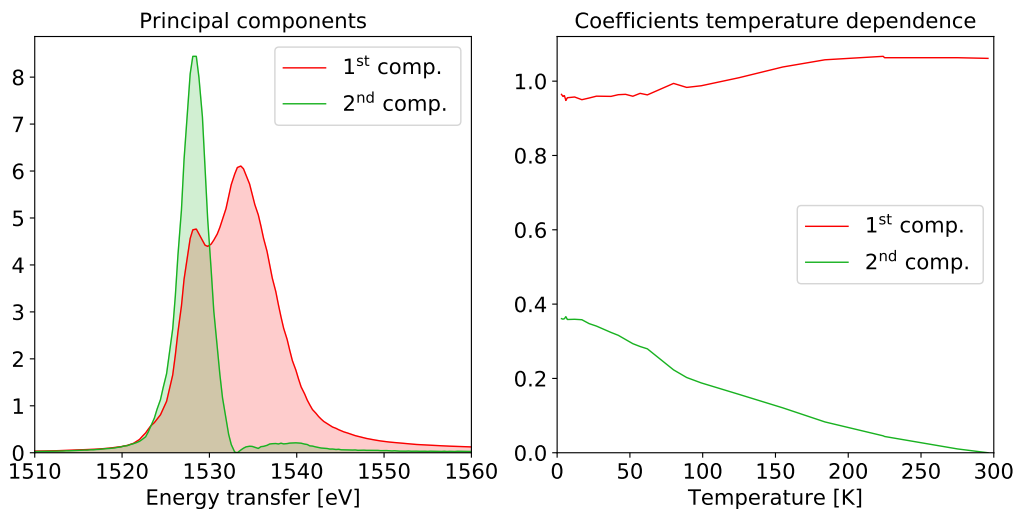


Figure 3.6: Principal components analysis where the initial guesses were the mean of the spectra and the difference between the 3 K and 296 K measurements. On the left, the two principal components are plotted; on the right, the temperature dependence of the weights are displayed. The 2nd component clearly reconstructs the peak associated with Yb⁺², while the 1st component resembles the 296 K spectrum. Notably, the 2nd component contribution to the total spectrum vanishes at 296 K, in accordance with the Yb +3 valence at 300 K reported in previous studies.

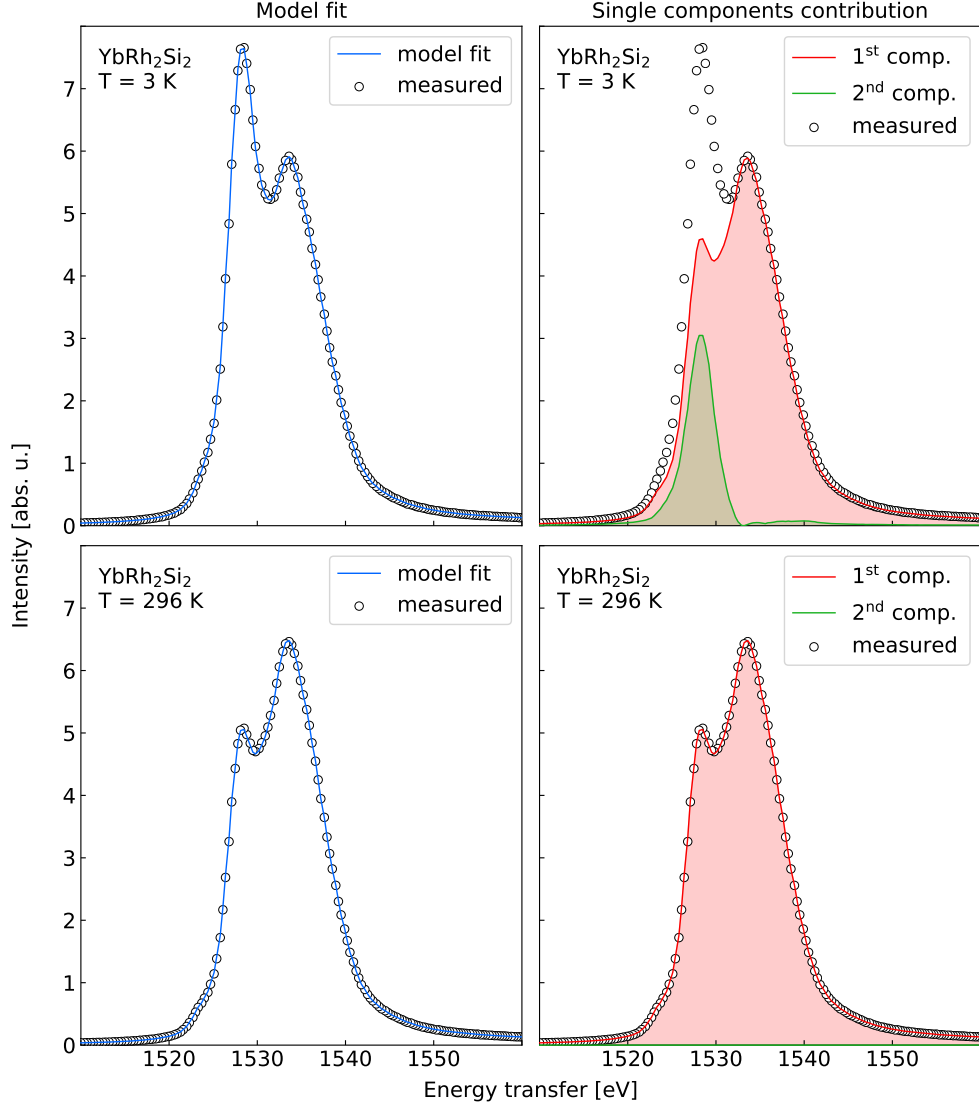


Figure 3.7: Model fit of the MCR-ALS analysis where the initial guesses were the mean of the spectra and the difference between the 3 K and 296 K measurements. R² factor is 99.9982% and the maximum of the residuals is of the order of 10^{-7} .

Finally, let's analyze the EFA as a method to choose initial guesses. As aforementioned in chapter 1, the EFA should be used whenever one expects there is a sequential order of emergence/decay for all components in the system. As already highlighted above, there is a sequential decay and emergence of the Yb^{+2} and Yb^{+3} contribution. However, it should be pointed out that the EFA is thought to work well whenever the emergence/decay is complete

in the sense that one component fully substitutes the others as the spectra evolves. This is not clearly the case, since at 3 K there is still a significant Yb^{+3} contribution to the total spectra intensity. Nevertheless, it is worth giving a try. The resulting MCR-ALS analysis is reported in figure 3.8.

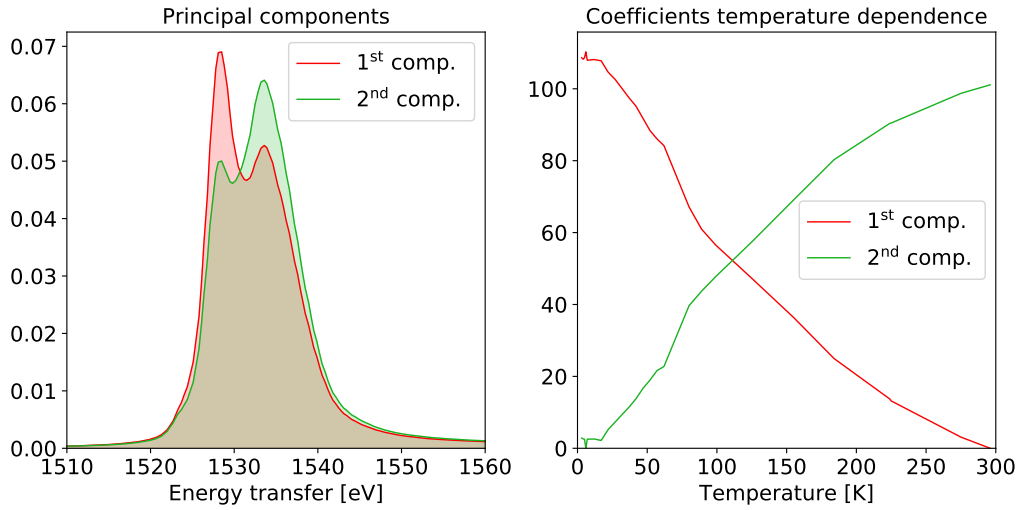


Figure 3.8: Principal component analysis with the EFA as method used for the initial guess selection. Despite the presence of the emergence and decay behavior of the spectra, the resulting components do not reflect the physics of the phenomenon, since the Yb^{+3} contribution always be present.

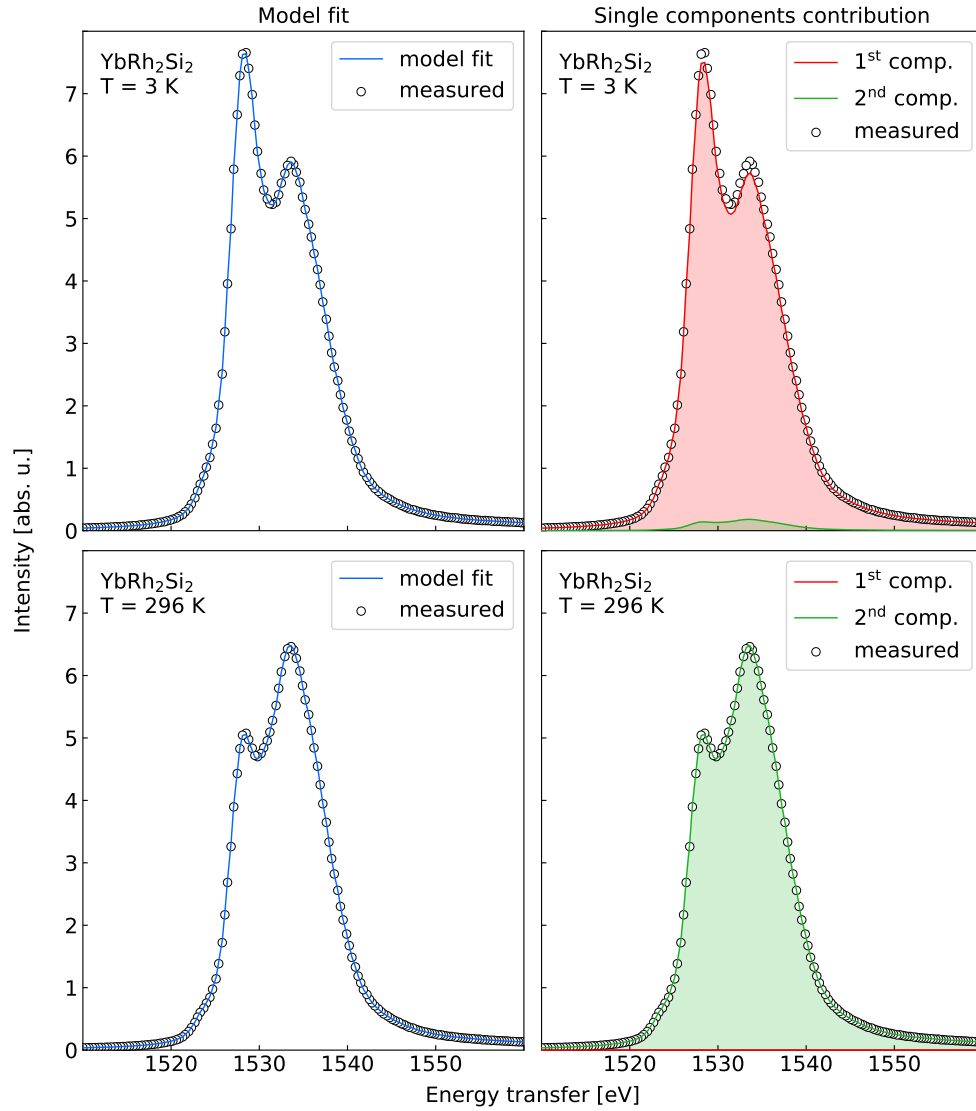


Figure 3.9: Model fit of the MCR-ALS analysis with evolving factor analysis for the initial guess selection. R2 factor is 99.9982% and the maximum of the residuals is of the order of 10^{-6} .

The two peaks are not isolated into one component each, instead both principal components contain the two peaks. Moreover, looking at the evolution of the weights, is clear how the EFA searches for complete emergence and decay of the components: indeed, at the extreme of the temperature range only one component is present. The model fit reported in figure 3.9 further confirm what said just above: the 1st component is exactly the RXES

spectra at 3 K, while the 2nd is the RXES spectra at 296 K.

One thing is worth pointing out at this point. The three analyses described above only differ in the selection of the initial guess, and those selections lead to three very different outcomes in terms of the shape of the principal components.

| | Pure | Mean&Diff | EFA |
|-----------|------------|-----------|-----------|
| R2 | 99.9982% | 99.9982% | 99.9982% |
| Residuals | 10^{-17} | 10^{-7} | 10^{-6} |

Table 3.1: R2 factors and max order of magnitude of residuals of MCR-ALS analysis on YbRh₂Si₂

In the table 3.1 the R2 and residuals of the three MCR-ALS analyses just described are reported. All three of them have a 99.9982% the percentage of total variance explained and very low residuals. This is a clear example of the rotational ambiguity introduced in chapter 1. At this point some kind of physical knowledge about the phenomenon needs to be introduced to interpret the results and decide which method is the one to choose. Indeed, only the pure variable selection method led to physically meaningful results.

3.2 Soft X-ray absorption spectroscopy on Ce 122 systems

Ternary intermetallic systems based on Ce exhibit interesting intermediate valence behaviors around the Kondo scale. In this section, Soft XAS of different Ce compounds are analyzed through MCR-ALS and more classical spectra analysis.

The ternary intermetallic system in study are the following:

In table 3.3, crystalline structure of CeNi₂Si₂, CeNi₂Ge₂, CeRu₂Si₂ and CeRu₂Ge₂ along with their lattice constants are reported. They all exhibit a ThCr₂Si₂-type crystalline structure.

In order to evaluate the intermediate valence M_{4,5} edge X-ray absorption spectra were acquired. An example of how those spectra look like is reported in figure 3.10. From previous studies [45] have emerged that the small peaks around 885 eV and 903 eV are the Ce⁺⁴ (4f⁰ configuration) contribution to the M₄ and M₅ edges respectively. All the other peaks are related to the M₄ and M₅ edges of Ce⁺³ (4f¹ configuration).

| | |
|--------------------------|--------------------------|
| $CeNi_2Si_2$ | $CeRu_2Si_2$ |
| $CeNi_2Si_{1.2}Ge_{0.8}$ | $CeRu_2Si_{1.7}Ge_{0.3}$ |
| $CeNi_2Si_{0.6}Ge_{1.4}$ | $CeRu_2Si_{1.2}Ge_{0.8}$ |
| $CeNi_2Si_{0.2}Ge_{1.8}$ | $CeRu_2Si_{0.6}Ge_{1.4}$ |
| $CeNi_2Ge_2$ | $CeRu_2Ge_2$ |

Table 3.2: Ternary compounds based on Ce analyzed

In order to understand how the valence changes over the temperature range, the intensity of the $4f^0$ peaks must be extract from the spectra. To separate the contribution of the $4f^0$ shell with respect to the $4f^1$, two different methods have been used: MCR-ALS and SNIP algorithm. However, before the actual peak reconstruction, data must be prepared. First of all, all spectra are normalized over the intensity of the impinging beam in order to take into account fluctuations of the beam intensity over time and energy. Then, the background is removed by subtracting a 2-step arctan function conveniently weighted:

$$f(c_1, c_2, \varepsilon_1, \varepsilon_2, \gamma_1, \gamma_2) = \frac{1}{\pi} \left[c_1 \arctan\left(\frac{\varepsilon - \varepsilon_1}{\gamma_1} + \frac{\pi}{2}\right) + c_2 \arctan\left(\frac{\varepsilon - \varepsilon_2}{\gamma_2} + \frac{\pi}{2}\right) \right], \quad (3.1)$$

where c_1 and c_2 are the intensities of the two plautes after each peak respectively, γ_1 and γ_2 measure how broadened is the arctan function in energy. The two arctan functions are centered at the maximum of the two edges.

Each measurement has a slightly different energy scale. In order to align spectra from different measurements, the points must be increased through interpolation and then smoothed out. At this point spectra are ready for peak isolation.

The first Ce ternary compound studied is $CeNi_2Si_2$. It crystallizes in the $ThCr_2Si_2$ structure, whose crystallographic space group is $I4/mmm$.

In figure 3.10 the temperature evolution of Soft XAS spectra at the $M_{4,5}$ edge of $CeNi_2Si_2$ is reported. As said before, the Ce^{+4} contribution to the spectra are four peaks at almost 884 eV, 886 eV, 902 eV and 904 eV. Notably, the different features of the spectrum slightly change with temperature.

In figure 3.11 singular values from the singular value decomposition are plotted. The predominance of one singular value is evident, suggesting that the PCA might not work. However, a similar condition was found for

3.2 Soft X-ray absorption spectroscopy on Ce 122 systems

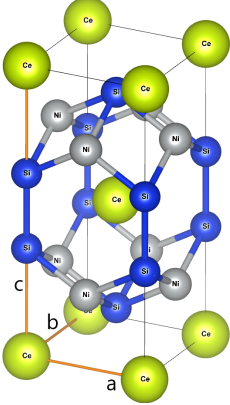
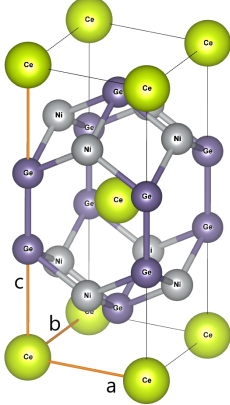
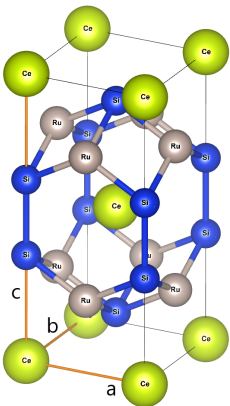
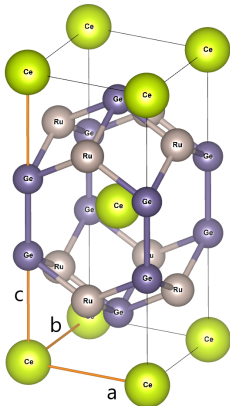
| | | |
|-----------|---|--|
| Compound | CeNi ₂ Si ₂ | CeNi ₂ Ge ₂ |
| Structure |  |  |
| a [Å] | 4.0325 | 4.1500 |
| b [Å] | 4.0325 | 4.1500 |
| c [Å] | 9.5663 | 9.8540 |
| Compound | CeRu ₂ Si ₂ | CeRu ₂ Ge ₂ |
| Structure |  |  |
| a [Å] | 4.1850 | 4.2684 |
| b [Å] | 4.1850 | 4.2684 |
| c [Å] | 9.7940 | 10.0471 |

Table 3.3: Crystalline structure of four different ternary intermetallic compounds based on Ce. lattice parameters taken from [41, 42, 43, 44] for CeNi₂Si₂, CeNi₂Ge₂, CeRu₂Si₂ and CeRu₂Ge₂ respectively

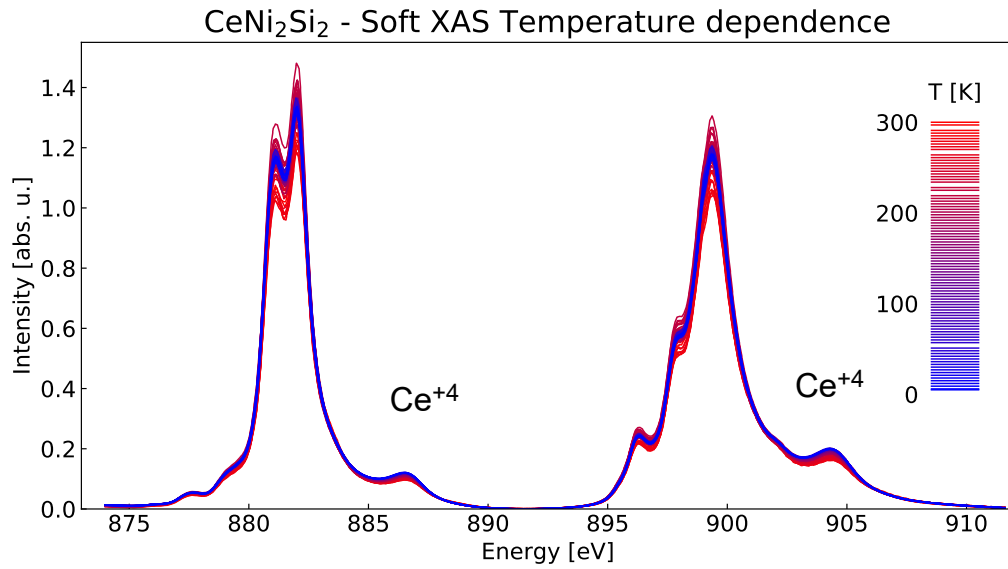


Figure 3.10: Temperature evolution of $M_{4,5}$ Soft XAS of $CeNi_2Si_2$. The contribution of Ce^{+4} are four peaks around 884 eV, 886 eV 902 eV and 904 eV; all the other peaks coming from the XAS of Ce^{+3} .

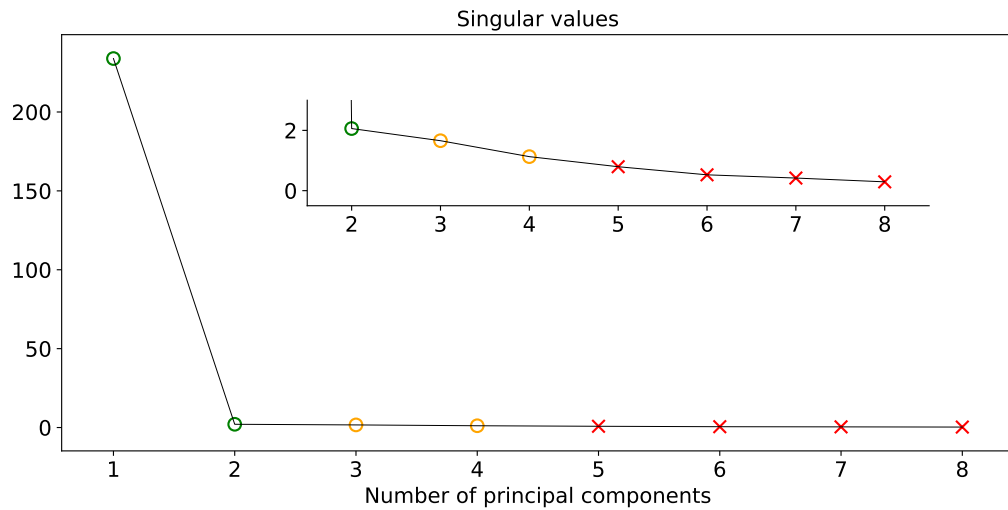


Figure 3.11: Singular value decomposition. Two is the minimum number of PCs that is possible to select. The second choice of the number of PCs is four since the 3rd and 4th components have singular values close to the one related to the 2nd

YbRh_2Si_2 case, and it still led to good results; therefore, it is worth it giving a try. Since PCs components from the 2nd to the 4th have similar singular values, two PCAs will be carried with two and four PCs, respectively. As for the previous case all the three methods for the initial guess selection were employed. Let's start from the pure variable selection method. In figures 3.12 and 3.13 the PCA analysis with two and four PCs are reported.

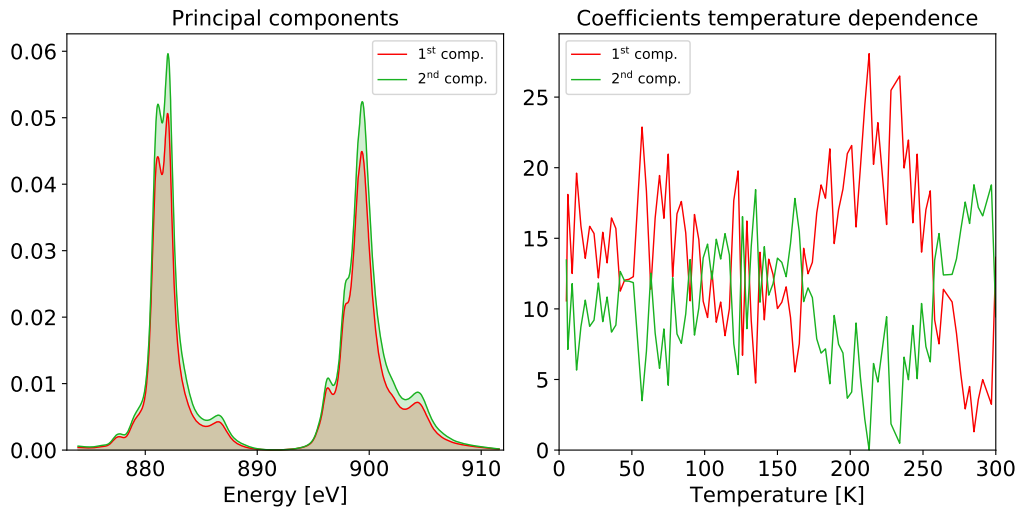


Figure 3.12: PCA on CeNi_2Si_2 with two PCs when pure variable selection is used as method to generate a suitable initial guess.

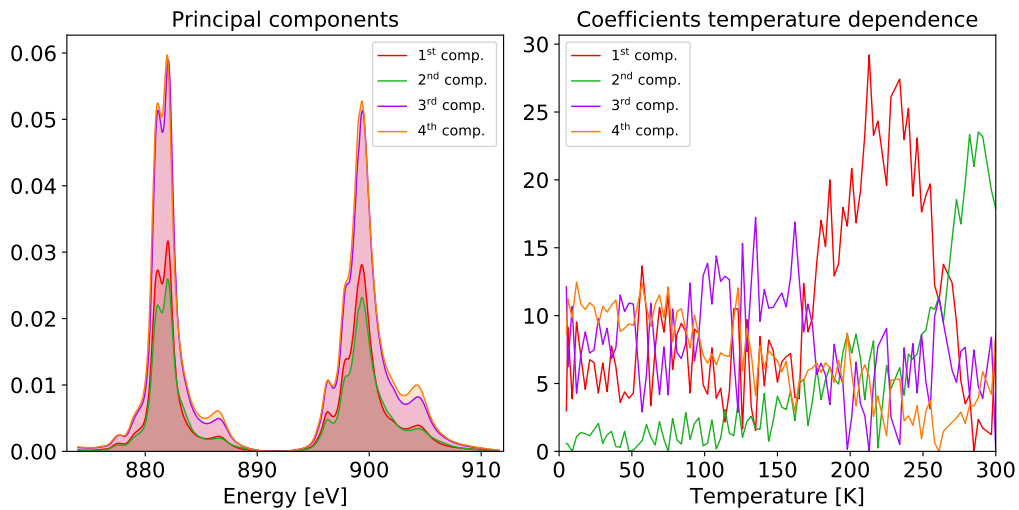


Figure 3.13: PCA on CeNi_2Si_2 with four PCs when pure variable selection is used as method to generate a suitable initial guess.

Notably, the situation is far more chaotic with respect to the YbRh_2Si_2 case. There is no clear difference between PCs in both studies reported in figures 3.12 and 3.13: different components do not describe different peaks or groups of peaks. The same regarding the temperature evolution of weights: no clear dependence emerges.

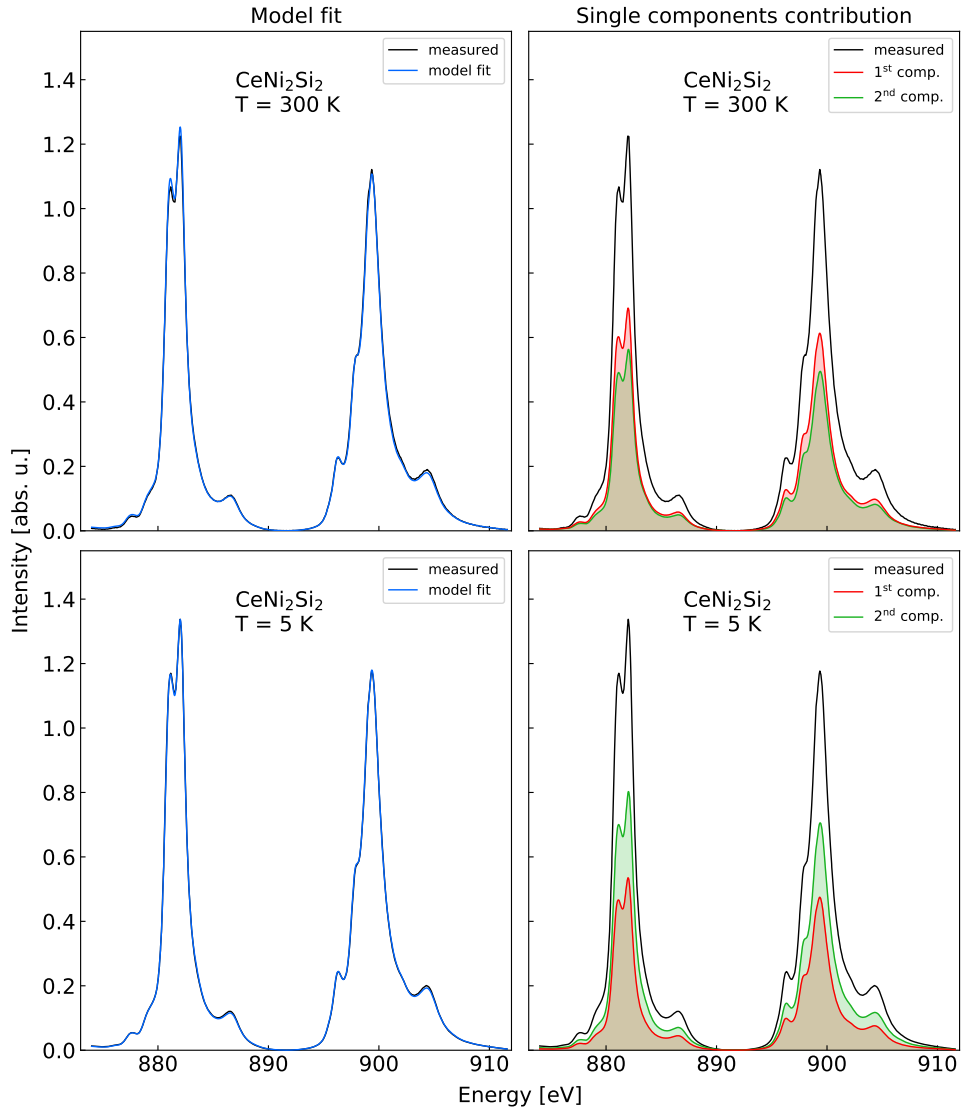


Figure 3.14: Model fit of the MCR-ALS analysis on CeNi_2Si_2 with two PCs when the pure variable selection method is used for the initial guess selection. R2 factor is 99.996% and the maximum of the residuals is of the order of 10^{-6} .

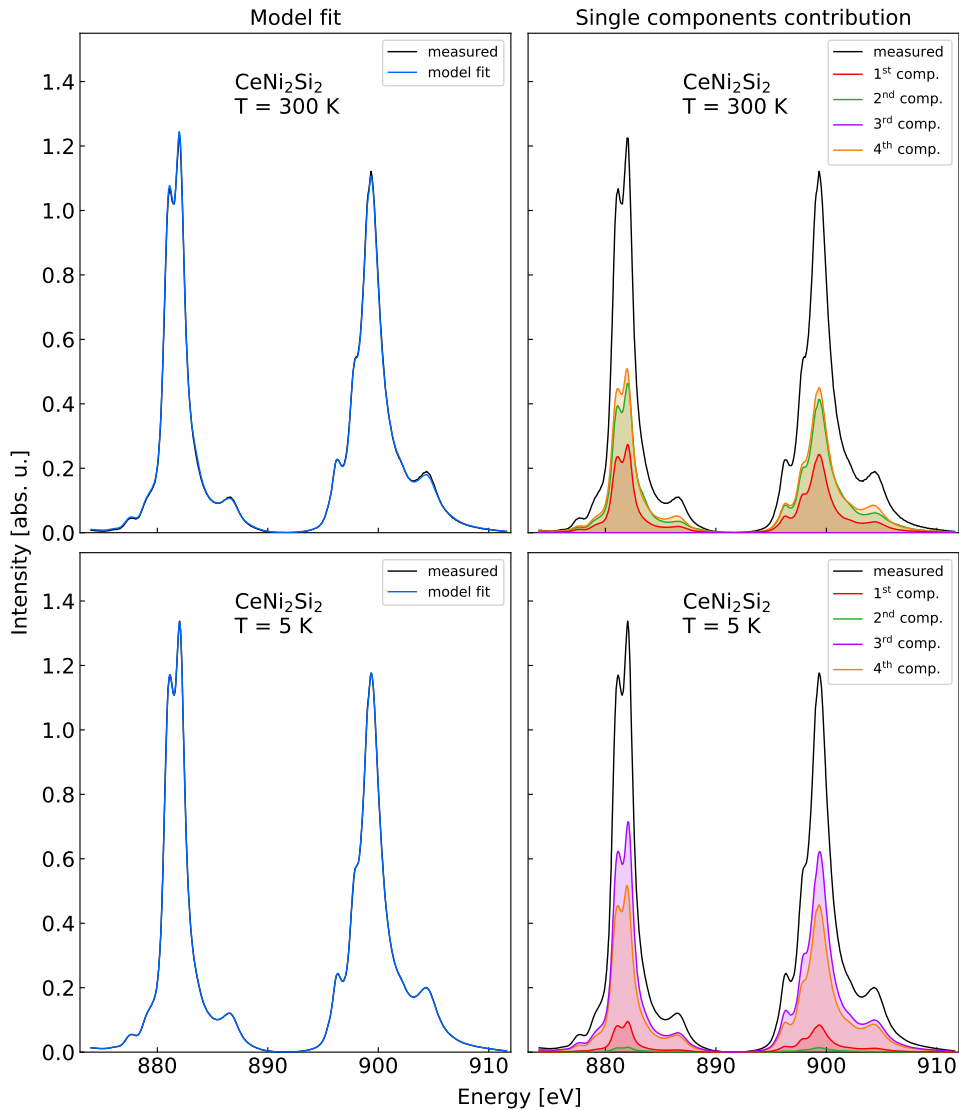


Figure 3.15: Model fit of the MCR-ALS analysis on CeNi_2Si_2 with four PCs when the pure variable selection method is used for the initial guess selection. R2 factor is 99.9989% and the maximum of the residuals is of the order of 10^{-6} .

In figures 3.14 and 3.15 the model fit with two and four PCs are reported. Despite having a really good fit, the PCs have no physical significance. All in all this method has resulted in being inconclusive.

Let's focus the second selection of initial guess: as for the YbRh_2Si_2 case, the mean of all spectra, and the difference between the measurements at 5 and 300 K are chosen as initial guesses.

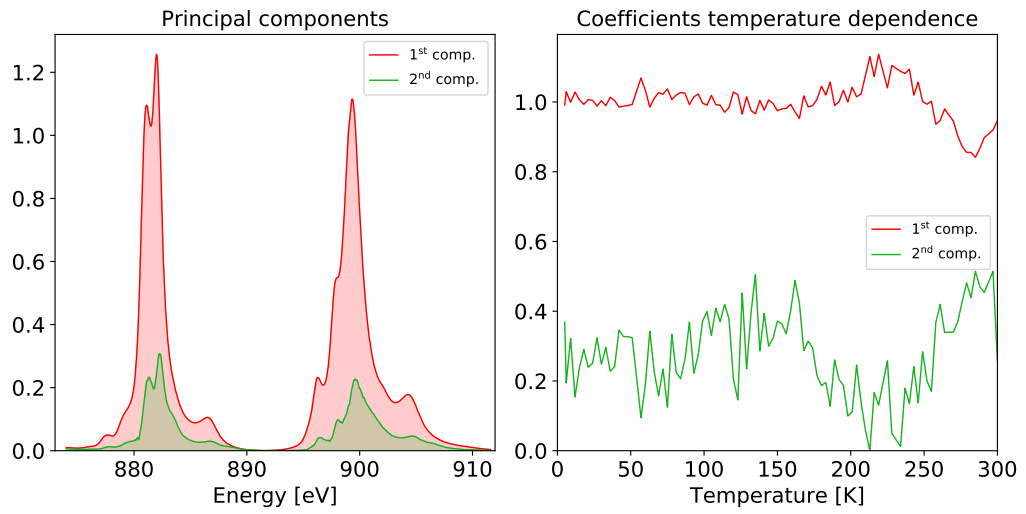


Figure 3.16: PCA on CeNi_2Si_2 with two PCs when the mean of spectra and the difference between the spectra at 5 K and 300 K are used as the initial guesses.

Compared to the previous method, now the evolution of the weights seems more clear. However, the shape of the two PCs resembles the entire shape of spectra; again, the PCA is not able to separate different features of the spectra without any a priori knowledge.

3.2 Soft X-ray absorption spectroscopy on Ce 122 systems

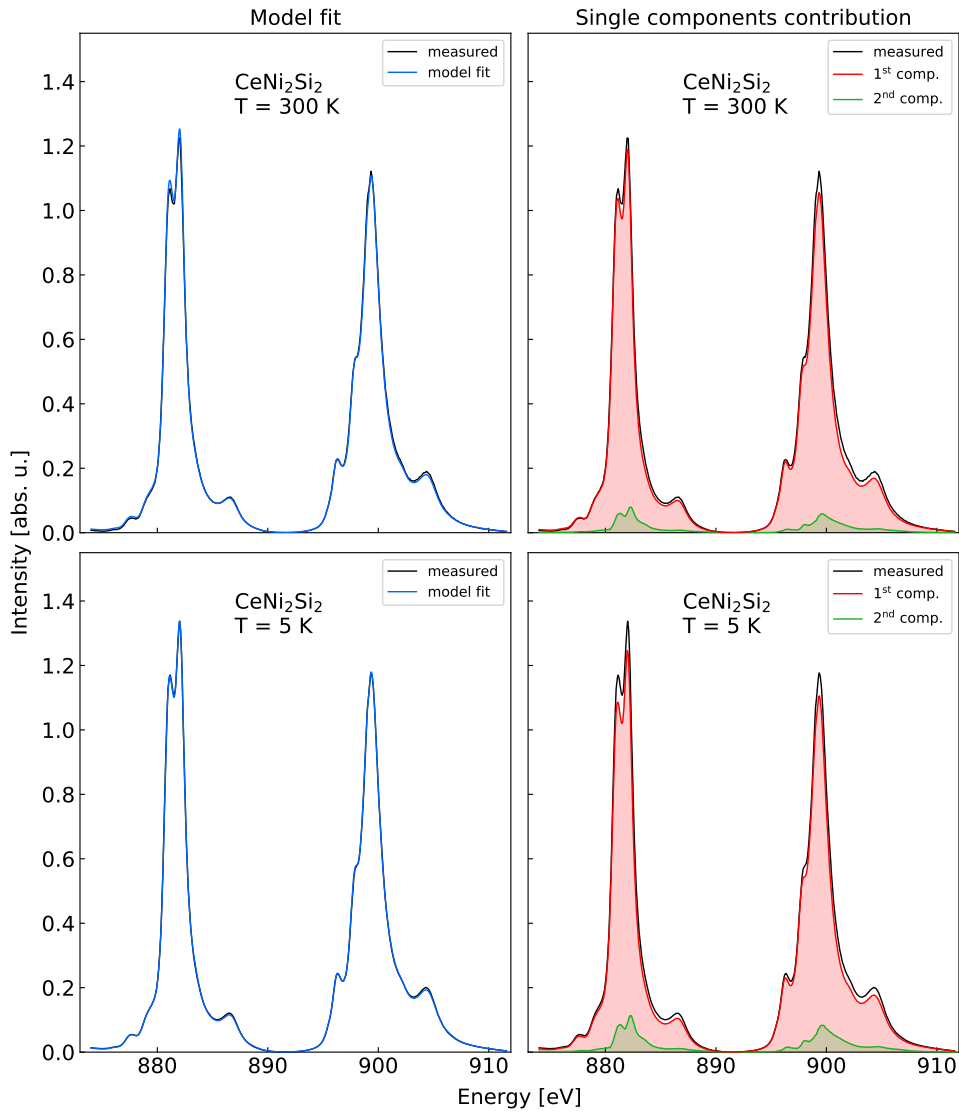


Figure 3.17: Model fit of the MCR-ALS analysis on CeNi_2Si_2 with two PCs when the mean of spectra and the difference between the spectra at 5 K and 300 K are used as the initial guesses. R2 factor is 99.9964% and the maximum of the residuals is of the order of 10^{-6} .

By looking at figure 3.17, the model fit is again good, with a R2 factor of 99.9964% and residuals of the order of 10^{-6} .

Finally let's look at the EFA as selection method for the initial guess. The resulting PCA with two and four components is shown in figures 3.18 and 3.19. Again the situation has not changed: there is no physical meaning

behind the PCs.

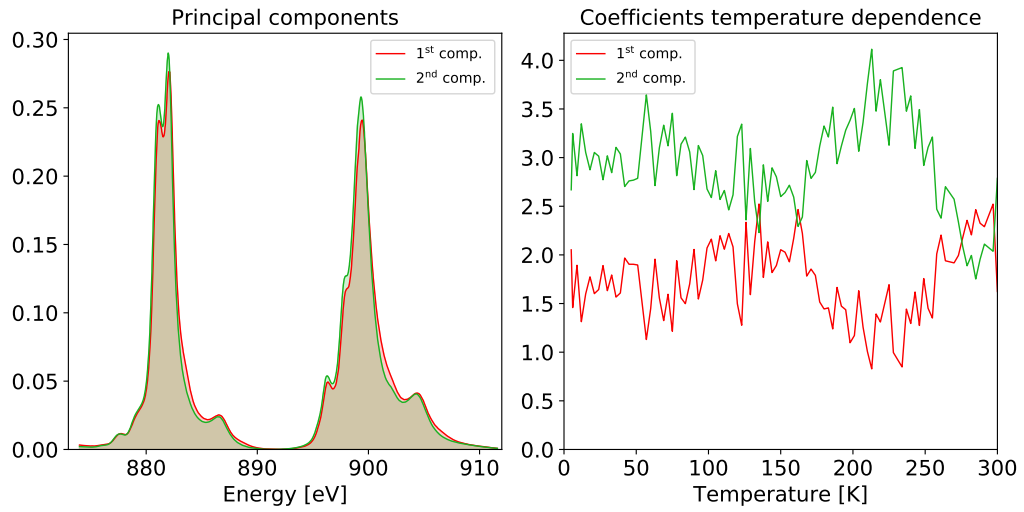


Figure 3.18: PCA on CeNi_2Si_2 with two PCs when EFA is employed as method to generate a suitable initial guess.

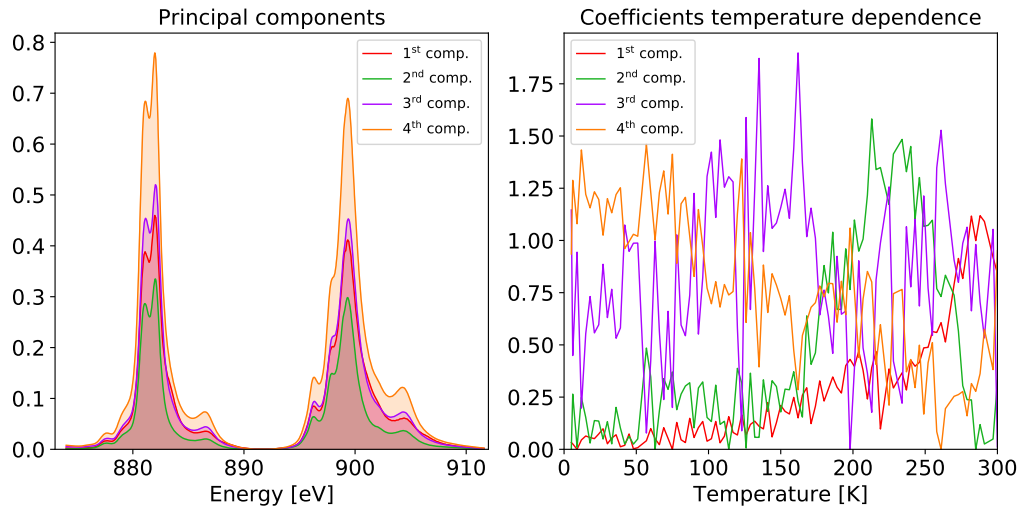


Figure 3.19: PCA on CeNi_2Si_2 with four PCs when EFA is employed as method to generate a suitable initial guess.

3.2 Soft X-ray absorption spectroscopy on Ce 122 systems

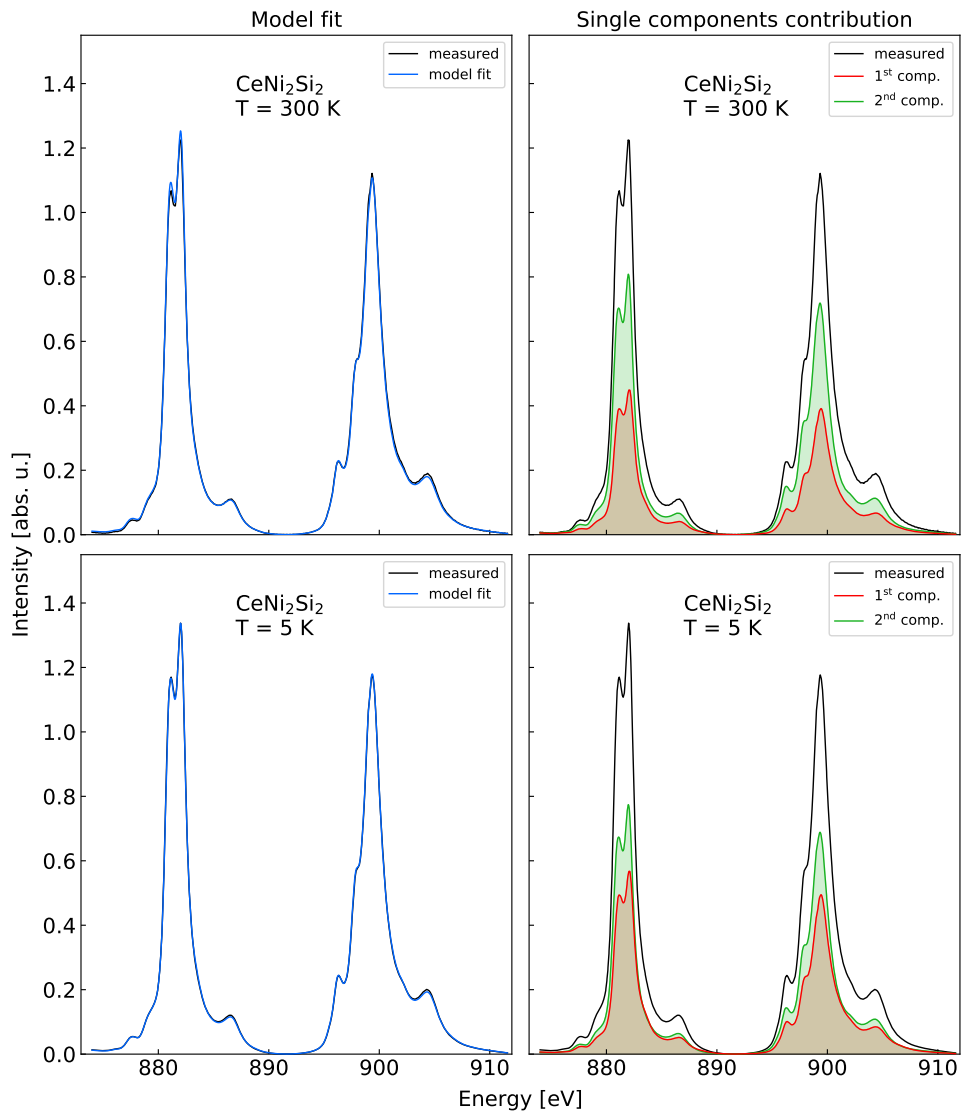


Figure 3.20: Model fit of the MCR-ALS analysis on CeNi_2Si_2 with two PCs in which the EFA was used to select the initial guess. R2 factor is 99.996% and the maximum of the residuals is of the order of 10^{-6} .

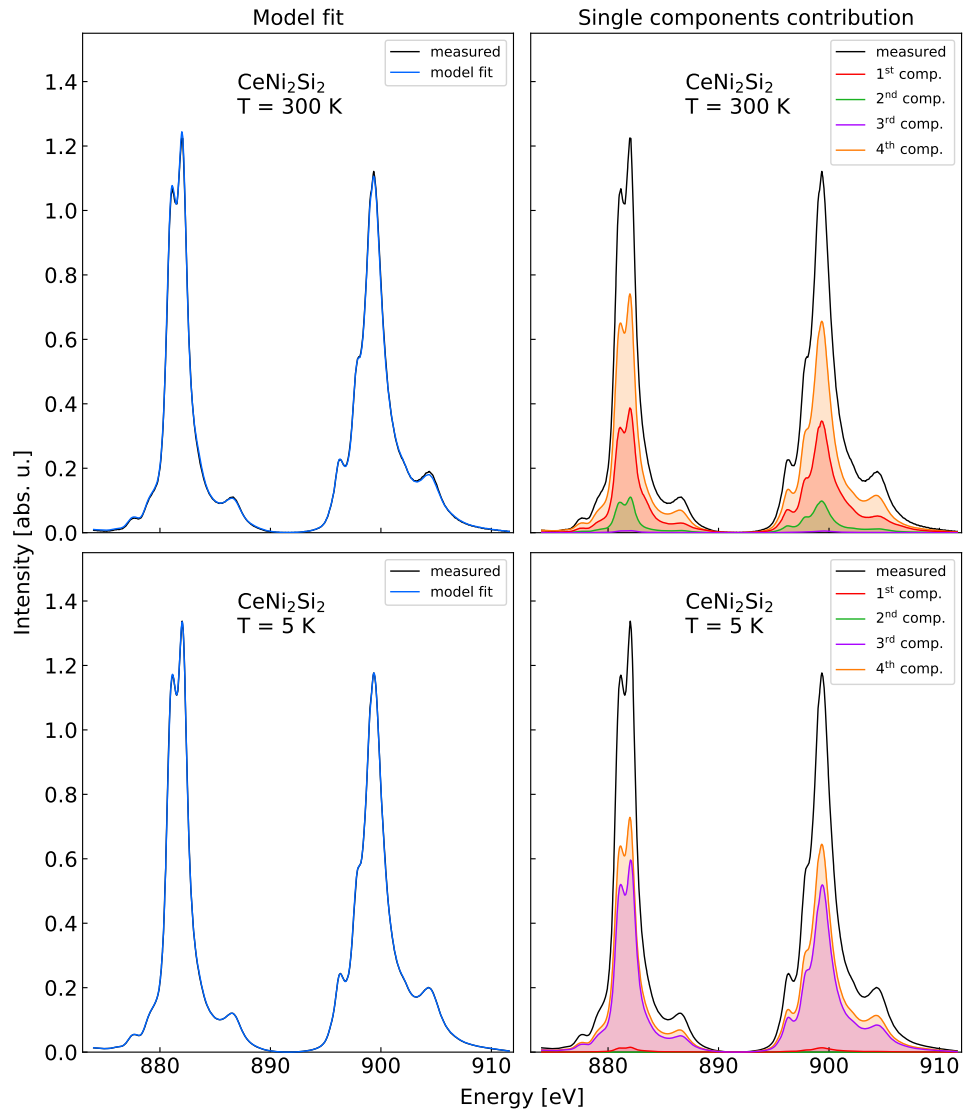


Figure 3.21: Model fit of the MCR-ALS analysis on CeNi_2Si_2 with four PCs in which the EFA was used to select the initial guess. R2 factor is 99.9989% and the maximum of the residuals is of the order of 10^{-6} .

The model fits reported in figures 3.203.21 show again good results: the R2 factor is 99.996% for the analysis with two PCs, while the one with four PCs has a R2 factor of 99.9989%. Residuals are both of the order of 10^{-6} . In the end, all three methods have lead to similar results with no physical meaning but good fits.

3.2 Soft X-ray absorption spectroscopy on Ce 122 systems

| | 2 PCs Pure | 4 PCs Pure | 2 PCs Mean&Diff | 2 PCs EFA | 4 PCs EFA |
|-----------|------------|------------|-----------------|-----------|-----------|
| R2 | 99.996% | 99.9989% | 99.9964% | 99.996% | 99.9989% |
| Residuals | 10^{-5} | 10^{-6} | 10^{-6} | 10^{-6} | 10^{-6} |

Table 3.4: R2 factors and max order of magnitude of residuals of MCR-ALS analysis on CeNi_2Si_2

The second compound analyzed is CeRu_2Ge_2 , which crystallizes in the same ThCr_2Si_2 structure as CeNi_2Si_2 .

In figure 3.22 Soft XAS spectra of CeRu_2Ge_2 are plotted. As for the CeNi_2Si_2 , intensities of different peak slightly change with temperature.

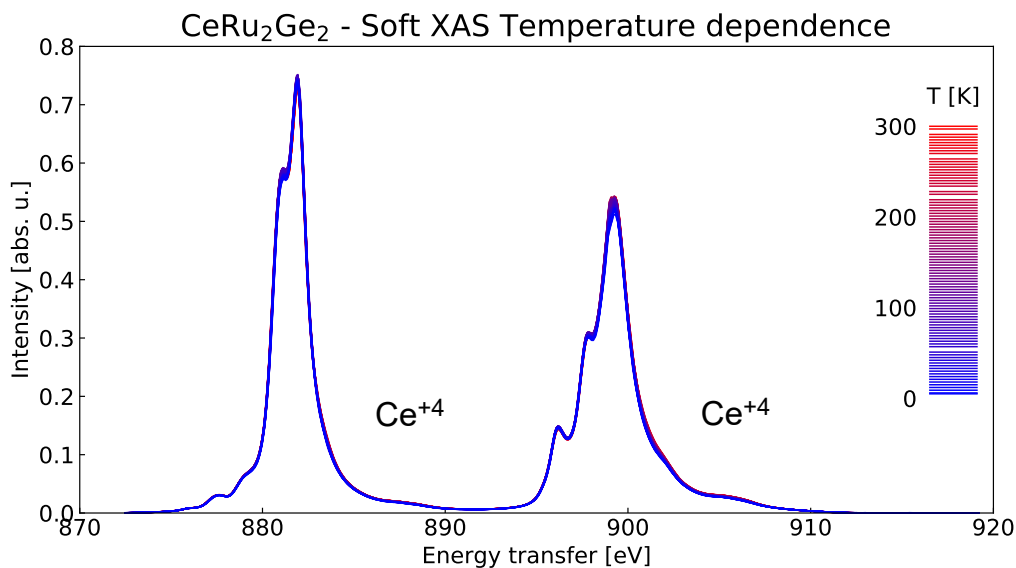


Figure 3.22: Temperature evolution of $M_{4,5}$ Soft XAS of CeRu_2Ge_2 . The contribution of Ce^{+4} are four peaks around 884 eV, 886 eV, 902 eV and 904 eV; all the other peaks coming from the XAS of Ce^{+3} .

Being the spectra similar between the two Ce compounds presented, almost equal singular values were obtained as one can see in figure 3.23. However, in this case only the 3rd singular value is close to the 2nd; therefore a maximum of three PCs is considered.

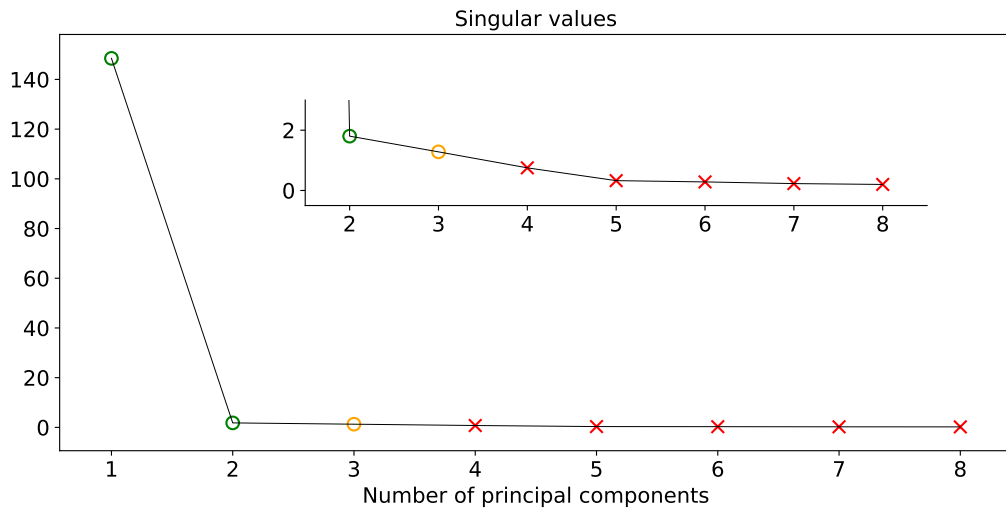


Figure 3.23: Singular value decomposition. Two is the minimum number of PCs that is possible to select. The second choice of the number of PCs is three since only the 3rd component has singular value close to the one related to the 2nd

Since all the MCSALS methods employed have reported similar results, they are all commented at the end. In order there will be: PCA when pure variable selection method is employed in figures 3.24 and 3.25, and the corresponding models fits in figures 3.26 and 3.27; subsequently in figures 3.28 and 3.29, PCA and model fit when the mean and difference were chosen as initial guesses is reported; finally in figures 3.30 and 3.31 PCAs in which the EFA method is used are shown, and in figures 3.32 and 3.33 the corresponding model fits are plotted.

3.2 Soft X-ray absorption spectroscopy on Ce 122 systems

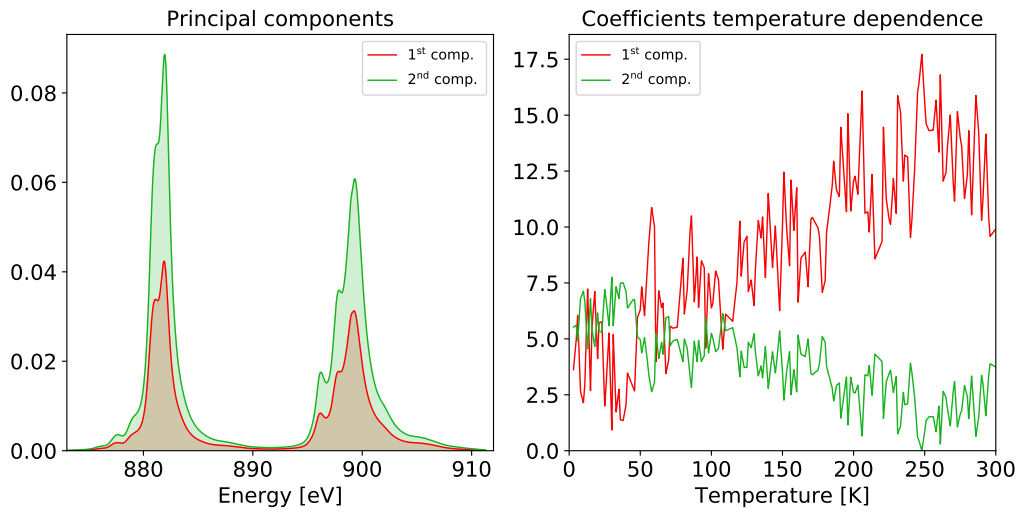


Figure 3.24: PCA on CeRu_2Ge_2 with two PCs when pure variable selection is used as method to generate a suitable initial guess.

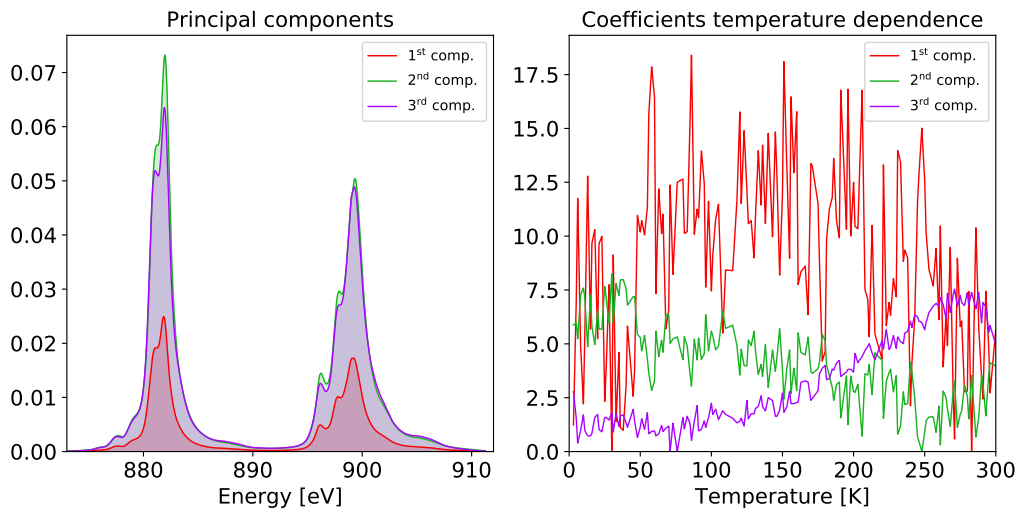


Figure 3.25: PCA on CeRu_2Ge_2 with three PCs when pure variable selection is used as method to generate a suitable initial guess.

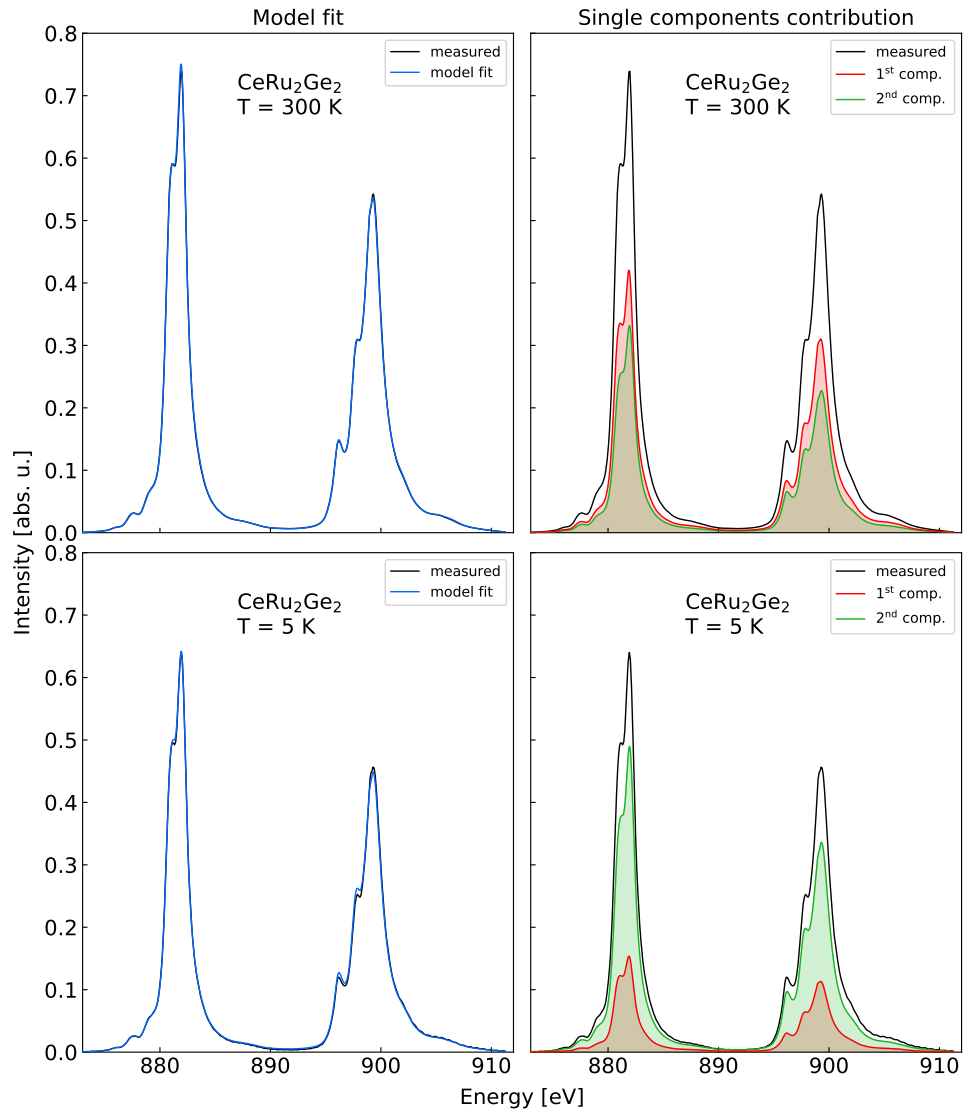


Figure 3.26: Model fit of the MCR-ALS analysis on CeRu_2Ge_2 with two PCs when pure variable selection is used as method to generate a suitable initial guess. R2 factor is 99.9944% and the maximum of the residuals is of the order of 10^{-5} .

3.2 Soft X-ray absorption spectroscopy on Ce 122 systems

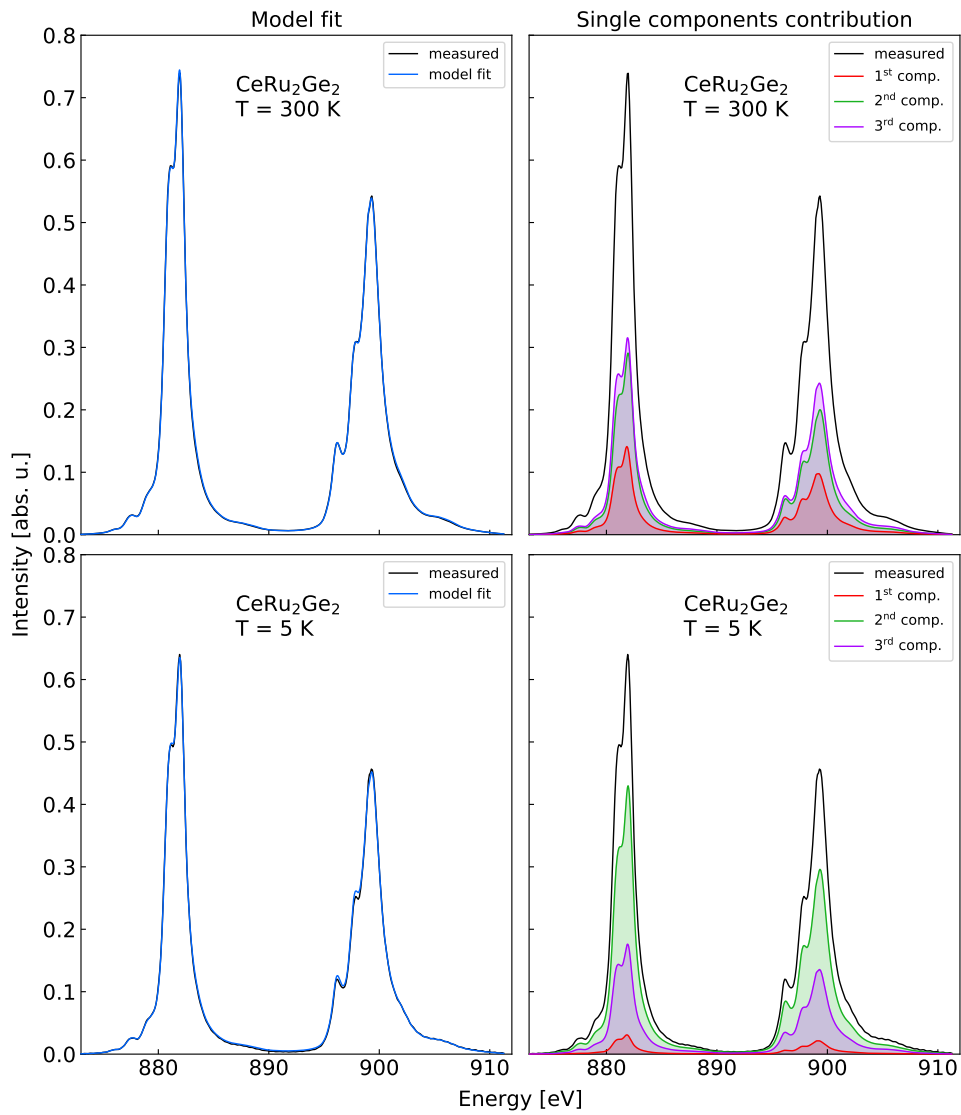


Figure 3.27: Model fit of the MCR-ALS analysis on CeRu_2Ge_2 with two PCs when pure variable selection is used as method to generate a suitable initial guess. R2 factor is 99.9978% and the maximum of the residuals is of the order of 10^{-5} .

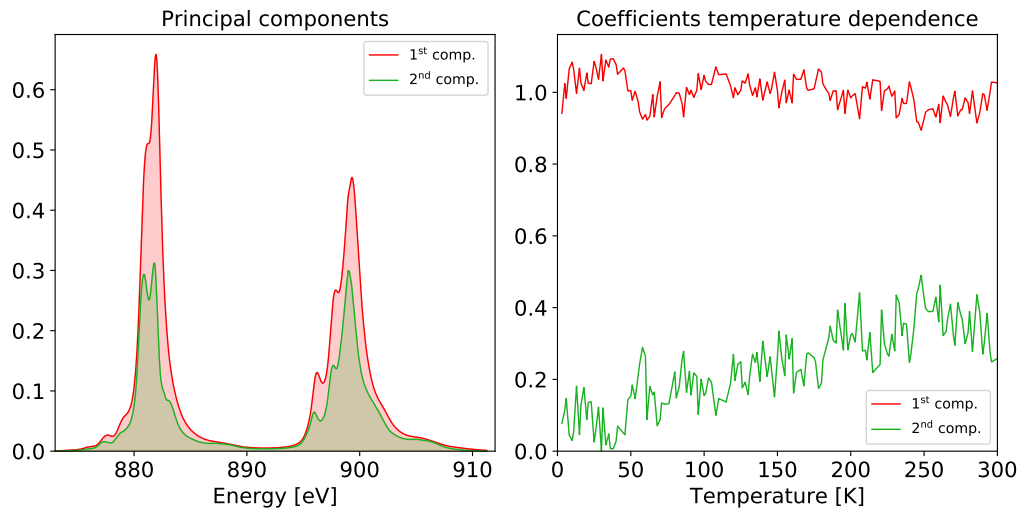


Figure 3.28: PCA on CeRu_2Ge_2 with two PCs when the mean of spectra and the difference between measurements at 5 and 300 K were used as suitable initial guesses.

3.2 Soft X-ray absorption spectroscopy on Ce 122 systems

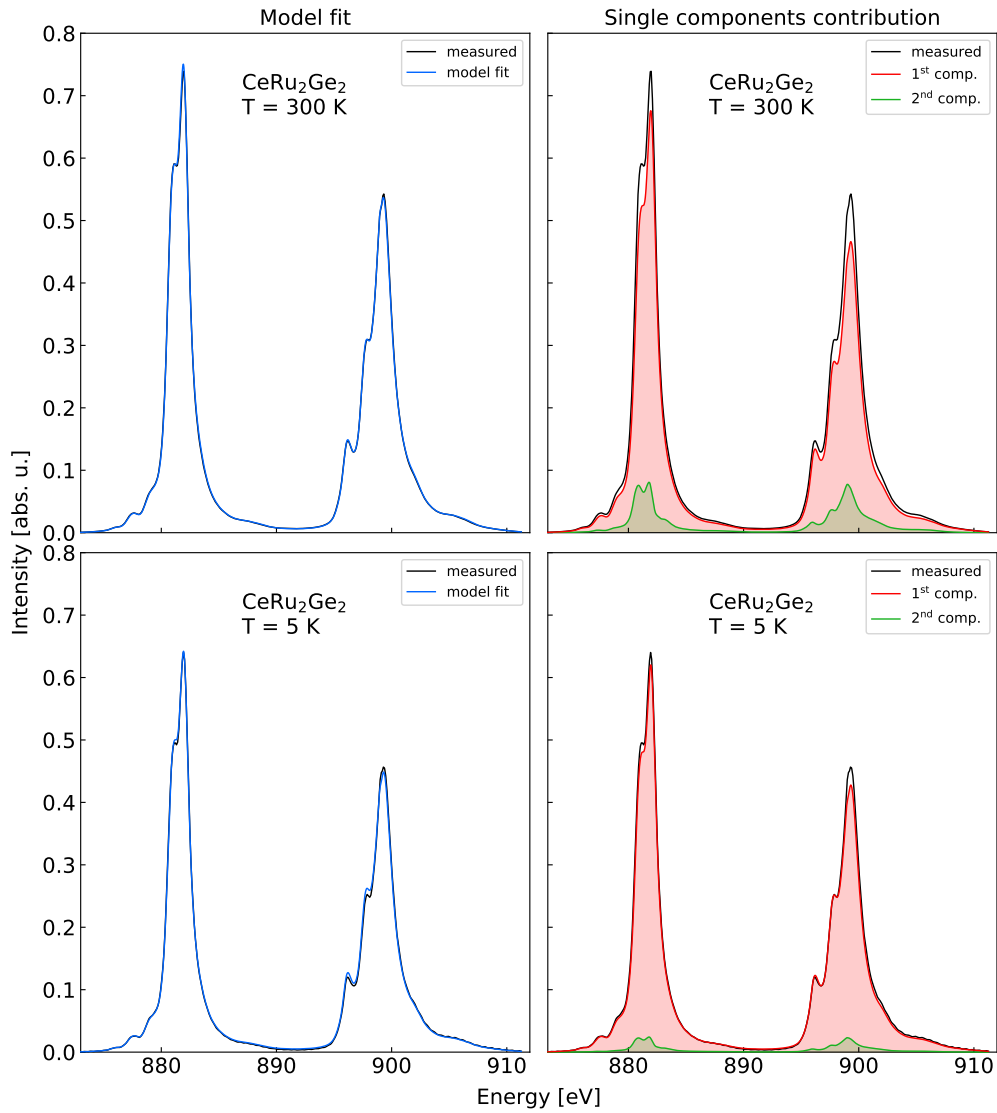


Figure 3.29: Model fit of the MCR-ALS analysis on CeRu_2Ge_2 with two PCs when the mean of spectra and the difference between measurements at 5 and 300 K were used as suitable initial guesses. The R2 factor is 99.9948% and the maximum of the residuals is of the order of 10^{-6} .

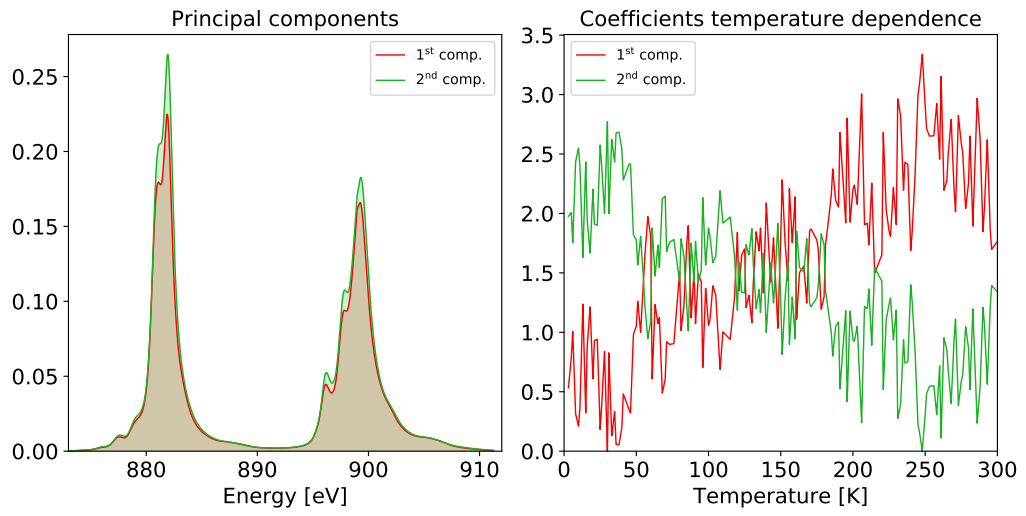


Figure 3.30: PCA on CeRu_2Ge_2 with two PCs when EFA is used as method to generate a suitable initial guess.

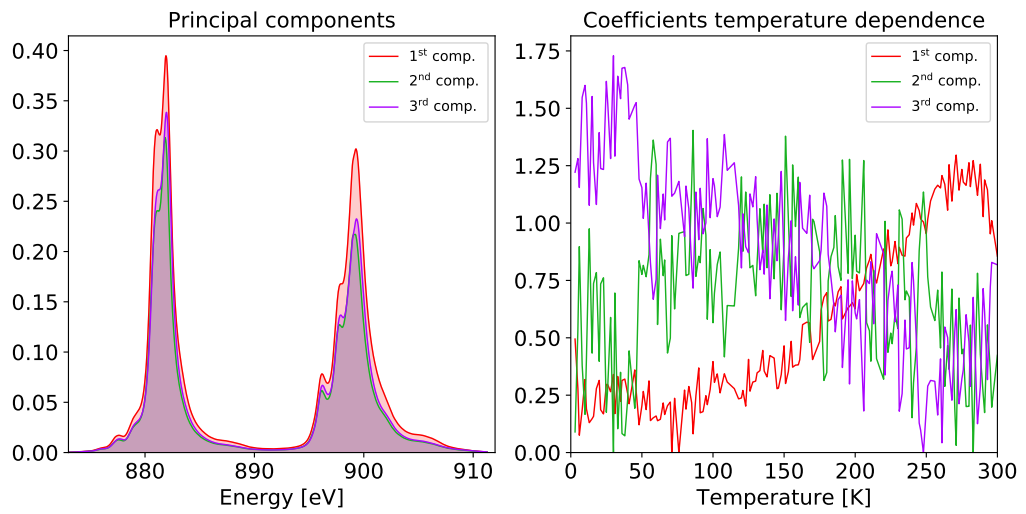


Figure 3.31: PCA on CeRu_2Ge_2 with two PCs when EFA is used as method to generate a suitable initial guess.

3.2 Soft X-ray absorption spectroscopy on Ce 122 systems

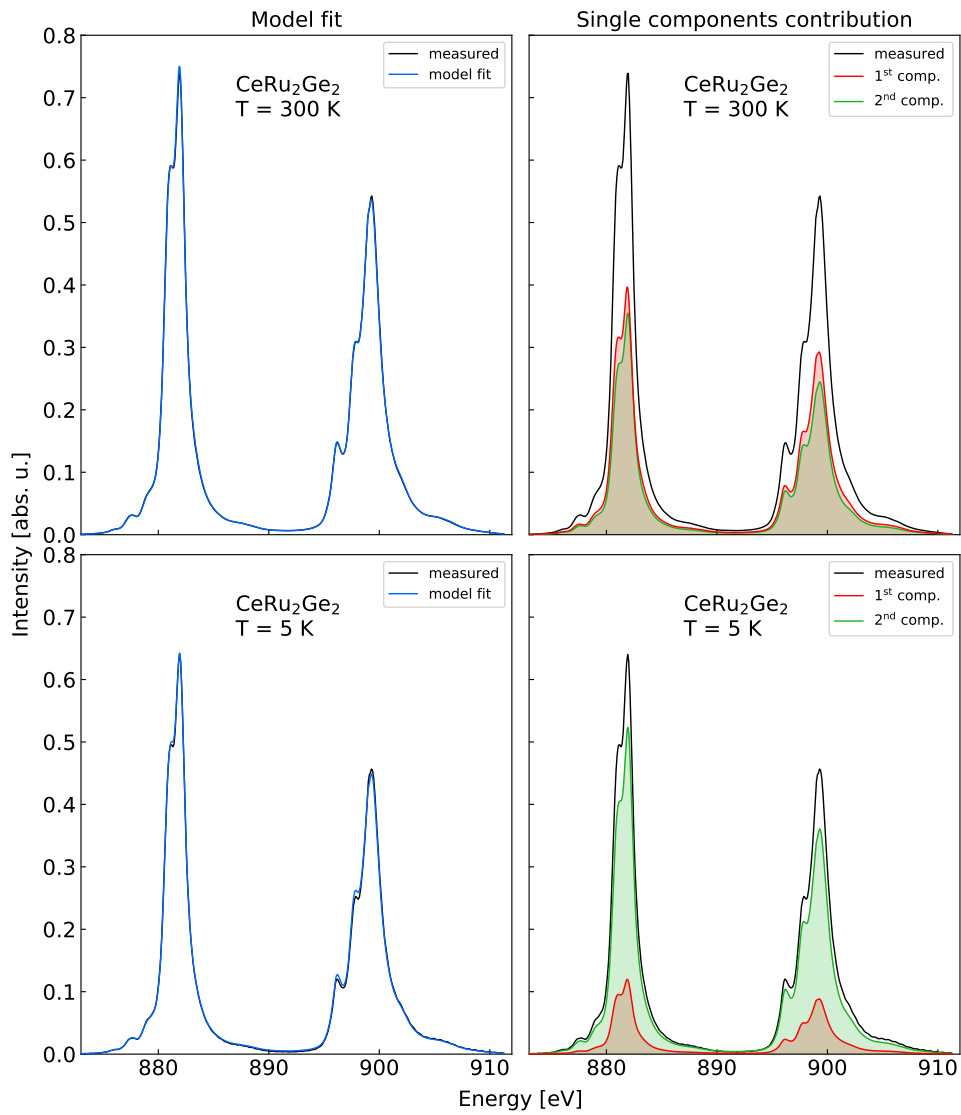


Figure 3.32: Model fit of the MCR-ALS analysis on CeRu_2Ge_2 with two PCs with evolving factor analysis for the initial guess selection. R2 factor is 99.9944% and the maximum of the residuals is of the order of 10^{-4} .

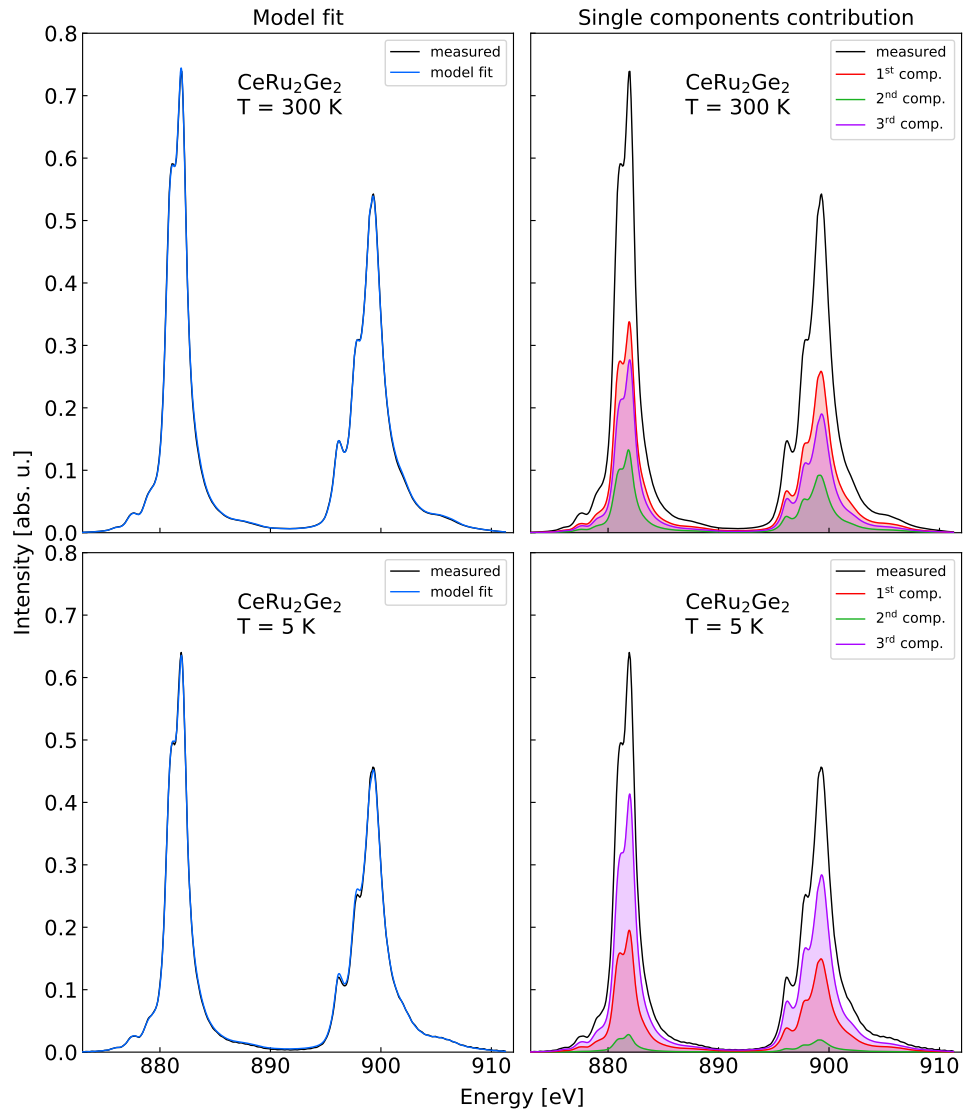


Figure 3.33: Model fit of the MCR-ALS analysis on CeRu_2Ge_2 with three PCs with evolving factor analysis for the initial guess selection. R2 factor is 99.9978% and the maximum of the residuals is of the order of 10^{-5} .

3.2 Soft X-ray absorption spectroscopy on Ce 122 systems

| | 2 PCs Pure | 3 PCs Pure | 2 PCs Mean&Diff | 2 PCs EFA | 3 PCs EFA |
|-----------|------------|------------|-----------------|-----------|-----------|
| R2 | 99.9944% | 99.9978% | 99.9948% | 99.9944% | 99.9978% |
| Residuals | 10^{-5} | 10^{-6} | 10^{-6} | 10^{-5} | 10^{-6} |

Table 3.5: R2 factors and max order of magnitude of residuals of MCR-ALS analysis on CeRu_2Ge_2

By just looking at all the principal component analysis on CeRu_2Ge_2 , the same conclusion drawn from the CeNi_2Si_2 study arises: each component resembles the general shape of the spectrum and none of them is able to isolate the Ce^{+4} contribution. Again, the MCR-ALS method has failed.

All in all, both CeNi_2Si_2 and CeRu_2Ge_2 MCR-ALS analysis were totally inconclusive. Despite having really good model fits and low residuals as reported in tables 3.4, 3.5, all the PCs calculated from different initial guesses resemble the shape of the entire XAS spectrum: the Ce^{+4} contributions have not been isolated into a single principal component.

The reasons why this method did not work could be several. However, comparing the mere shape of YbRh_2Si_2 measurements with the ones of CeNi_2Si_2 and CeRu_2Ge_2 , some hypotheses could be drawn.

First of all, the general shape of YbRh_2Si_2 spectra is much simpler than the one of Ce compounds: in the former there are only two peaks, while in the latter there are two groups of four/five peaks each.

Secondly, the temperature evolution of the intensity of different peaks. In the YbRh_2Si_2 , the intensities of the Yb^{+2} and Yb^{+3} peaks exhibit an opposite variation and there is a clear dominance of one peak over the other at the extreme of the temperature range. Instead, in both Ce compounds, the $4f^0$ peak never becomes dominant: its max intensity is almost on order of magnitude lower than the highest peak intensity. Moreover, other peaks not related to the $4f^0$ contribution show a similar temperature dependence of the $4f^0$ peak, making it almost impossible to separate their contributions. In the end, the MCR-ALS analysis could lead to good results only for specific types of measurements. Probably, by applying more constraints regarding the features of the principal component, good results can be obtained. However, in doing so, implicit a priori information about the phenomenon is being provided, making the MCR-ALS lose its power of generating good analysis without any a priori knowledge. Since the purpose of this thesis was only to test the PCA as a method for spectra analysis, no further investigations were carried on regarding changes in the algorithm that might provide better results.

Having found poor results with the MCR-ALS on two Ce compounds,

the analysis regarding the temperature dependence of intermediate valence in those compounds is carried on with a more classical analysis.

The SNIP algorithm, despite not being the most correct approach to peak extraction, works well and does not implies much data manipulation. The algorithm extracts the background of the peak in an iterative way. Let $v(p)$ be the spectra intensity over energy. At each iteration the algorithm calculates

$$v_{M+1}(i) = \min \left\{ v_M(i), \frac{v_M(i-M) + v_M(i+M)}{2} \right\} \quad (3.2)$$

The result is the peak background. In figure 3.34 an example of the SNIP algorithm working is reported.

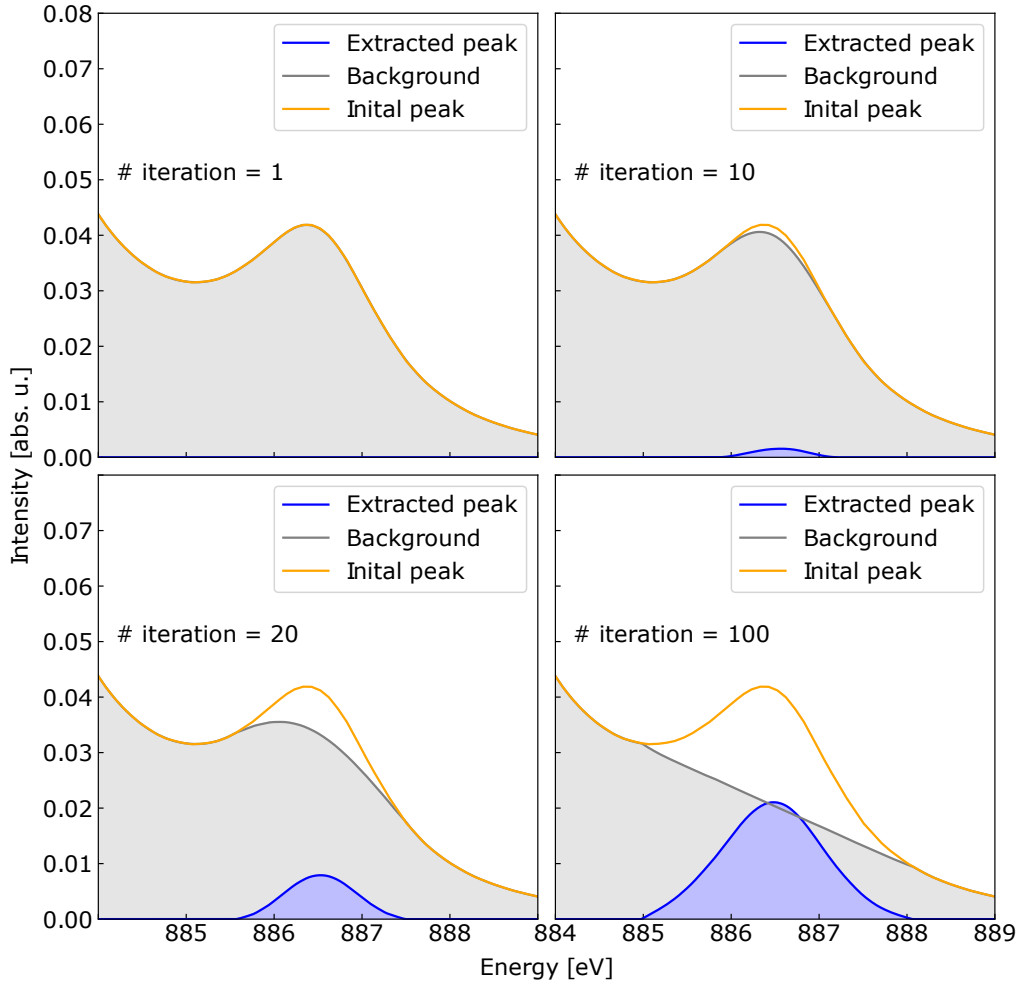


Figure 3.34: Example of SNIP algorithm applied to CeNi_2Si_2 with at different number of iterations.

Once two of the four $4f^0$ peaks are extracted from the M_4 and M_5 edges, the evolution of the peak maximum over the temperature is plotted and fitted with a 5^{th} degree polynomial function. In figure 3.35 the temperature evolution of the M_4 edge $4f^0$ peak is reported (zoomed version shown in figure 3.36). The same results regarding the M_5 edge are reported in the same order as the M_4 edge in figures 3.37 and 3.38.

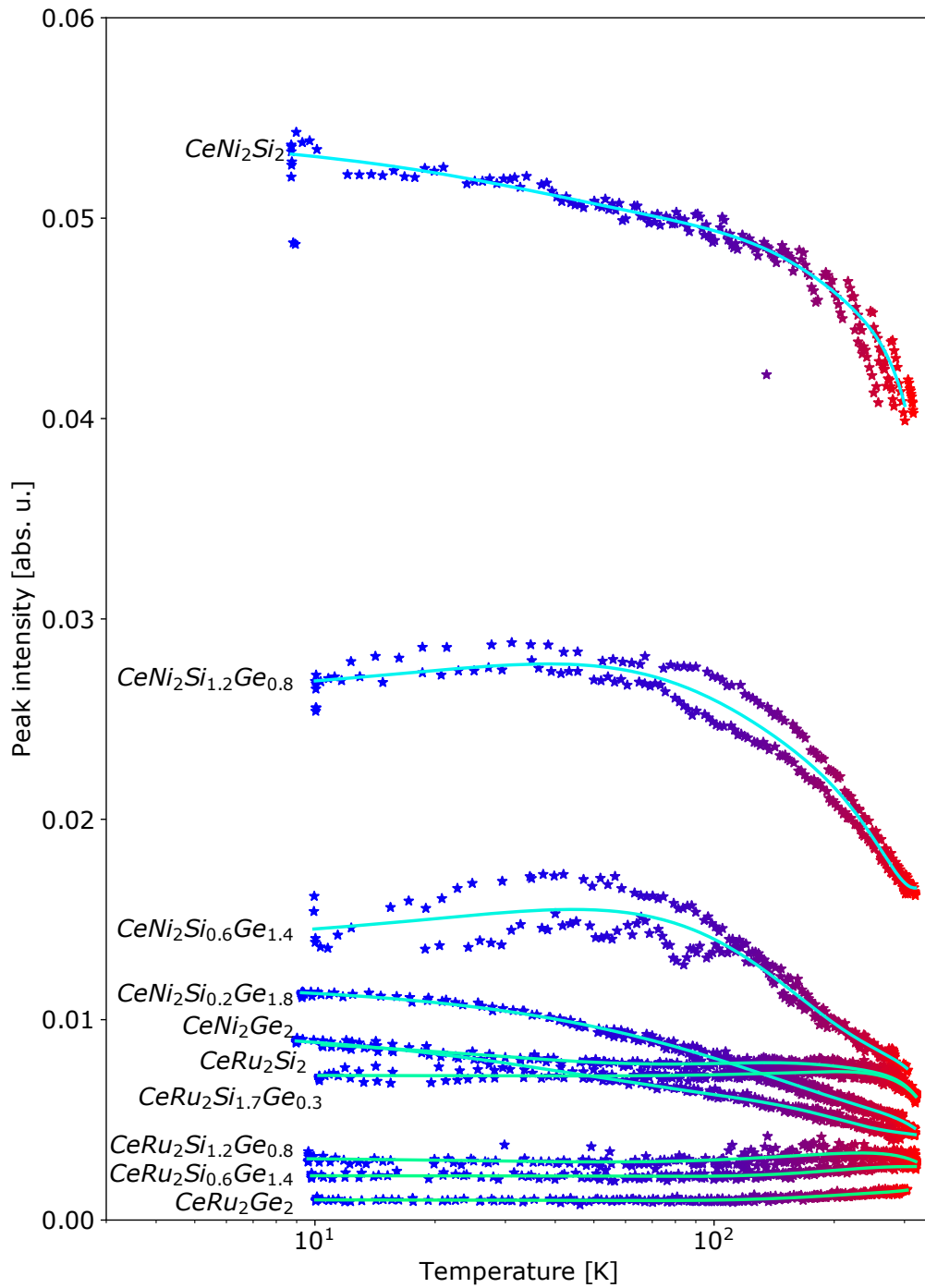


Figure 3.35: M_4 edge $4f^0$ peaks temperature evolution from several ternary Ce compounds.

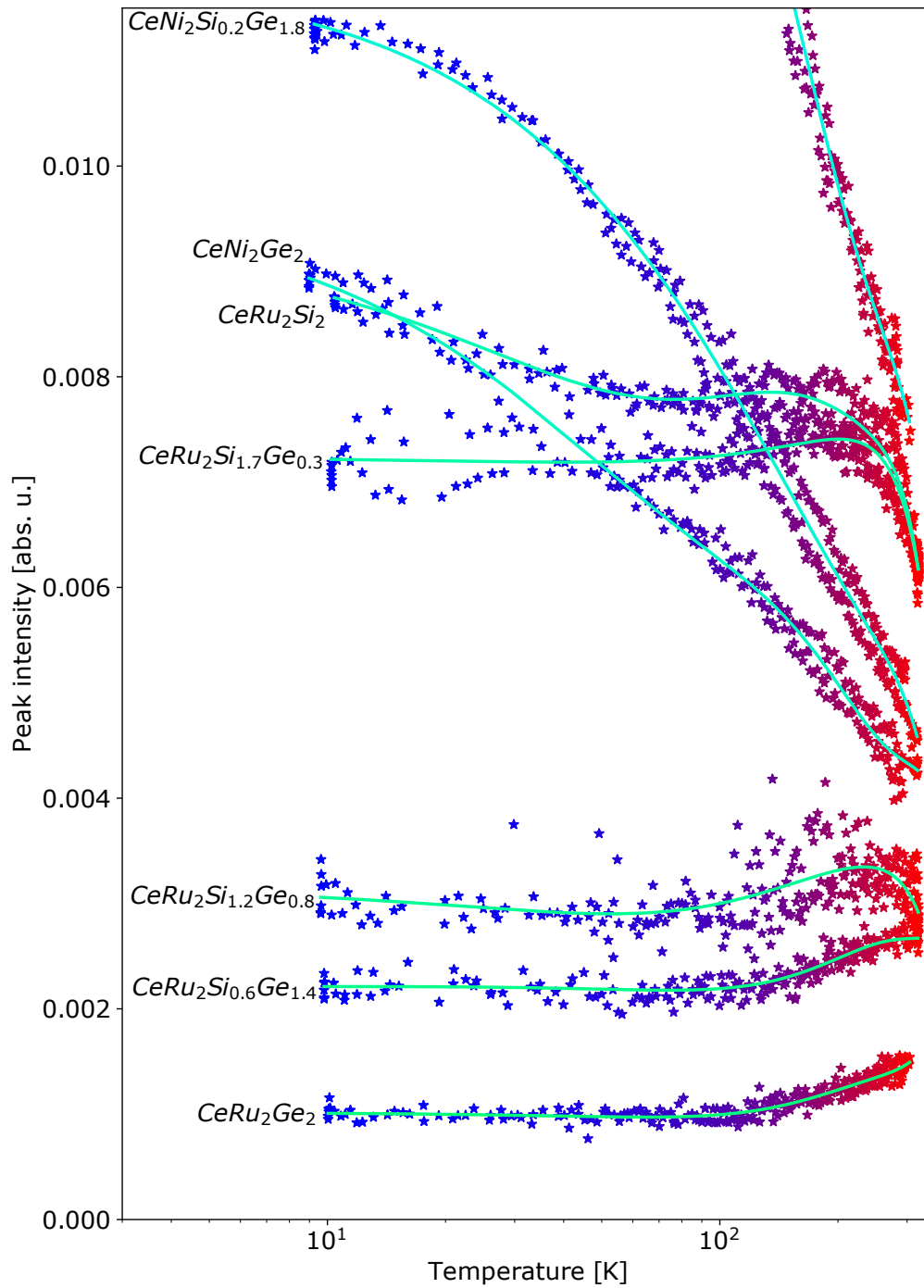


Figure 3.36: Zoomed version of figure 3.35. Despite being small, $CeRu_2Si_{0.6}Ge_{1.4}$ and $CeRu_2Ge_2$ exhibits and increasing contribution of the $4f^0$ as the temperature arises.

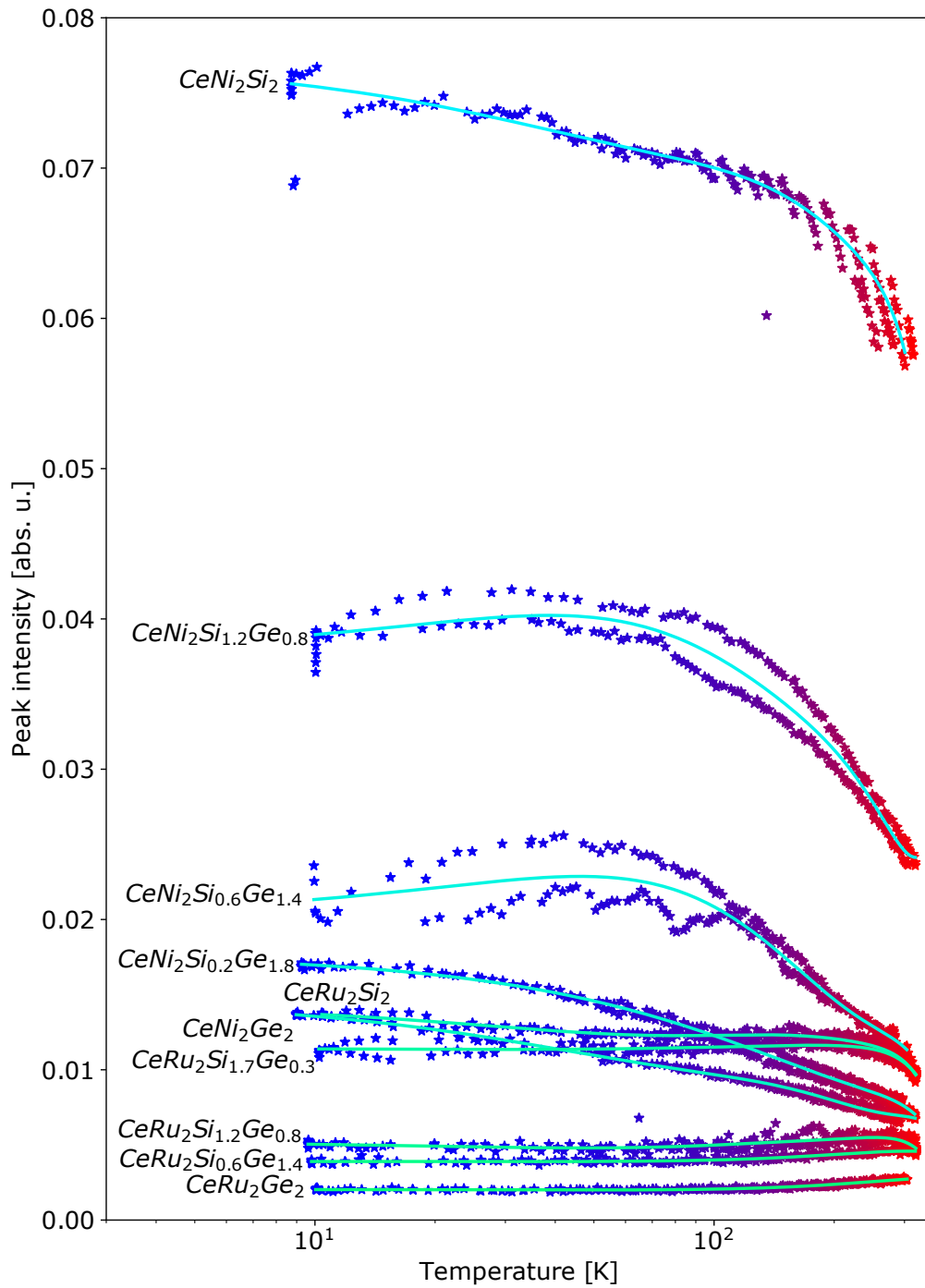


Figure 3.37: M_5 edge $4f^0$ peaks temperature evolution from several ternary Ce compounds.

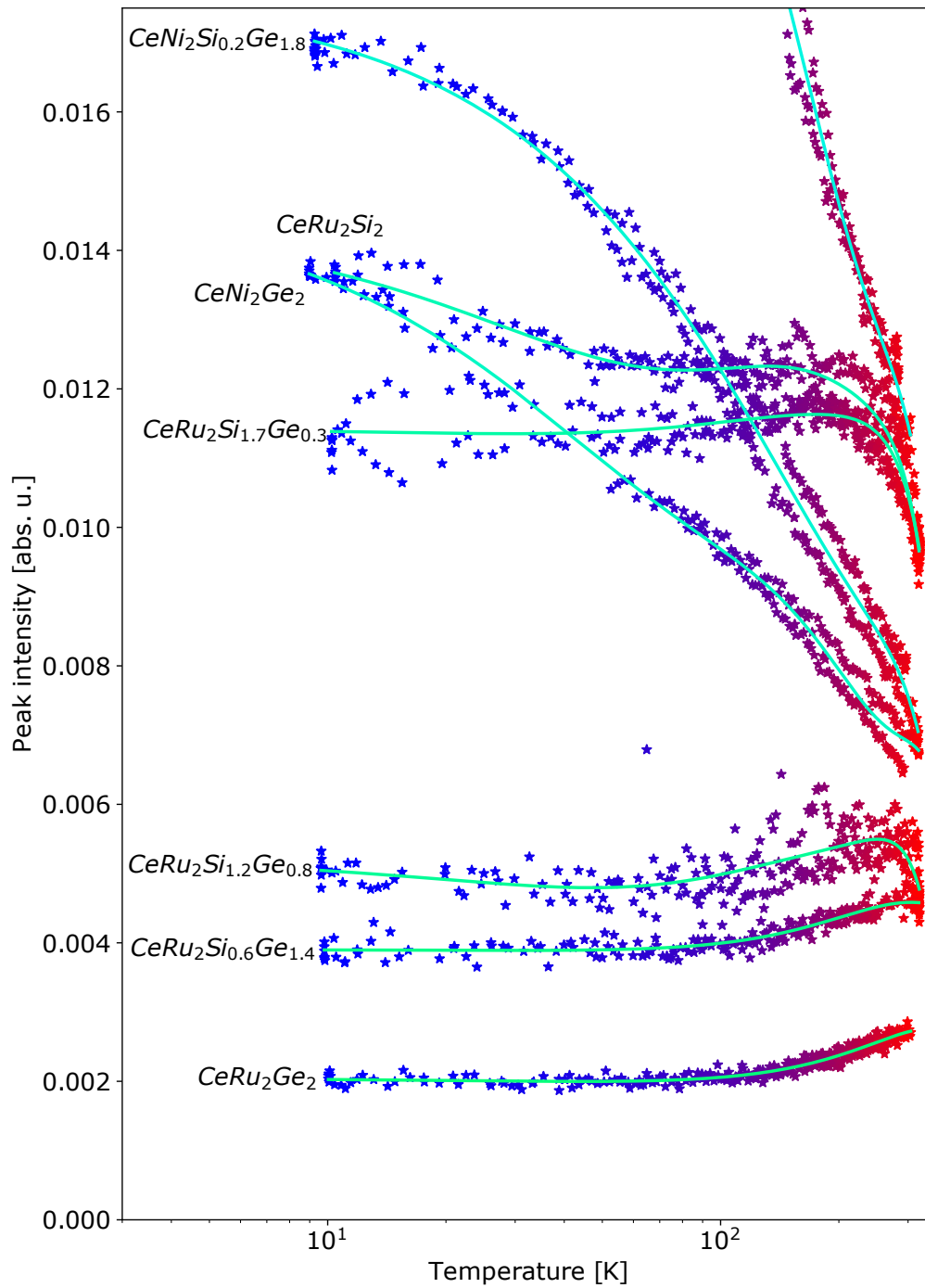


Figure 3.38: Zoomed version of figure 3.37. Despite being small, $CeRu_2Si_{0.6}Ge_{1.4}$ and $CeRu_2Ge_2$ exhibits and increasing contribution of the $4f^0$ as the temperature arises.

Looking at figures 3.35 and 3.37, a pattern clearly emerges. There is a coherent transition from CeNi_2Si_2 to CeRu_2Ge_2 . The overall intensity is decreasing and the temperature behavior is changing: as the temperature rises, in CeNi_2Si_2 the peak intensity decreases; while in CeRu_2Ge_2 the peak intensity increases, despite the overall intensity being small. There is no general theory predicting this kind of behavior. Possible factors include the crystal electric field effect and the variation of the lattice constants of the crystal structure. Indeed, notice how the compound with the smallest lattice constant, CeNi_2Si_2 , exhibits the highest intensity of the $4f^0$, while the largest compound, CeRu_2Ge_2 , practically shows no hybridization (see table 3.3 for lattice constants). Moreover, the transition seems to be continuous. This behavior suggests that the variation of lattice constants actually affects the hybridization strength.

In order to better see the general dependence of the $4f^0$ contributions over temperature, all the previous plots are normalized such that the minimum is at 0 abs. u. and the maximum at 0.06. The resulting plots are reported in figures 3.39 and 3.40.

Many factors are worth to be noticed. Firstly, the general behavior change from being decreasing to increasing somehow in a continuous way, suggesting the existence of a competition between two different contributions. Secondly, all these compounds exhibit the same Kondo temperature and energy scale; and lastly some compounds exhibit some sort of hysteresis loop when the temperature is lowered and risen again. The increasing intensity of the $4f^0$ peak, as the temperature rises, has no explanation in the model presented in chapter 1. As said before, one possible explanation could be the effect of the crystal electric field. Indeed, the first excited level assuming the CEF splitting would be around 200-300K. Populating this excited level creates an increase of the degeneracy, leading to higher Kondo temperature and ultimately to higher occupation of the $4f^0$ shell. Since strong hybridization destroys the idea of having crystal field splitting, this kind of effect will be only visible when the hybridization is weak. That is the case of CeRu_2Ge_2 : it shows practically no hybridization at low temperature, but around 200-300 K there is an increase in the $4f^0$ occupancy.

Finally, the presence of the hysteresis loop can be caused by some misplacements during measurement due to dilatation and shrinkage of the sample holder.

3.2 Soft X-ray absorption spectroscopy on Ce 122 systems

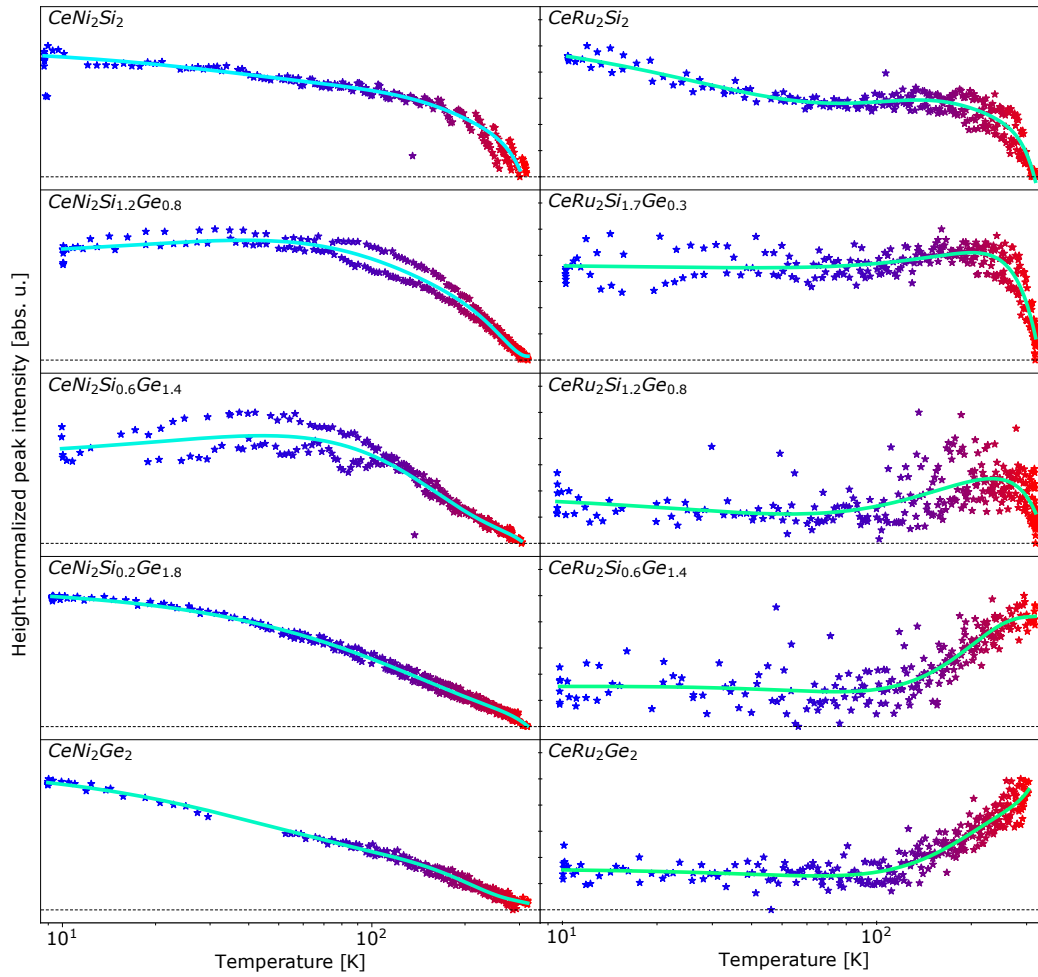


Figure 3.39: Normalized M_4 edge $4f^0$ peaks temperature evolution from several ternary Ce compounds.

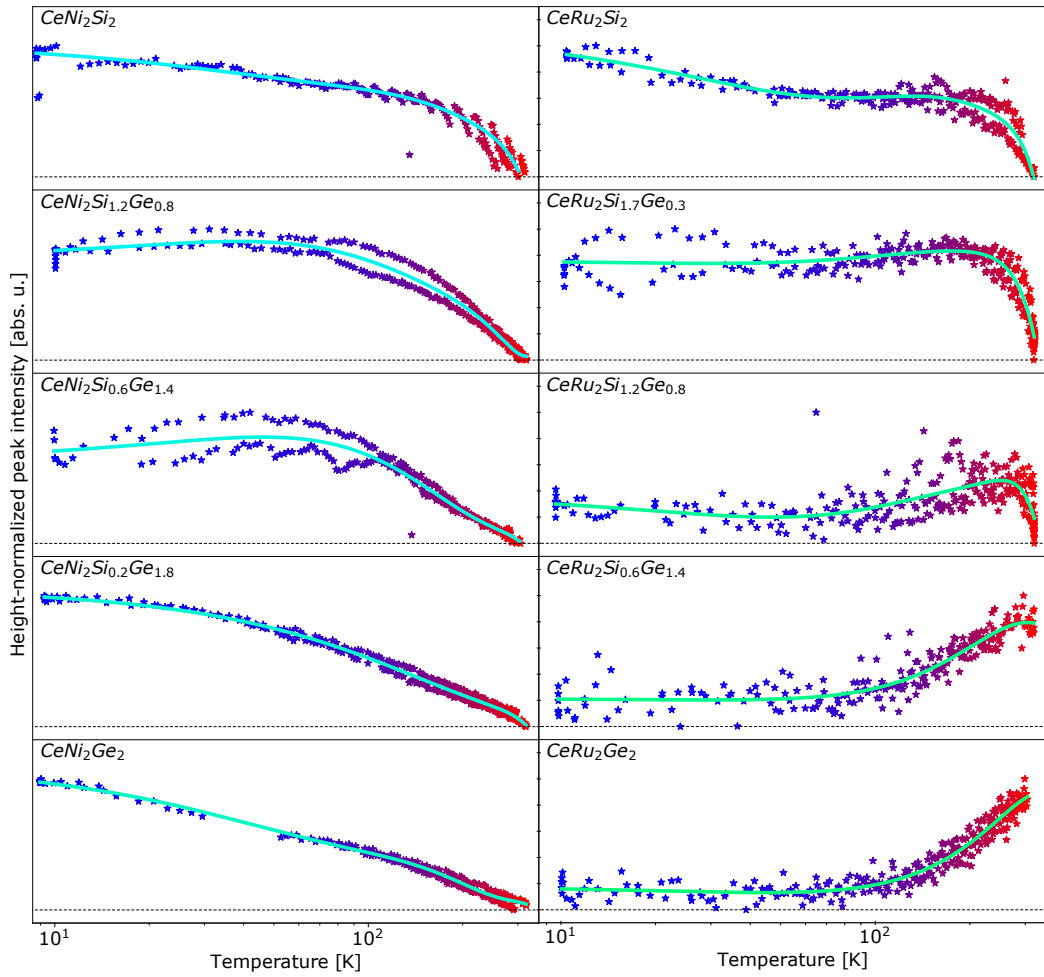


Figure 3.40: Normalized M_5 edge $4f^0$ peaks temperature evolution from several ternary Ce compounds.

Chapter 4

Simulation on XAS and RIXS spectra of strongly correlated oxides from first principles

In this study, the $L_{2,3}$ edges XAS and L_3 edge RIXS spectra are taken into account. The L_2 and L_3 edges respectively describe excitations from the $2p_{1/2}$ and $2p_{3/2}$ shells to the 3d shell. The different features of the L_3 RIXS spectra are characteristic excitations of the system in the final state. The final states corresponding to a re-arrangement of the 3d electrons at constant 3d population are usually indicated as dd excitations. In the following chapter, the simulated spectra of NiO and MnO resulting from DFT calculation are reported. In order to achieve that, the combination of two software, FPLO[®] [46] and Quanty [47, 8], has been exploited.

FPLO[®], developed at IFW Dresden (Institute for Theoretical Solid-State Physics, Group Numerical Solid-State Physics and Simulation), allows the user to calculate the electronic band structure of solids and use WFs to build localized orbitals.

On the other hand, Quanty, developed by M. W. Haverkort, Y. Lu S. Macke, R. Green, M. Brass and S. Heinze, works with a small cluster of atoms and can be used to simulate spectra by defining the Hamiltonian and transitions operator in the second quantization framework. To simulate the XAS and RIXS spectra, the atomic multiplet framework introduced in chapter 1 has been used. In order to simulate different types of spectroscopic measurements, Quanty needs the following parameters regarding the compounds in study:

- Coulomb repulsion between two electron in the d shell, U_{dd}

- Coulomb repulsion between one electron in the p shell and another in the d shell, U_{pd}
- Slater integrals, F^k and G^k
- Crystal Electric Field parameters, A_k^m
- Spin-orbit interaction, ζ_{2p} and ζ_{3d}
- Charge transfer energy, Δ

As aforementioned in chapter 1, WF act as a bridge connecting the infinite crystal framework, in which FPLO[®] operates, with the localized cluster used in Quanty. Indeed, both for MnO and NiO, the Slater integrals F^k , G^k , and the CEF parameters A_k^m are obtained from DFT calculations. The remaining parameters necessary for the simulation are taken from literature.

Since the 3d and 2p shells of the transition metal and oxygen, respectively, are the only orbitals needed to simulated the $L_{2,3}$ XAS and RIXS, no other shells are considered in order to reduce the total computational time.

4.1 NiO

In figure 4.1 the unit cell of NiO and the cluster used in Quanty are reported.

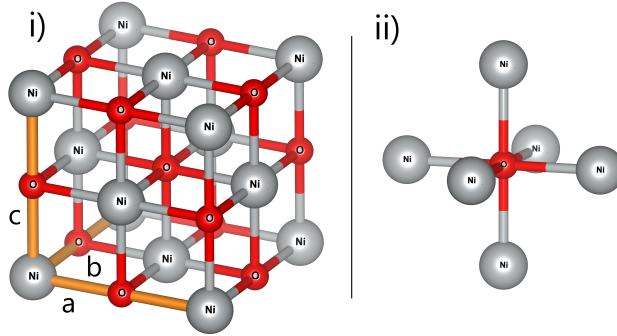


Figure 4.1: i) Unit cell of NiO. $a = b = c = 4.178 \text{ \AA}$ (data taken from [48]). ii) Cluster of atoms extracted from NiO crystalline structure used in Quanty.

In the simulation the following parameters have been used: $U_{dd}=7.3 \text{ eV}$, $U_{pd}=8.5 \text{ eV}$, $\Delta = 4.7 \text{ eV}$, $\zeta_{2p}=11.51 \text{ eV}$, $\zeta_{3d}=0.08 \text{ eV}$ [8]

4.1.1 Band structure

In figure 4.2, the electronic band structure of NiO is plotted.

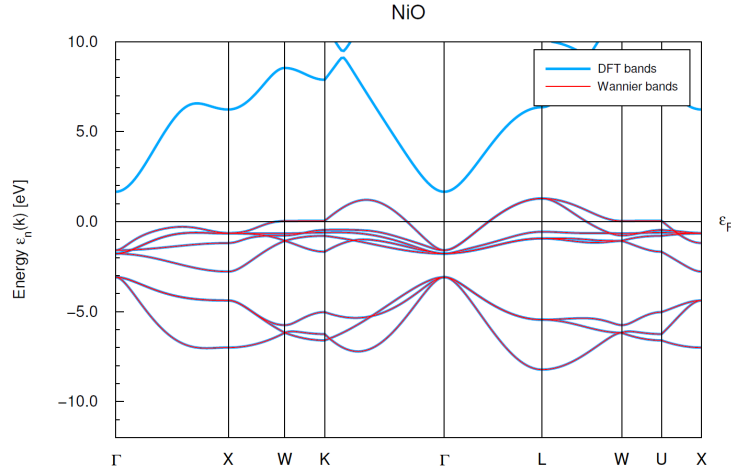


Figure 4.2: Band structure of NiO in the $[-10, 10]$ eV energy range. The band reconstructed from the WFs (red) are perfectly fitting the bands calculated from DFT (blue). Since the WFs are defined only for the 2p and 3d shells, they do not extend over the whole energy windows selected.

In the WFs definition, only the 3d shell of Ni and 2p shell of O have been taken into account, since those are the only orbitals needed to simulate the spectra as aforementioned. Therefore the band structure reconstructed from the WFs, is not complete in the $[-10, 10]$ eV energy range. Notably, the match between the two bands is practically perfect, confirming a good definition of the WFs.

4.1.2 XAS spectra

In figure 4.3, the X-ray absorption spectroscopy measurements [49] and simulation at the $L_{2,3}$ edges of NiO are reported. Each spectra is normalized to its maximum intensity.

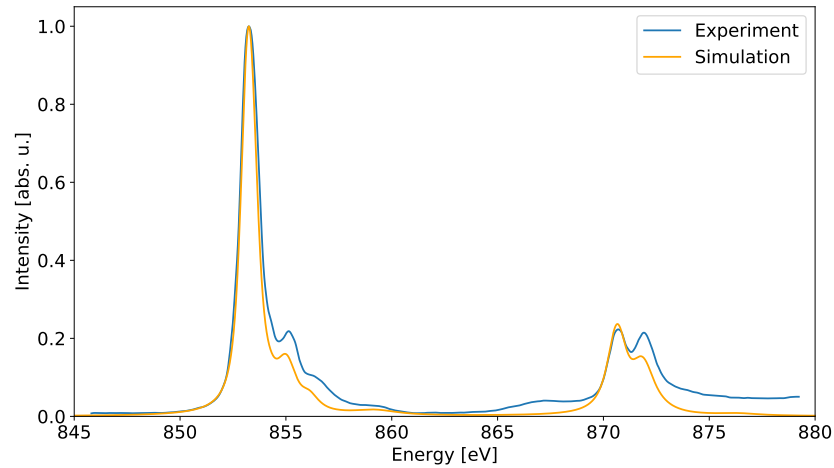


Figure 4.3: X-ray Absorption Spectroscopy measurements and simulation on NiO at $L_{2,3}$ edges. Experimental data taken from [49]. The intensity are normalized to the maximum. Notably, the match is not perfect, but the simulation is able to reconstruct the different features of the spectra. Background is not simulated.

Looking at the plot, the simulation succeeded in reproducing all the peaks at the correct energy, despite some of them having a lower intensity with respect to the experiment. Therefore, DFT calculation seems to be correct. No background has been simulated since the purpose of the simulation is to correctly reconstruct the different features of spectra.

4.1.3 RIXS spectra

In figure 4.4, experimental [50] and simulated RIXS spectra of NiO with incident photon energy at 853 eV are reported. A Lorentzian broadening of 0.2 eV has been applied to the simulated spectra.

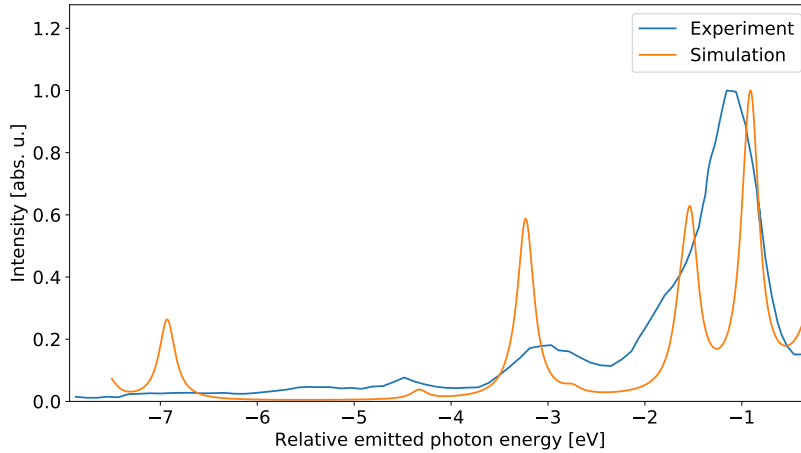


Figure 4.4: Experimental (blue) and simulated (orange) RIXS of MnO with incident photon energy at 853 eV. Experimental data extracted from [50]. A Lorentzian broadening of 0.2 eV has been applied to the simulated spectra.

Looking at experimental RIXS, it is possible to distinguish three different major peaks; however a small shoulder is present on the left side of the highest peak, suggesting the presence of a fourth peak. Notably, four out of five peaks present in the simulated spectra have a match with the experimental one. Starting from right to left, the 1st, 2nd and 4th simulated peaks are slightly at higher energies than the experimental RIXS; whereas the 3rd peak is shifted at lower energies. The 5th has no correspondence with the measurements. In the end, most of the features have been correctly modeled.

4.2 MnO

In figure 4.5 the unit cell of MnO and the cluster used in Quantity are reported.

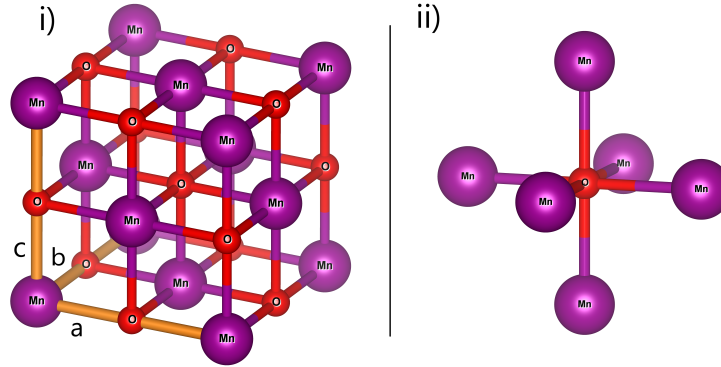


Figure 4.5: i) Unit cell of MnO. $a = b = c = 4.446 \text{ \AA}$ (data taken from [48]). ii) Cluster of atoms extracted from MnO crystalline structure used in Quantity.

In the simulation the following parameters have been used: $U_{dd}=5.5 \text{ eV}$, $U_{pd}=7.2 \text{ eV}$, $\Delta = 8.0 \text{ eV}$, $\zeta_{2p}=6.85 \text{ eV}$, $\zeta_{3d}=0.04 \text{ eV}$ [8]

4.2.1 Band structure

In figure 4.6, the electronic band structure of the MnO is plotted.

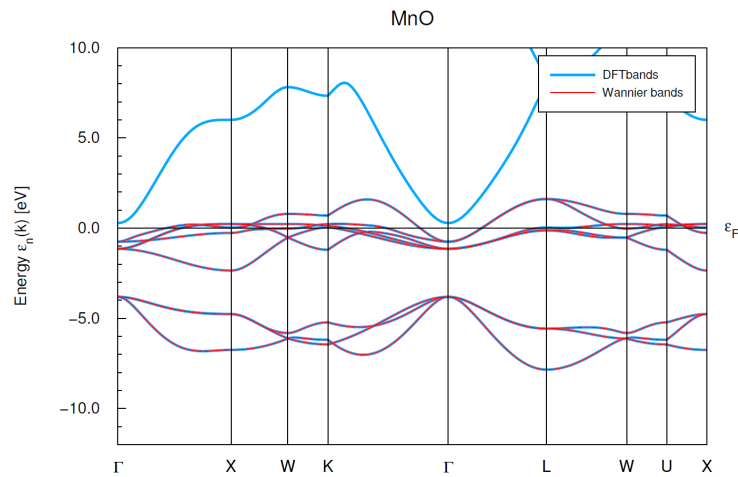


Figure 4.6: Band structure of MnO in the $[-10, 10] \text{ eV}$ energy range. The band reconstructed from the WFs (red) are perfectly fitting the bands calculated from DFT (blue). Since the WFs are defined only for the 2p and 3d shells, they do not extend over the whole energy windows selected.

As for the NiO, only the 3d and 2p shells of Mn and O respectively are used. Looking at the figure, the band structure from DFT calculation and the one resulting from WF display a perfect match. Again, this is a clue that the WF are well-localized and correctly resembling the atomic orbitals around the ions.

4.2.2 XAS spectra

In figure 4.7, the measured and simulated XAS of MnO at $L_{2,3}$ edge are reported.

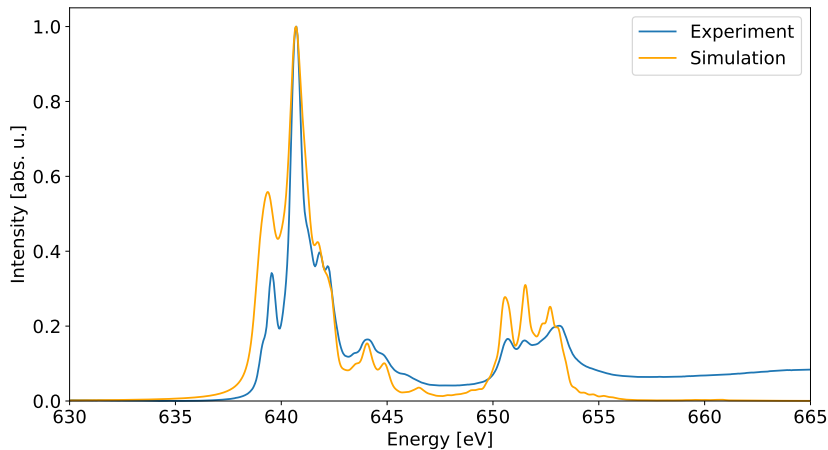


Figure 4.7: X-ray Absorption Spectroscopy measurements and simulation on MnO at $L_{2,3}$ edges. The intensity are normalized to the maximum. Notably, the match is not perfect, but the simulation is able to reconstruct the different feature of the spectra. Background is not simulated.

The spectra are both normalized to its maximum intensity. Notably, the simulated spectra is well describing all the different peaks in terms of energy positioning. As for NiO, no background has been simulated. Again, by just looking at the XAS, DFT calculations seem to be correct.

4.2.3 RIXS spectra

In figure 4.8, the simulated and measured RIXS spectra at 640 eV are reported. A Lorentzian broadening of 0.2 eV has been applied to the simulated spectra.

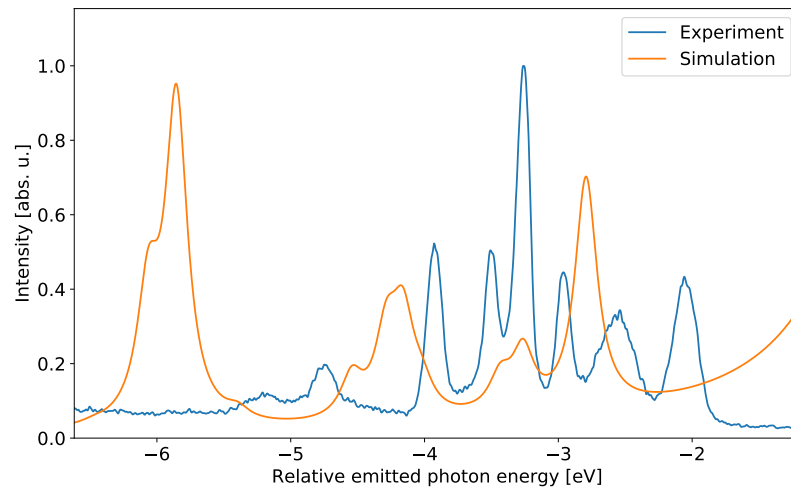


Figure 4.8: Experimental (blue) and simulated (orange) RIXS of MnO with incident photon energy at 640 eV. A Lorentzian broadening of 0.2 eV has been applied to the simulated spectra.

Clearly, the two spectra are completely different: despite having a good fit in the XAS case, the simulation is not able to correctly describe all the features of the RIXS measurement.

In conclusion, the usage of DFT to calculate key parameters used in spectra simulation has led to different results. XAS simulated are good when compared with measurements; however, the RIXS simulations are not as good as the XAS. Since a combination of two software is used in order to calculate parameters and simulated spectra, the problem could dwell in both of them. In order to understand the true nature of the problem, a more deep and consistent analysis must be pursued. However, due to the limited amount of time at disposal and since the aim of the thesis was to test the goodness of this method to simulated spectra, no further investigations have been carried on.

Chapter 5

Summary and outlooks

In this thesis work, modern tools for data analysis and simulation for X-ray spectroscopic data have been presented and tested. In chapter 1, theoretical fundamentals of multivariate curve resolution in conjunction with alternating least squared algorithm (MCR-ALS), density functional theory (DFT) and heavy fermion physics are provided to the reader. A brief description of the X-Ray Absorption Spectroscopy (XAS) and Resonant Inelastic X-ray Scattering (RIXS), from both theoretical and experimental points of view, are presented in chapter 2. Chapters 3 and 4 contain the results of the data analysis and simulation, respectively. Specifically, in chapter 3 a principal component analysis performed on YbRh_2Si_2 , CeNi_2Si_2 and CeRu_2Ge_2 to investigate the intermediate valence is reported; whereas chapter 4 reports XAS and RIXS spectra simulations of NiO and MnO.

The effectiveness of the MCR-ALS algorithm, used to isolate different features inside spectra, strongly depends on the shape and evolution of measurements and on the initial guess selection. Indeed, simple-shaped spectra with a clear evolution of peak intensities have led to astonishingly good results, both in terms of peak reconstruction and weight evolution. This is the case of YbRh_2Si_2 . However, this method failed to isolated relevant features in complex spectra with smaller intensity evolution. Indeed, for CeNi_2Si_2 and CeRu_2Ge_2 , none of the proposed methods were able to identify and separate the features of the spectra. All the components are resembling the whole shape of the spectra, with almost no difference between each other, despite being the total fit with the experiment perfect. One possible way to solve this problem could be to apply more constraints about the shape of the components. However, in doing so, the ability of these types of algorithms to extract data without any a priori knowledge is greatly affected. In the end, the MCR-ALS algorithm could lead to good results whenever the shape of the spectra is not too complicated, but the resulting analysis in the case

of complex spectra could be inconclusive. For the sake of completeness, the intermediate valence in ternary Ce compounds has been analyzed by manual peak extraction. The results are quite surprising. From theory, the Ce valence should become closer to unity as the temperature rises. However, this is not the case for some of the studied ternary compounds based on Ce, which show an opposite behavior, reflecting the incompleteness of the model and the need for further studies on heavy fermion compounds.

Regarding spectra simulation, the usage of Wannier functions as a bridge to connect DFT calculations in infinite crystals with a cluster-based simulation software works well. Indeed, X-ray Absorption Spectroscopy simulation is quite similar to measurements: despite having some differences in the intensity of the peaks, all the characteristic features of the spectra are correctly positioned in terms of energy. However, Resonant Inelastic X-ray Scattering simulations are not as good as XAS spectra. Looking at NiO, four out of five peaks are almost correct in terms of energy positioning but the simulated spectrum shows an extra peak not present in the measurements. Regarding MnO, there is no match between the simulated and the experimental spectra, both the number of peaks and their energy positioning are wrong. In the end, the combined approach presented to simulate spectra from first principles works properly for XAS, but not for RIXS. In order to understand the reasons behind such discrepancies between the aforementioned simulations, a much deeper analysis both on the parameters and the software must be pursued.

Bibliography

- [1] Vladimir Ilich Anisimov. Electronic structure of strongly correlated materials. In *AIP Conference Proceedings*, volume 1297, pages 3–134. AIP, 2010.
- [2] Yoichi Yanase, Takanobu Jujo, Takuji Nomura, Hiroaki Ikeda, Takashi Hotta, and Kosaku Yamada. Theory of superconductivity in strongly correlated electron systems. *Physics Reports*, 387(1-4):1–149, 2003.
- [3] Alexander I Poteryaev, Michel Ferrero, Antoine Georges, and Olivier Parcollet. Effect of crystal-field splitting and interband hybridization on the metal-insulator transitions of strongly correlated systems. *Physical Review B*, 78(4):045115, 2008.
- [4] S. Sullo F. Steglich. Heavy-fermions systems. In L. Eyring Karl A. Gschneidner, editor, *Handbook on the Physics and Chemistry of Rare Earths*, volume 14, pages 3749–3746. 2001.
- [5] P.W. Anderson. Localized Magnetic States in Metals. *Physical Review*, 124, 1961.
- [6] Judith Felten, Hardy Hall, Joaquim Jaumot, Romà Tauler, Anna De Juan, and András Gorzsás. Vibrational spectroscopic image analysis of biological material using multivariate curve resolution–alternating least squares (mcr-als). *Nature protocols*, 10(2):217, 2015.
- [7] M. Garrido, F. X. Rius, and M. S. Larrechi. Multivariate curve resolution-alternating least squares (MCR-ALS) applied to spectroscopic data from monitoring chemical reactions processes. *Analytical and Bioanalytical Chemistry*, 390(8):2059–2066, 2008.
- [8] M. W. Haverkort, M. Zwierzycki, and O. K. Andersen. Multiplet ligand-field theory using Wannier orbitals. *Physical Review B - Condensed Matter and Materials Physics*, 85(16):1–20, 2012.

Bibliography

- [9] H. Eschrig. *The Fundamentals of Density Functional Theory*. Vieweg+Teubner Verlag, 1996.
- [10] G. H. Shortley E. U. Condon. *The Theory of Atomic Spectra*. Cambridge University Press, 1935.
- [11] A. Kotani F. de Groot. *Core Level Spectroscopy of Solids*. Taylor Francis Group, 2008.
- [12] J. C. Slater. The theory of complex spectra. *Physical Review*, 34(10):1293–1322, 1929.
- [13] B. Jacquier G. Liu. *Spectroscopic Properties of Rare Earths in Optical Materials*. Springer, 2005.
- [14] Frank De Groot. Multiplet effects in X-ray spectroscopy. *Coordination Chemistry Reviews*, 249(1-2):31–63, 2005.
- [15] Betty Ng D. J. Newman. *Crystal Field Handbook*. Cambridge University Press, 2000.
- [16] R.D. Cowan. *The Theory of Atomic Structure and Spectra*. University of California Press, 1981.
- [17] Nicola Marzari and David Vanderbilt. Maximally localized generalized Wannier functions for composite energy bands. *Physical Review B - Condensed Matter and Materials Physics*, 56(20):12847–12865, 1997.
- [18] Nicola Marzari, Arash A. Mostofi, Jonathan R. Yates, Ivo Souza, and David Vanderbilt. Maximally localized Wannier functions: Theory and applications. *Reviews of Modern Physics*, 84(4):1419–1475, 2012.
- [19] T. Park, V. A. Sidorov, F. Ronning, J. X. Zhu, Y. Tokiwa, H. Lee, E. D. Bauer, R. Movshovich, J. L. Sarrao, and J. D. Thompson. Isotropic quantum scattering and unconventional superconductivity. *Nature*, 456(7220):366–368, 2008.
- [20] G R Stewart. Heavy-fermion systems. *Reviews of Modern Physics*, 56(4):755–787, 1984.
- [21] Yoshichika Onuki, Yoshiaki Shimizu, Munekazu Nishihara, Yohichi Machii, and Takemi Komatsubara. Kondo Lattice Formation in $\text{Ce}_x\text{La}_{1-x}\text{Cu}_6$. *Journal of the Physical Society of Japan*, 54(5):1964–1974, 1985.

-
- [22] M. Coldea, M. Neumann, V. Pop, and M. Demeter. Mixed valence state of Ce ions in CeNi_2Al_3 . *Journal of Alloys and Compounds*, 323-324:431–434, 2001.
- [23] J. P. Rueff, S. Raymond, M. Taguchi, M. Sikora, J. P. Itié, F. Baudalet, D. Braithwaite, G. Knebel, and D. Jaccard. Pressure-induced valence crossover in superconducting CeCu_2Si_2 . *Physical Review Letters*, 106(18):2–5, 2011.
- [24] H. Yamaoka, Y. Yamamoto, E. F. Schwier, F. Honda, Y. Zekko, Y. Ohta, J. F. Lin, M. Nakatake, H. Iwasawa, M. Arita, K. Shimada, N. Hiraoaka, H. Ishii, K. D. Tsuei, and J. Mizuki. Pressure and temperature dependence of the Ce valence and c-f hybridization gap in CeTIn_5 (T=Co,Rh,Ir) heavy-fermion superconductors. *Physical Review B - Condensed Matter and Materials Physics*, 92(23):1–6, 2015.
- [25] Tuson Park, F. Ronning, H. Q. Yuan, M. B. Salamon, R. Movshovich, J. L. Sarrao, and J. D. Thompson. Hidden magnetism and quantum criticality in the heavy fermion superconductor CeRhIn_5 . *Nature*, 440(7080) : 65 – –68, 2006.
- [26] P. Coleman. Heavy Fermions: electrons at the edge of magnetism. 1:1–97, 2006.
- [27] N. E. Bickers, D. L. Cox, and J. W. Wilkins. Self-consistent large-N expansion for normal-state properties of dilute magnetic alloys. *Physical Review B*, 36(4):2036–2079, 1987.
- [28] Alexander T. Holmes, Didier Jaccard, and Kazumasa Miyake. Valence instability and superconductivity in heavy fermion systems. *Journal of the Physical Society of Japan*, 76(5):1–10, 2007.
- [29] N Metoki, K Kaneko, T D Matsuda, A Galatanu, T Takeuchi, S Hashimoto, T Ueda, R Settai, Y Nuki, and N Bernhoeft. Magnetic structure and the crystal field excitation in heavy-fermion antiferromagnetic superconductor CePt_3Si . *Journal of Physics: Condensed Matter*, 16(15):L207–L212, 2004.
- [30] S. Raymond, P. Haen, R. Calemczuk, S. Kambe, B. Fåk, P. Lejay, T. Fukuhara, and J. Flouquet. From heavy fermion antiferromagnetism to localized ferromagnetism: Competition of two ground states in CeRu_2Ge_2 on cooling. *Journal of Physics Condensed Matter*, 11(29):5547–5560, 1999.

- [31] M Yano, A Sekiyama, H Fujiwara, Y Amano, S Imada, T Muro, M Yabashi, K Tamasaku, A Higashiya, T Ishikawa, Y. Onuki, and S Suga. Electronic structure of CeRu_2X_2 ($\text{X}=\text{Si,Ge}$) in the paramagnetic phase studied by soft x-ray ARPES and hard x-ray photoelectron spectroscopy. *Physical Review B - Condensed Matter and Materials Physics*, 77(3):1–8, 2008.
- [32] T. Okane, Y. Takeda, H. Yamagami, A. Fujimori, Y. Matsumoto, N. Kimura, T. Komatsubara, and H. Aoki. Magnetic behavior near the boundary of 4f delocalization in ferromagnetic CeRu_2Ge_2 and paramagnetic CeRu_2Si_2 observed by Ce $M_{4,5}$ XAS and XMCD. *Physical Review B - Condensed Matter and Materials Physics*, 86(12):1–11, 2012.
- [33] Z. F. Weng, M. Smidman, L. Jiao, Xin Lu, and H. Q. Yuan. Multiple quantum phase transitions and superconductivity in Ce-based heavy fermions. *Reports on Progress in Physics*, 79(9), 2016.
- [34] Anna De Juan, Joaquim Jaumot, and Romà Tauler. Multivariate Curve Resolution (MCR). Solving the mixture analysis problem. *Analytical Methods*, 6(14):4964–4976, 2014.
- [35] Gene H Golub and Christian Reinsch. Singular value decomposition and least squares solutions. In *Linear Algebra*, pages 134–151. Springer, 1971.
- [36] R. Tauler. Constrained optimization of feasible ranges for species profiles obtained by multivariate curve resolution. https://www.cid.csic.es/homes/rtaqam/tmp/WEB_MCR/download/pdf/feasible.pdf.
- [37] Akio Kotani and Shik Shin. Resonant inelastic x-ray scattering spectra for electrons in solids. *Reviews of Modern Physics*, 73(1):203–246, 2001.
- [38] N. B. Brookes, F. Yakhou-Harris, K. Kummer, A. Fondacaro, J. C. Cezar, D. Betto, E. Velez-Fort, A. Amorese, G. Ghiringhelli, L. Braicovich, R. Barrett, G. Berruyer, F. Cianciosi, L. Eybert, P. Marion, P. van der Linden, and L. Zhang. The beamline ID32 at the ESRF for soft X-ray high energy resolution resonant inelastic X-ray scattering and polarisation dependent X-ray absorption spectroscopy. *Nuclear Instruments and Methods in Physics Research, Section A: Accelerators, Spectrometers, Detectors and Associated Equipment*, 903:175–192, 2018.
- [39] Luuk J.P. Ament, Michel Van Veenendaal, Thomas P. Devereaux, John P. Hill, and Jeroen Van Den Brink. Resonant inelastic x-ray scat-

- tering studies of elementary excitations. *Reviews of Modern Physics*, 83(2):705–767, 2011.
- [40] K. Kummer, C. Geibel, C. Krellner, G. Zwicknagl, C. Laubschat, N. B. Brookes, and D. V. Vyalikh. Similar temperature scale for valence changes in Kondo lattices with different Kondo temperatures. *Nature Communications*, 9(1):1–10, 2018.
- [41] A. V. Morozkin, A. V. Knotko, A. V. Garshev, V. O. Yapaskurt, R. Nir-mala, S. Quezado, and S. K. Malik. The Ce-Ni-Si system as a representative of the rare earth-Ni-Si family: Isothermal section and new rare-earth nickel silicides. *Journal of Solid State Chemistry*, 243:290–303, 2016.
- [42] Wolfhart Rieger and Erwin Parthé. Ternäre Erdalkali-und Seltene Erdmetall-Silicide und-Germanide mit ThCr_2Si_2 -Struktur. *Monatshefte für Chemie*, 100(2):444–454, 1969.
- [43] P. Lejay, J. Muller, and R. Argoud. Crystal growth and stoichiometry study of the ternary silicides CeRu_2Si_2 and $\text{Ce}_{1-x}\text{La}_x\text{Ru}_2\text{Si}_2$. *Journal of Crystal Growth*, 130(1-2):238–244, 1993.
- [44] R. Rawat and V. G. Sathe. Structural and transport studies of $\text{CeRu}_{2-x}\text{Co}_x\text{Ge}_2$. *Journal of Physics Condensed Matter*, 17(2):313–322, 2005.
- [45] T. Willers, D. T. Adroja, B. D. Rainford, Z. Hu, N. Hollmann, P. O. Körner, Y. Y. Chin, D. Schmitz, H. H. Hsieh, H. J. Lin, C. T. Chen, E. D. Bauer, J. L. Sarrao, K. J. McClellan, D. Byler, C. Geibel, F. Steglich, H. Aoki, P. Lejay, A. Tanaka, L. H. Tjeng, and A. Severing. Spectroscopic determination of crystal-field levels in CeRh_2Si_2 and CeRu_2Si_2 and of the $4f^0$ contributions in CeM_2Si_2 ($M=\text{Cu, Ru, Rh, Pd, and Au}$). *Physical Review B - Condensed Matter and Materials Physics*, 85(3):0–8, 2012.
- [46] K. Koepernik. FPLO[®] package. <https://www.fplo.de/>.
- [47] M. W. Haverkort. Quany - a quantum many body script language. <http://www.quany.org/>.
- [48] S Sasaki, K Fujino, and Y Takeuchi. X-Ray Determination of Electron-Density Distributions in Oxides, MgO, MnO, CoO, and NiO, and Atomic Scattering Factors of their Constituent Atoms. *Proceedings of the Japan Academy, Series B*, 55(2):43–48, 1979.

Bibliography

- [49] D. Alders, L. Tjeng, F. Voogt, and T. Hibma. Temperature and thickness dependence of magnetic moments in NiO epitaxial films. *Physical Review B - Condensed Matter and Materials Physics*, 57(18):11623–11631, 1998.
- [50] G. Ghiringhelli, M. Matsubara, C. Dallera, F. Fracassi, R. Gusmeroli, A. Piazzalunga, A. Tagliaferri, N. B. Brookes, A. Kotani, and L. Braicovich. NiO as a test case for high resolution resonant inelastic soft x-ray scattering. *Journal of Physics Condensed Matter*, 17(35):5397–5412, 2005.